Effective Interactions for
Nuclear Structure Calculations

By

Angelo Signoracci

A DISSERTATION

Submitted to
Michigan State University
in partial fulfillment of the requirements
for the degree of

DOCTOR OF PHILOSOPHY

Physics

2011

ABSTRACT

EFFECTIVE INTERACTIONS FOR NUCLEAR STRUCTURE CALCULATIONS

By

Angelo Signoracci

Experimental interest in nuclei far from stability, especially due to proposed advancements in rare isotope facilities, has stimulated improvements in theoretical predictions of exotic isotopes. However, standard techniques developed for nuclear structure calculations, Configuration Interaction theory and Energy Density Functional methods, lack either the generality or the accuracy necessary for reliable calculations away from stability. Hybrid methods, which combine Configuration Interaction theory and Energy Density Functional methods in order to exploit their beneficial properties, are currently under investigation for improved theoretical capabilities.

A new technique to produce nuclear Hamiltonians has been developed, implementing renormalization group methods, many-body perturbative techniques, and Energy Density Functional methods. Connection to the underlying physics is a primary focus, limiting the number of free parameters necessary in the procedure. The main benefit of this approach is the improvement in the quality of effective interactions outside of standard model spaces.

In the Hybrid Renormalization Procedure developed in this dissertation, Skyrme energy density functionals provide a realistic single particle basis that accounts for the long tail of loosely bound orbits, especially significant for valence orbits of exotic isotopes. A microscopic nucleon-nucleon potential is softened with renormalization group techniques to eliminate the hard core of the nuclear interaction. Many-body perturbative techniques, in the form of Rayleigh-Schrödinger theory, implement the realistic basis to convert the low-momentum interaction into a model space of interest.

The basis is an important ingredient in the renormalization and greatly affects the results obtained with the Hybrid Renormalization Procedure, specifically through the single particle energies derived from Skyrme functionals. A comparison of the standard harmonic oscillator basis and the realistic basis derived from energy density functional methods illustrates the necessity of a realistic basis when a microscopic nucleon-nucleon potential is renormalized into the nuclear medium. Because Skyrme single particle energies are unreliable, other sources are desired for the determination of this component of the effective interaction.

An *sd* shell interaction is produced for a proof of principle, and extensive results are obtained in the island of inversion region and for ^{42}Si. One hundred nuclei are calculated near the island of inversion region of the nuclear chart. Binding energies and low-lying excitations agree well with available experimental data. The neutron dripline is determined theoretically for isotopic chains near the island of inversion. The boundaries of the island of inversion region are mapped out, suggesting an extension to lighter and more neutron-rich isotopes than measured experimentally thus far. Reactions in the island of inversion region have also been studied and reproduce experimental behavior, such that conclusions can be reached regarding the evolution of shell structure and the properties of states of particular interest. The known states of ^{42}Si are reproduced with effective interactions derived from the Hybrid Renormalization Procedure, but the detection of the 0_2^+ and 4_1^+ states are important to distinguish between different theoretical approaches.

The viability of the Hybrid Renormalization Procedure is evident from the results in the island of inversion region. Applications to other exotic regions of the nuclear chart are desired for future research.

ACKNOWLEDGMENTS

This document represents the culmination of five years of research and development in nuclear structure physics at the National Superconducting Cyclotron Laboratory and the Department of Physics and Astronomy at Michigan State University. In that time, I have been fortunate to receive instruction and guidance from a committee of scientific researchers, comprised of Alex Brown, Carlo Piermarocchi, Jon Pumplin, Michael Thoennessen, and Vladimir Zelevinsky. In particular, I would like to thank Alex Brown as the advisor of my doctoral research for helpful discussions from the formulation of the project to its completion.

As this project incorporated many aspects of nuclear physics, I am indebted to experts in the subdisciplines relevant for my research: Alex Brown, for CI theory, EDF methods, and general nuclear structure; Morten Hjorth-Jensen, for renormalization group methods and many-body perturbative techniques, and especially for instruction on implementing his programs to produce effective interactions, which were essential for this work; Thomas Duguet, for EDF methods and single particle energies; Scott Bogner, for renormalization group methods; the UNEDF collaboration, for EDF methods and hybrid methods; Vladimir Zelevinsky, for general nuclear structure; Filomena Nunes, Ian Thompson, and Kathryn Wimmer, for reaction calculations of ^{30}Mg(t,p); and Alexandra Gade, Paul Mantica, Wolfgang Mittig, and Michael Thoennessen, for interpretations of experimental data.

The U.S. Department of Energy National Nuclear Security Administration Stewardship Science Graduate Fellowship program and the Krell Institute funded the majority of my graduate career and provided unique opportunities. I benefited greatly from interaction with personnel from the DOE and national labs, and also with my peers in the SSGF program. My practicum at Lawrence Livermore National Laboratory was a formative experience, and I gained new perspectives on nuclear structure

research from the Nuclear Theory and Modeling Group. I would like to single out my advisor for the practicum, Erich Ormand, for his guidance and support during and after my time at LLNL. For additional funding, I thank the NSCL, the Department of Physics and Astronomy, the College of Natural Science, and the Council of Graduate Students.

In addition to those who directly influenced this research, I would like to thank those people who contributed significantly to the successful completion of my degree from Michigan State. The nuclear theory group at the NSCL offered a wonderful environment with a supportive staff that facilitated my development. Shari Conroy and Lin Leslie were instrumental for their coordination of day-to-day affairs, enabling me to focus solely on research. The collaborative nature of the NSCL and the consistent visits by researchers from around the world expanded my knowledge and emphasized comparisons between my work and results obtained in experiments or in other theoretical approaches.

From the Department of Physics and Astronomy, I must thank the Chair, Wolfgang Bauer, the Secretary for Graduate Student Affairs, Debbie Barratt, and the Graduate Program Director, Scott Pratt. In addition, I am particularly indebted to the former Graduate Program Director, Bhanu Mahanti, for his guidance and his role in my teaching experience. I thank all the instructors of my graduate classes that have given me the foundation for a career in physics. I have benefited greatly from my fellow graduate students at Michigan State, not only from discussions regarding research and homework but also from the relationships cultivated, especially those which have spanned my entire graduate career.

Finally, I thank those who were not present in East Lansing during my stay, but provided support and encouragement throughout the years. If not for my family, I would have been unable to undertake this project and succeed. I thank you all, but especially my parents, Jon and Judy.

TABLE OF CONTENTS

LIST OF TABLES

LIST OF FIGURES

Chapter 1

Introduction

Because of the complexity of the nuclear many-body problem, the time-independent Schrödinger equation

$$H\Psi = E\Psi \tag{1.1}$$

cannot be solved exactly for more than a few particles. However, over 3000 nuclei have been measured (and another 4000 are expected to exist), with nearly all outside the range of exact ab initio methods. In order to provide theoretical estimates of nuclear properties, various methods have been developed to approximate the time-independent Schrödinger equation. Configuration Interaction (CI) method and Energy Density Functional (EDF) methods are two commonly used sets of nuclear structure techniques that expand the range of theoretical calculations beyond the lightest-mass region of the nuclear chart.

1.1 Configuration Interaction Method

The Configuration Interaction method, including the nuclear shell model [1], [2], simplifies the nuclear problem by selecting an inert core of occupied single particle levels with mass number A_c as a vacuum with zero point energy. The entire description of occupied particles is contained in a model space of valence orbits outside the core, reducing the problem from A-body to A_{val}-body, where $A_{val} = A - A_c$. One effect of this reduction in the allowed configuration space (i.e. reduction in degrees of freedom) requires the modification of the Hamiltonian. The interactions between nucleons in the model space must take into account effects outside of the model space, both from the core and from higher energy orbits which are not included in the valence space.

The utility of the CI method depends upon a single particle picture that simplifies the nuclear many-body problem. In this model, the A nucleons produce a mean field that binds them in the nucleus, and a one-body potential can be used to represent the complicated effects of the nuclear interaction. Mathematically, the trick is to rewrite the nuclear Hamiltonian

$$H = T + V = \sum_{i=1}^{A} t(r_i) + \sum_{\substack{i,j=1 \\ i<j}}^{A} v(\mathbf{r_i}, \mathbf{r_j}) + \ldots, \tag{1.2}$$

where the ellipsis refers to many-body forces up to $A-$body, as

$$H = [T + V_{mf}] + [V - V_{mf}], \tag{1.3}$$

where the mean field potential V_{mf} is chosen as a single particle interaction such that

$$V_{mf} = \sum_{i=1}^{A} v(\mathbf{r_i}). \tag{1.4}$$

The mean field Hamiltonian $H_0 = T + V_{mf}$ is usually selected so that the many-body system is reasonably approximated by the exact solution to the Schrödinger equation. In this way, $H_1 = V - V_{mf}$ is small relative to H_0 and can be treated as a perturbation with well-established many-body perturbative techniques. The A-body problem in the mean field is solved by separating the Schrödinger equation

$$H_0 \Psi_0(\mathbf{r_1}, \mathbf{r_2}, \ldots, \mathbf{r_A}) = E_0 \Psi_0(\mathbf{r_1}, \mathbf{r_2}, \ldots, \mathbf{r_A}) \tag{1.5}$$

into A identical one-body equations

$$h(\mathbf{r})\psi_\alpha(\mathbf{r}) = \epsilon_\alpha\psi_\alpha(\mathbf{r}), \tag{1.6}$$

where $h(\mathbf{r}) = t(r) + v(\mathbf{r})$, α is a representation of the complete set of quantum numbers that solve the single particle states, and

$$\Psi_0(\mathbf{r_1}, \mathbf{r_2}, \ldots, \mathbf{r_A}) = \sqrt{\frac{1}{A}}\mathcal{A}\psi_{\alpha_1}(\mathbf{r_1})\psi_{\alpha_2}(\mathbf{r_2})\ldots\psi_{\alpha_A}(\mathbf{r_A}) \tag{1.7}$$

is a Slater determinant of single particle wavefunctions obtained from the antisymmetrization operator $\mathcal{A}$. The energy is then given by

$$E_0 = \sum_{i=1}^{A}\epsilon_{\alpha_i}. \tag{1.8}$$

A typical mean field potential includes a central term, the Coulomb interaction, and a spin-orbit term as given by the one-body potential

$$v(r) = v_{HO}(r) + v_C(r) + v_{LS}(r)\mathbf{L}\cdot\mathbf{S}, \tag{1.9}$$

where the central term is a harmonic oscillator potential. A Woods-Saxon potential $v_{WS}(r)$ is often used instead of $v_{HO}(r)$ without significant modifications. The potentials can be determined phenomenologically, or can be produced in a more microscopic way. From Suhonen [3], for example,

$$v_{HO}(r) = -V_1 + \frac{1}{2} m_N \omega^2 r^2 \tag{1.10}$$

$$v_{WS}(r) = \frac{-V_0}{1 + e^{\frac{r-R}{a}}} \tag{1.11}$$

$$v_{LS}(r) = V_{LS}^{(0)} \frac{r_0^2}{\hbar^2 r} \frac{dv_{WS}(r)}{dr} \tag{1.12}$$

$$v_C(r) = \frac{Ze^2}{4\pi\epsilon_0} \begin{cases} \frac{1}{r} & r > R \\ \frac{3-(r/R)^2}{2R} & r \leq R \end{cases} \tag{1.13}$$

with constants $R = r_0 A^{1/3} = 1.27 A^{1/3}$ fm, $a = 0.67$ fm, $V_0 = (51 \pm 33\frac{N-Z}{A})$ MeV, with + for protons and − for neutrons, and $V_{LS}^{(0)} = -0.44$. A comparison between results with the Woods-Saxon and harmonic oscillator central potentials is used to determine V_1 and $\hbar\omega$, by matching the depth and single particle spacing of the two potentials, respectively. With the one-body potential of Eq. 1.9, the mean field is given by Fig. 1.1. The solution of the one-body Schrödinger equation with the given one-body potential results in the quantum numbers $\alpha = (n, \ell, j, m_j)$ due to the combination of central and spin-orbit interactions (see [4], or another standard quantum mechanics textbook). A schematic description of the lowest single particle states is shown for ^{132}Sn in Fig. 1.2, including a solution with only the harmonic oscillator potential and the evolution of the single particle spacing when the spin-orbit potential is added. The solution with the harmonic potential gives an energy dependence on the main quantum number $N = 2n + \ell$ only, producing large gaps of energy between oscillator shells (i.e., orbits with the same value of N). A complete description of the harmonic oscillator single particle basis can be found in [4] or [3], but it is important to note three qualities:

(i) the degeneracy of the N^{th} shell, including two spin states for each nucleon, is given by $g(N) = (N + 1)(N + 2)$,

(ii) the parity is determined by $(-1)^{\ell}$, and

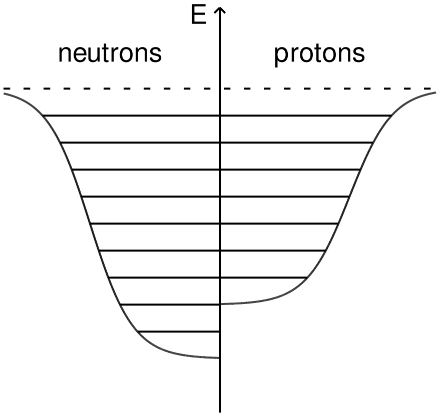

Figure 1.1: Schematic view of single particle orbits for protons and neutrons bound in a one-body mean field potential.

(iii) in one shell, ℓ takes the values $N, N-2, \ldots, 0$ for positive parity and $N, N-2, \ldots, 1$ for negative parity.

Hence, the $N = 0$ shell is given by the $0s$ orbit and has positive parity, the $N = 1$ shell consists of the $0p$ orbits and has negative parity, the $N = 2$ shell consists of the $0d$ and $1s$ orbits and has positive parity. As determined empirically by Blomqvist and Molinari [5], the spacing of oscillator shells is dependent on mass and can be approximated by $\hbar\omega = (45A^{-1/3} - 25A^{-2/3})$ MeV to reproduce experimental measurements.

The characteristic gaps between certain numbers of neutrons and protons result in "magic numbers" that require a relatively large amount of energy to excite a nucleon into the next highest orbit. For the harmonic oscillator potential, restricting to one type of nucleon, the magic numbers are $2, 8, 20, 40, 70,$ and 112. As determined experimentally, agreement is only achieved for lighter nuclei, as these magic numbers should be $2, 8, 20, 28, 50, 82,$ and 126. The strong spin-orbit force in nuclear physics, relative to the atomic case for instance, is essential for a treatment of the nuclear problem, and results in splitting on the order of single particle energy differences as seen in Fig. 1.2. With the choice of parameters listed above from [3], the experimental magic numbers are reproduced.

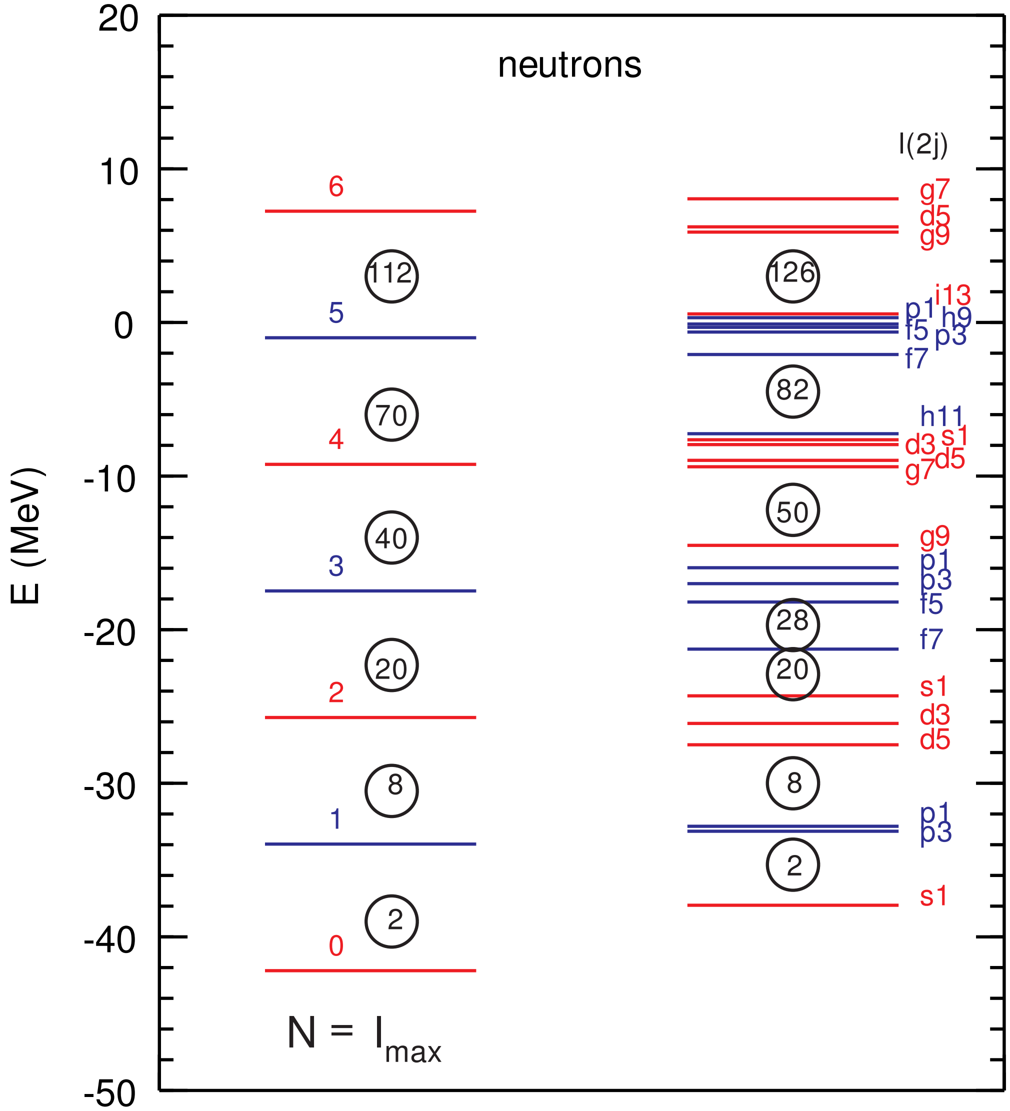

Figure 1.2: Schematic view of the single particle states in ^{132}Sn with a harmonic oscillator mean field and the splitting that occurs with the addition of a strong spin-orbit potential.

The main approach of the CI method proceeds via a reduction to A_{val} particles by selecting a core with magic numbers for protons and neutrons separately. The valence space orbits should be chosen such that low-lying states of nuclei beyond the core can be reproduced. Standard model spaces include the major oscillator shells, named according to the composition of their orbits. Thus, the $N = 0, 1, 2, 3$ shells correspond to the s, p, sd, pf model spaces, respectively. For instance, ^{16}O, with $N = Z = 8$, represents a good core and has been used extensively for calculations from $A = 16$ to $A = 40$ within the sd model space. After selecting a core and model space, two problems remain: finding an effective interaction and solving an eigenvalue problem in the model space. Research through many decades has provided guidance. To solve the eigenvalue problem, various shell model codes have been developed such as OXBASH [6], ANTOINE [7], NUSHELL [8], and NUSHELLX [9].

The effective interaction determines the accuracy of the method, assuming an appropriate core and model space and sufficient computing resources. The earliest shell model calculations [10] used a simple square well potential between nucleons, but fifty years of research have led to better interactions. The established shell model codes require an interaction in the form of single particle energies (SPE) and two-body matrix elements (TBME), given by $\langle ab | V | cd \rangle_{JT}$, where a, b, c, d are single particle orbits, V is an effective two-body interaction, and J and T are the spin and isospin of the coupled nucleons. Chapter 4 will discuss in detail the determination of SPE; for standard model spaces with a stable core, the experimental energy difference between the core with A particles and states in $A + 1$ nuclei provide reasonable SPE since the lowest-energy experimental states can be approximated as single particle states. The TBME should be determined, as discussed in [11] and [12], through a procedure that:

(i) utilizes a microscopic nucleon-nucleon interaction

(ii) overcomes the strongly repulsive short-range part of the interaction via renormalization group methods

(iii) employs many-body perturbative techniques to renormalize the interaction

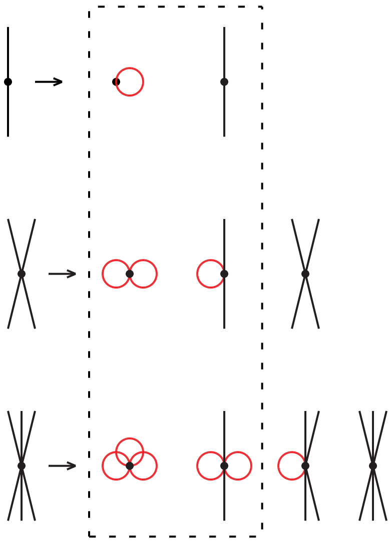

Figure 1.3: A schematic diagram from [13] of the Hamiltonian obtained from an application of Wick's theorem to a closed shell target. The black lines represent valence particles and/or holes, while the red circles represent a summation over orbitals occupied in the target.

into the model space, accounting for configurations outside the model space.

Each component of this procedure will be covered later, in Sections 1.3, 1.4, and 1.5, respectively.

The immediate shortcoming of this approach is the exclusion of many-body forces present in the nuclear Hamiltonian H. As has been found by many studies, notably in [14], three-body forces are approximately one order of magnitude smaller than two-body forces but contribute significantly to the total binding energy of nuclei. In the typical procedure discussed above, the only inclusion of many-body forces occurs implicitly through the experimentally-determined SPE. Truncating at the three-body level, the Hamiltonian is represented diagrammatically by the leftmost column of Fig. 1.3. All three diagrams contain an effective zero-body component and a one-body component, which lie within the dashed black box and can be described reasonably via single particle energies, as discussed in Chapter 4. Two-body matrix elements, as derived from a microscopic nucleon-nucleon interaction by the procedure above, include only the explicit two-body component of Fig. 1.3 but can produce reasonable results for few particles outside the core. As more valence particles are added, the effect of many-body forces increases, along with the deviation from experiment. To counteract this deviation, effective interactions have been derived in the standard model spaces by parameterizing the SPE and TBME and by determining the nuclear Hamiltonian through a fit to experimental levels in the model space, such that all components of Fig. 1.3 except the explicit three-body term are effectively included. Following this procedure, the USDB and USDA interactions were produced in the *sd* model space, varying 66 parameters to fit over 600 energy levels with a root mean square (rms) deviation of 130 keV and 170 keV, respectively [15]. Similar procedures were performed by Cohen and Kurath in the *p* shell [16] and Honma et al. in the *pf* shell [17]. While these effective interactions lose connection to the underlying physics in the nuclear Hamiltonian, they account for many-body forces through their modification of SPE and TBME. Calculations with a shell model code throughout the standard model spaces agree with experiment on the order of the rms deviation of the effective interactions. The most accuracy achieved to date is the 130 keV rms deviation with the USDB interaction, while the Cohen and Kurath interaction has a 400 keV rms deviation [16].

1.2 Energy Density Functional Methods

The concept of the mean field has already been introduced. Hartree-Fock [18], [4] and other self-consistent mean field methods apply the variational principle from quantum mechanics to minimize the total energy of a system and construct the ground state wavefunction. Density Functional Theory (DFT), as developed in condensed matter physics and quantum chemistry [19], [20], is derived with a variational procedure in a similar way to the Hartree-Fock method, except that the density is the basic variable. DFT springs from the Hohenberg-Kohn theorems, which state that:

(i) the ground state properties of a many-particle system are uniquely determined by the local density of the system, and

(ii) for a given Hamiltonian, a universal energy density functional exists that defines the ground state when minimized.

Unfortunately, the theorems provide no insight on how to determine the functional. DFT reduces the many-body problem to a system of non-interacting particles in an effective potential, similar to the mean field methods discussed previously. Due to this simplification, a single Slater determinant can be used to minimize the functional. The Slater determinant is only a reference state, and therefore DFT is considered wavefunction independent.

The problem is not as simple in nuclear physics. As particle number changes from closed-shell to midshell, the ground state undergoes a phase transition due to pairing, giving rise to collective modes. As a result, symmetry-breaking reference states are implemented in the EDF minimization, which have not been proven to satisfy the Hohenberg-Kohn theorems. For this reason, methods which follow a similar procedure to DFT will be called single-reference EDF (SR-EDF), or more generally EDF methods, in order to distinguish from DFT.

Such a formulation is attractive particularly in nuclear physics, since the nuclear Hamiltonian is not known explicitly. The general prescription writes the energy

$$E[\rho] = \int d\mathbf{r}\mathcal{E}[\rho(\mathbf{r})] \tag{1.14}$$

where ρ is the one body density matrix with elements ρ_{ij} given by

$$\langle \psi \mid a_j^\dagger a_i \mid \psi \rangle. \tag{1.15}$$

Since the wavefunction can break symmetries such as particle number, the functional can also include terms with the anomalous density- or its conjugate- with elements κ_{ij} given by

$$\langle \psi \mid a_j^\dagger a_i^\dagger \mid \psi \rangle. \tag{1.16}$$

Determining the form of the nuclear functional is a problem currently under investigation by groups throughout the world [21], [22], and is a goal of the U.S. Department of Energy UNEDF collaboration [23], [24]. However, two common empirical approaches developed by Decharge and Gogny [25] and Skyrme, Vautherin, and Brink [26], [27] have been the basis for the majority of nuclear physics applications of EDF methods. In this work, only the latter approach of functionals, termed Skyrme EDFs, will be used. The Skyrme EDF is given by local terms up to second order in ρ and its derivatives around $r = r'$ for both isospin channels T as:

$$\begin{aligned}\mathcal{E}[\rho] = \sum_{T=0,1} \Big[& C_T^{\rho} \rho_T^2 + C_T^{S} \mathbf{S_T} \cdot \mathbf{S_T} + C_T^{\Delta\rho} \rho_T \Delta \rho_T \\ & + C_T^{\Delta S} \mathbf{S_T} \cdot \boldsymbol{\Delta} \mathbf{S_T} + C_T^{\tau} (\rho_T \tau_T - \mathbf{j_T} \cdot \mathbf{j_T}) + C_T^{ST} (\mathbf{S_T} \cdot \mathbf{T_T} - J_T^2) \\ & + C_T^{\nabla J} (\rho_T \nabla \cdot \sum_{ijk} \epsilon_{ijk} J_T^{jk} \cdot r_i + S_T \cdot \nabla \times \mathbf{j_T}) + C_T^{\nabla S} (\nabla \cdot \mathbf{S_T})^2 \Big] \end{aligned} \tag{1.17}$$

where $\mathbf{S}$ is the spin density, $\mathbf{r}^2 = \sum_{i=1}^{3} r_i^2, \tau_T(\mathbf{r}) = \nabla' \cdot \nabla \rho_T(\mathbf{r}, \mathbf{r}') \mid_{\mathbf{r}=\mathbf{r}'}$ is the kinetic density, $\mathbf{T_T}(\mathbf{r}) = \nabla' \cdot \nabla \mathbf{S_T}(\mathbf{r}, \mathbf{r}') \mid_{\mathbf{r}=\mathbf{r}'}$ is the kinetic spin density, $\mathbf{j_T}(\mathbf{r}) = \frac{i}{2}(\nabla' - \nabla)\rho_T(\mathbf{r}, \mathbf{r}') \mid_{\mathbf{r}=\mathbf{r}'}$ is the current, and $J_T(\mathbf{r}) = \frac{i}{2}(\nabla' - \nabla) \otimes \mathbf{S_T}(\mathbf{r}, \mathbf{r}') \mid_{\mathbf{r}=\mathbf{r}'}$ is the spin current.

Although complicated, the description can be simplified by connecting these coupling constants to the parameters of the Skyrme mean field interaction, as originally derived in [26]. There is an explicit correspondence between the C_T coupling constants and the so-called (t, x) parameterization of the Skyrme interaction, as related by Stoitsov et al. [28]. In general, Skyrme EDFs are expressed in terms of the (t, x)

Table 1.1: Values of parameters for the Skx and Skxtb interactions.

Parameter	Skx	Skxtb
α	1/3	1/3
χ_w	0	0
χ_c	0	0
t_0	-1445.3	-1446.8
t_1	246.9	250.9
t_2	-131.8	-133.0
t_3	12103.9	12127.6
W_0	148.6	153.1
x_0	0.340	0.329
x_1	0.580	0.518
x_2	0.127	0.139
x_3	0.030	0.018

parameters of the mean field interaction. The Skyrme interaction is given by

$$\begin{aligned} v_{skyrme} &= t_0(1+x_0P_\sigma)\delta + \frac{1}{2}t_1(1+x_1P_\sigma)(\mathbf{k}^{*2}\delta + \delta\mathbf{k}^2) \\ &+ t_2(1+x_2P_\sigma)\mathbf{k}^* \cdot \delta\mathbf{k} + \frac{1}{6}t_3(1+x_3P_\sigma)\rho^\alpha(\mathbf{R})\delta \\ &+ iW_0(1+\chi_w P_\tau)\mathbf{k}^* \cdot \delta(\sigma \times \mathbf{k}) + V_{coulomb} \\ &+ S_{12}\sum_{i,T} W_{i,T}\{1 + \frac{3}{r_i} + \frac{3}{r_i^2}\}\frac{e^{-r_i}}{r_i} \end{aligned} \tag{1.18}$$

where $\delta = \delta(\mathbf{r}-\mathbf{r}'), \mathbf{R} = (\mathbf{r}+\mathbf{r}')/2, \mathbf{k} = \frac{1}{2i}(\nabla - \nabla'), \mathbf{k}^*$ is the adjoint of $\mathbf{k}, P_\sigma$ is the spin-exchange operator, and $S_{12} = 2\left[3\frac{(\mathbf{S}\cdot\mathbf{r})^2}{r^2} - \mathbf{S^2}\right]$ is the tensor operator. The last line of Eq. 1.18 is a particular parameterization of the tensor force, which is not always included in the description of the Skyrme interaction.

Without the tensor force, the interaction has twelve parameters (t_i, x_i for $i = 0, 1, 2, 3; \alpha; W_0; \chi_w$; and χ_c, a parameter from the Coulomb interaction) that can be fit to data. In general, the χ_w and χ_c parameters are fixed from physical considerations, and therefore ten parameters are varied. The parameters are given for the Skx interaction [29] in Table 1.1, as an example.

Especially away from stability, the tensor force plays an important role in the properties of nuclei. A Skyrme force including the tensor interaction was fit with the

Skx values as the initial parameters. The new parameterization, Skxtb [30], was refit to the same data as Skx and is also displayed in Table 1.1.

With either parameterization, the energy can be found from a Hartree-Fock-like minimization [18], which proceeds self-consistently in few iterations for spherical closed-shell nuclei. The correspondence between the energy density functional and the two-body interaction enables the minimization to be performed with respect to either description. This is a particularly useful property of the Skyrme functional which does not generally hold: while any Hamiltonian can be described in the ground state by some energy density functional, a pure Hartree-Fock solution of the Hamiltonian need not reproduce the minimization of the EDF. This convenient property of the Skyrme functionals will be exploited so that a so-called Skyrme Hartree-Fock equation can be solved, without recourse to the functional form. When EDF methods are employed in this work, they will utilize the Skyrme interaction, solved in coordinate space on a mesh.

While Skyrme EDFs are convenient and commonly used in the nuclear structure community, a microscopic EDF that connects to the underlying two- and three-body interactions is ultimately desired. The results in this work are dependent on single particle energies calculated with Skyrme functionals, which are unreliable and deviate significantly from experiment, as will be seen in Chapter 4. Improved single particle properties could be implemented directly into the procedure described in Chapter 2, and could be obtained from a microscopic description of the functional. The derivation of microscopic EDFs is beyond the scope of this work, but is of great interest for the applications in the following chapters.

1.3 Microscopic Nucleon-Nucleon Potentials

Several nucleon-nucleon potentials that reproduce elastic scattering phase shifts have been derived. Experimental data up to 350 MeV exists in a variety of channels and for all three types of interaction (proton-proton, proton-neutron, and neutron-neutron). The potential is not identical for the three cases; even after accounting for the primary cause of the difference due to the charge of the proton via the Coulomb force, small deviations between the three cases still exist. The difference between neutron-neutron and proton-proton scattering relates the charge asymmetry of the strong force, and is due to a charge-symmetry-breaking (CSB) interaction. Similarly, a difference between proton-neutron scattering and the average of proton-proton and neutron-neutron scattering relates the charge dependence of the interaction due to a charge-independence-breaking (CIB) interaction.

The derived potentials all have a common feature: strong short-range tensor forces and repulsion (the "hard core" of the nucleon-nucleon interaction) result in highly correlated many-body wavefunctions and highly non-perturbative few- and many-body systems [31]. As a result, many-body perturbative approaches cannot be applied directly to microscopic nucleon-nucleon potentials to produce valence shell interactions, as is done in chemistry for instance. There is not a single potential that can be derived to explain low-energy phemonema, as evidenced by the several potentials that fit low-energy scattering data. In fact, there are an infinite number of potentials that can be developed which deviate at higher energies but match the scattering data. The differences in the two-body potentials result in unique many-body forces for each potential. If the other degrees of freedom are included or calculations are limited to low-energy behavior due to two-body forces, the choice of two-body potential will not affect the results. Due to developments in many-body perturbative techniques, a two-body potential without a hard core is desired, such that model space interactions can be produced for use in further calculations. As has been discussed in detail [31], any potential can be evolved to reduce the high-momentum components (see Section 1.4). As a result, the starting potential can be any derived microscopic nucleon-nucleon potential, regardless of the hard core behavior, if renormalization group methods are applied.

Results throughout this work will be obtained from the microscopic NN potentials N3LO [32] and Argonne v_{18} [33]. The N3LO [32] interaction is derived from chiral effective field theory (χEFT), beginning with the underlying quark physics expressed through quantum chromodynamics (QCD). One advantage of χEFT is that two- and three-body forces are generated on equal footing at a given order of perturbation theory, such that the description can be continually improved by extending the calculation to higher orders of perturbation. As a low-momentum expansion based on a sharp cutoff in momentum (500 MeV in [32]), χEFT provides a theoretical error at a given order of perturbation by varying the cutoff. For N3LO, the uncertainty in the two-body interaction due to contributions from higher orders is 3% [32]. As the cutoff is decreased, the potential softens but the error increases. The cutoff cannot be increased to reduce the error indefinitely, since a resolution scale is set by the explicit treatment of long-range physics [31]. The 500 MeV cutoff is a reasonable compromise between the pion mass which needs to be treated explicitly and the rho meson mass which can be treated effectively through contact terms. The current status of derivation is fourth order or next-to-next-to-next-to-leading order (hence N3LO) for the NN potential, while the NNN potential has only been derived at the N2LO level. In all, 29 parameters are varied to reproduce 4400 data points for two-body elastic scattering with $\chi^2 \approx 1$.

The Argonne v_{18} potential [33] is composed of eighteen local operators expected to contribute to the nucleon-nucleon interaction, such as central, spin-orbit, tensor, etc. and includes fourteen charge-independent terms, a CIB interaction via three charge-dependent terms, and a CSB interaction via one charge-asymmetric term. The potential is solely a function of the separation variable r in each partial wave, causing a strong short-range repulsion in S-waves and strong coupling between low- and high-momentum modes [31]. In all, 40 parameters are varied to reproduce 4300 scattering data with $\chi^2 \approx 1$. A set of companion NNN potentials, called the Illinois models, have been developed and provide good agreement for light nuclei with exact ab initio methods [14].

As mentioned, many-body perturbative techniques cannot be applied to the Argonne v_{18} or N3LO potential directly, as the hard core and coupling between low- and high-momentum modes prevent convergent results. To produce an effective interaction in a reduced model space, the microscopic NN potential must be softened with renormalization group methods.

1.4 Renormalization Group Methods

The renormalization of the free nucleon-nucleon (NN) interaction into the nuclear medium can only be calculated using many-body perturbative techniques if the high-energy degrees of freedom are decoupled from the microscopic potential. Renormalization group (RG) methods, an active area of nuclear structure research [31], [11], [34], are designed to explain the decoupling and to transmit the relevant information to the scale of interest through a finite number of parameters [35]. Results in this work will implement two different RG methods, termed the G-matrix technique and the v_{lowk} approach.

The G-matrix technique applies Brueckner theory [36] to determine the ground state of a many-body system from the perturbation due to the microscopic NN interaction. The energy shift in the ground state is obtained by a linked-cluster expansion as expressed by the Goldstone linked-diagram theory [11]. The G-matrix is then defined relative to the microscopic NN potential V by the integral equation

$$G(\omega) = V + V\frac{Q}{\omega - H_0}G(\omega), \tag{1.19}$$

where H_0 is the unperturbed Hamiltonian (without the potential), the Pauli operator Q blocks intermediate states to prevent scattering into orbits occupied in the many-body system, and ω is the starting energy of the two nucleons. The problem can be generalized if Q does not commute with H_0 as assumed here. The expression appears simple, but requires complicated many-body calculations for a solution. The solution is dependent on a cutoff of active single particle states but can be evaluated numerically through an iterative scheme; for full details, see [11].

The v_{lowk} approach eliminates high-momentum modes in the microscopic NN interaction through a sharp cutoff Λ in momentum space. In order to maintain consistency, the effects of the high-momentum modes must be incorporated into the low-momentum behavior of the potential. Instead of merely truncating the potential, the high-momentum modes are integrated out. The condition of consistency is achieved by demanding that the scattering T matrix for the initial potential v_{NN} remain unchanged as the cutoff is lowered, such that

$$\begin{aligned} T(k',k) &= v_{NN}(k',k) + \frac{2}{\pi} P \int_0^\infty \frac{v_{NN}(k',p)T(p,k)}{k^2-p^2} p^2 dp \\ &= v^{\Lambda}_{lowk}(k',k) + \frac{2}{\pi} P \int_0^\Lambda \frac{v^{\Lambda}_{lowk}(k',p)T(p,k)}{k^2-p^2} p^2 dp \end{aligned} \tag{1.20}$$

for all momenta $k, k' < \Lambda$ and

$$\frac{d}{d\Lambda} v^{\Lambda}_{lowk}(k',k) = \frac{2}{\pi} \frac{v^{\Lambda}_{lowk}(k',\Lambda)T(\Lambda,k)}{1-(k/\Lambda)^2} \tag{1.21}$$

from the requirement $dT(k',k)/d\Lambda = 0$ [31]. Since many microscopic potentials reproduce the low-energy scattering data but diverge for higher energies, they will collapse to the same low-momentum potential as the cutoff is lowered to a sufficiently small value ($\Lambda \approx 2.0\ \mathrm{fm}^{-1}$) [37]. The long-range pion exchange of the nuclear force is maintained in the v_{lowk} interaction, while the short-range hard core has been integrated out. The application of either of these RG methods converts the microscopic NN potential into a potential amenable to perturbative techniques.

1.5 Many-Body Perturbative Techniques

The discussion in this work will be limited to time-independent Rayleigh-Schrödinger perturbation theory, although the time-dependent version, which still leads to an energy-independent expansion, will be used in calculations. As discussed in Section 1.1, the Hamiltonian can be split into two terms $H = H_0 + H_1$ by introducing an appropriate one-body mean field potential so that H_1 is small in comparison to H_0. The solution to H_0, where V_{mf} is usually chosen as a harmonic oscillator potential, can be written as a product of single particle wavefunctions $\psi_{\alpha_i}(r)$. A model space of single particle orbits is chosen separately for protons and neutrons with the dimension D. Projection operators

$$P = \sum_{i=1}^{D} \mid \psi_i\rangle\langle\psi_i \mid \tag{1.22}$$

$$Q = \sum_{i \notin D} \mid \psi_i\rangle\langle\psi_i \mid \tag{1.23}$$

defining the model space and excluded space, respectively, span the single particle basis. The solution to the full Schrödinger equation can be projected into the model space such that

$$P \mid \Psi\rangle = \mid \Psi^M\rangle, \tag{1.24}$$

with the transformation back to the exact wavefunction given by the correlation operator χ via [11]

$$\mid \Psi\rangle = (1 + \chi) \mid \Psi^M\rangle. \tag{1.25}$$

The effective interaction in the model space is then given by

$$V_{eff}(\chi) = \hat{Q}(\omega) - PH_1 \frac{1}{\omega - QHQ} \chi V_{eff}(\chi), \tag{1.26}$$

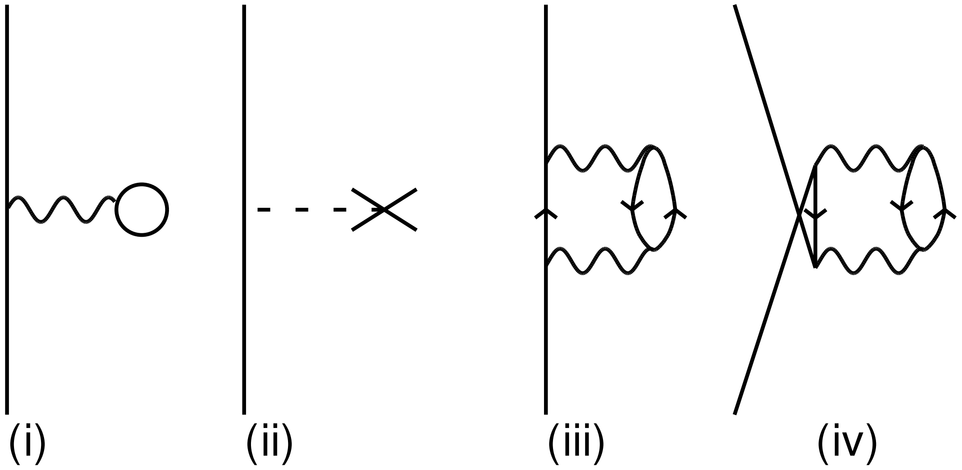

Figure 1.4: One-body Goldstone diagrams included in the evaluation of the $\hat{Q}$-box to second order in perturbation theory: (i) Hartree-Fock, (iii) two-particle one-hole ($2p1h$), and (iv) one-particle two-hole ($1p2h$). The kinetic diagram (ii) does not contribute to the $\hat{Q}$-box but affects the determination of TBME. Only the direct term is depicted for each diagram, but the contribution from exchange diagrams is also included in calculations.

where

$$\hat{Q}(\omega) = PH_1P + PH_1Q\frac{1}{\omega - QHQ}QH_1P \tag{1.27}$$

is the so-called $\hat{Q}$-box and ω is the starting energy defined in Section 1.4. The $\hat{Q}$-box can be expanded into a perturbative form as

$$\hat{Q}(\omega) = PH_1P + P(H_1\frac{Q}{\omega - H_0}H_1 + H_1\frac{Q}{\omega - H_0}H_1\frac{Q}{\omega - H_0}H_1 + \ldots)P. \tag{1.28}$$

For a full derivation of the effective interaction and $\hat{Q}$-box, see [11].

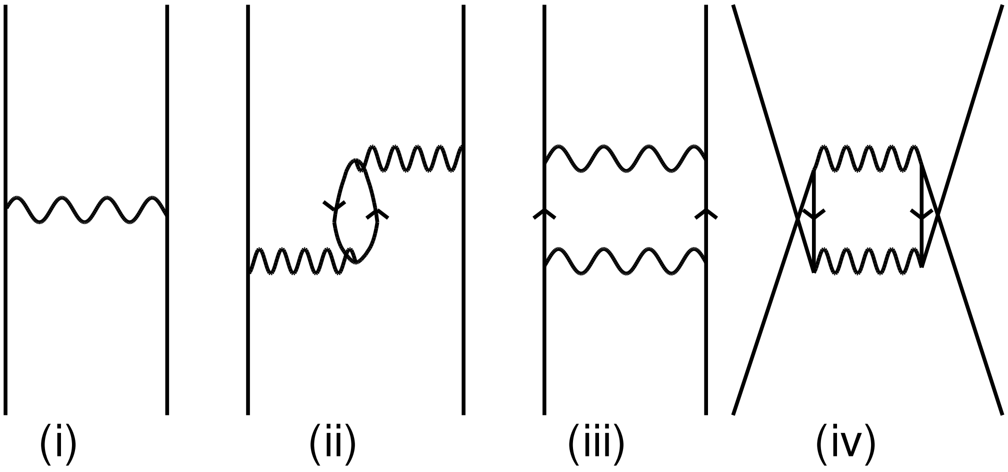

Figure 1.5: Two-body Goldstone diagrams included in the evaluation of the $\hat{Q}$-box to second order in perturbation theory: (i) first order, (ii) core polarization, (iii) particle-particle ladder, and (iv) four-particle two-hole ($4p2h$). Only the direct term is depicted for each diagram, but the contribution from exchange diagrams is also included in calculations.

The equation can be solved in many ways, but the focus here will employ Goldstone diagrams in an iterative scheme with the folded-diagram method. Given the exact $\hat{Q}$-box, the eigenvalues are found from an iterative scheme where

$$\lambda_1 = \omega + \hat{Q}_{exact}(\omega), \tag{1.29}$$

$$\lambda_n = \lambda_1 + \sum_{m=1}^{\infty} \frac{1}{m!} \frac{d^m \hat{Q}}{d\omega^m} (\lambda_{n-1} - \omega)^m \tag{1.30}$$

from [11]. In practice, the exact $\hat{Q}$-box cannot be determined, and time-dependent Rayleigh-Schrödinger theory is necessary to motivate the approximate $\hat{Q}$-box through a folding operator which connects the $\hat{Q}$-box to a wave operator through active model space states. This derivation goes beyond the perfunctory description given here, but can be found in [11] along with the solution to the effective interaction, given by

$$V_{eff}^{(n)} = \hat{Q} + \sum_{m=1}^{\infty} \frac{1}{m!} \frac{d^m \hat{Q}}{d\omega^m} (V_{eff}^{(n-1)})^m \tag{1.31}$$

for a degenerate model space with $V_{eff}^{(0)} = \hat{Q}$. A description of rules to produce and evaluate linked-valence diagrams can be found in [38]. The one- and two-body diagrams for the $\hat{Q}$-box up to second order are included in Figs. 1.4 and 1.5, respectively. The Goldstone diagrams have been derived up to third order as represented in [11] and can be implemented in the renormalization of a microscopic NN potential. In Fig. 1.5, the diagrams are: (i) first order, (ii) core polarization, (iii) particle-particle ladder, and (iv) four-particle two-hole. Without the folding procedure, the effective interaction to second order is given by TBME evaluated as a sum over the four two-body diagrams. The folding procedure essentially blocks some orbits from being accessed, causing (in general) a reduction in the size of the TBME in a summation including contributions to infinite order. The one-body diagrams in Fig. 1.4 produce effective SPE, but experimental values provide better results. The model space interaction, consisting of experimental SPE and TBME from $V_{eff}^{(n)}$ can be used directly in a shell model code.

1.6 Hybrid Methods

CI and EDF methods, as outlined above, have extremely different properties and methods of calculation. The CI method falls under the scope of wavefunction procedures to solve Eq. 1.1, where a given Hamiltonian in matrix form is diagonalized to give eigenvalues and eigenvectors, while EDF methods only require a reference state wavefunction to minimize the energy density functional. The two procedures are desirable for different reasons. The CI method produces a fully correlated model space calculation with simple wavefunctions, expressed for instance as a product of single particle harmonic oscillator wavefunctions. The deviation from experiment depends on the interaction but ranges from 125-400 keV in standard model spaces. It is the most accurate method currently applicable beyond very light and near closed shell nuclei. However, it suffers from limitations in mass and excitation energy, requires an effective interaction for each model space of interest, and has depended on empirical interactions (i.e. effective SPE and TBME) for results in reasonable agreement with experiment. On the other hand, EDF methods use the full single particle space instead of a reduced model space, and produce results for all nuclei with one single parameterization of the functional. The drawbacks of EDF methods are that the form of the functional is not known, the parameterization of a particular form is not universal, dynamic correlations are missing in the standard Skyrme and Gogny functionals, and a full level scheme cannot be calculated with these standard functionals. Recall that in Section 1.2 the discussion was limited to SR-EDF. The biggest disadvantage of EDF methods is the large deviation with respect to experiment, given by an rms deviation of 1.2 MeV for ground states with a Skyrme EDF [23], which can be reduced to 0.6 MeV with additional terms in the functional [39]. Combined with the lack of complete description of excited states, a comparison of theoretical and experimental level schemes is difficult throughout most of the nuclear chart.

In the last few decades, there have been attempts [40], [41] to combine aspects of CI and EDF methods to produce a more robust theory which achieves advantages of both approaches. The ultimate goal seeks to maximize the advantages of each method while minimizing their respective faults. As it happens, the two approaches have distinct advantages and disadvantages which are not mutually attainable. In general, progress has been made in past attempts by groups with expertise primarily in EDF methods, resulting in new approaches lacking many of the advantages of the CI method.

For instance, Bender et al. [40] have produced a symmetry-conserving variational approach called Variation after Mean field Projection In Realistic model spaces (VAMPIR). Like EDF methods, a symmetry-breaking auxiliary wavefunction is varied to determine the lowest-energy states for each spin and parity quantum numbers. The Hamiltonian in the form of TBME is taken from an effective interaction in a standard shell model space; for instance, a modified version of the USD interaction is used in [40]. Correlations are included by expanding the wavefunction around a symmetry-projected ground state via one or two quasiparticle excitations (for odd and even nuclei, respectively) and by diagonalizing the interaction in the resultant basis. Like the CI method, this allows for configuration-mixing, and the restricted calculations that have been performed so far reproduce CI calculations. The application of the VAMPIR approach to heavy nuclei would extend the reach of configuration-mixing diagonalizations beyond the limits of the CI method ($A \approx 100$ as shown in Fig. 1.6). However, the current formulation is dependent on a shell model effective interaction, such that results do not improve upon CI calculations in its region of applicability.

The opposite approach is utilized here, focusing instead on improved determinations of nuclear Hamiltonians as influenced by renormalization group and EDF methods. The main benefit, due to the relative ease of determining nuclear interactions from realistic nucleon-nucleon potentials for any model space of interest, is improved accuracy for nuclei outside of standard shell model spaces. The effective interactions will be used as input to the shell model code NUSHELLX. As a result, an immediate limitation of the approach prevents heavy nuclei ($A > 100$) from being calculated, except those near doubly magic nuclei like ^{100}Sn, ^{132}Sn, and ^{208}Pb.

1.7 Motivation

A chart of nuclides is shown in Fig. 1.6, overlaid by various nuclear structure techniques and their declared ranges of validity. Ab initio approaches, which solve the many-body Schrödinger equation (nearly) exactly with microscopic potentials, are valid only for the lightest nuclei due to computational limitations. The two approximate techniques cover the rest of the chart, with the CI method extending to $A \approx 100$ and EDF methods not limited by mass. While the CI method is computationally applicable in the region shown on the graph, the standard CI method as described in Section 1.1 does not produce satisfactory results throughout this region.

Fig. 1.7 displays results in the *sd* shell with the standard USDB interaction [15]. The interaction is symmetric with respect to isospin, so only nuclei on the neutron-rich side are shown. Good agreement between experiment and theory, on the order of the rms deviation of 130 keV, is seen for all nuclei except $Z \approx 10, N \approx 20$. The advent of rare isotope beams sparked experimental interest in this neutron-rich region, such that a better theoretical description was desired. Brown and Richter [15] included recent experimental data for neutron-rich exotic energy levels in the fitting procedure to create the USDB and USDA interactions, so that they would produce better results for neutron-rich nuclei. Since the connection to microscopic physics is lost in the fitting procedure, the empirical interaction does not have predictive power for nuclei with different shell structure than the experimental data used in the fit. The disagreement for $N = 19$ and $N = 20$ is understood, because these nuclei are in the so-called island of inversion region. The island of inversion is a region of the nuclear chart near the

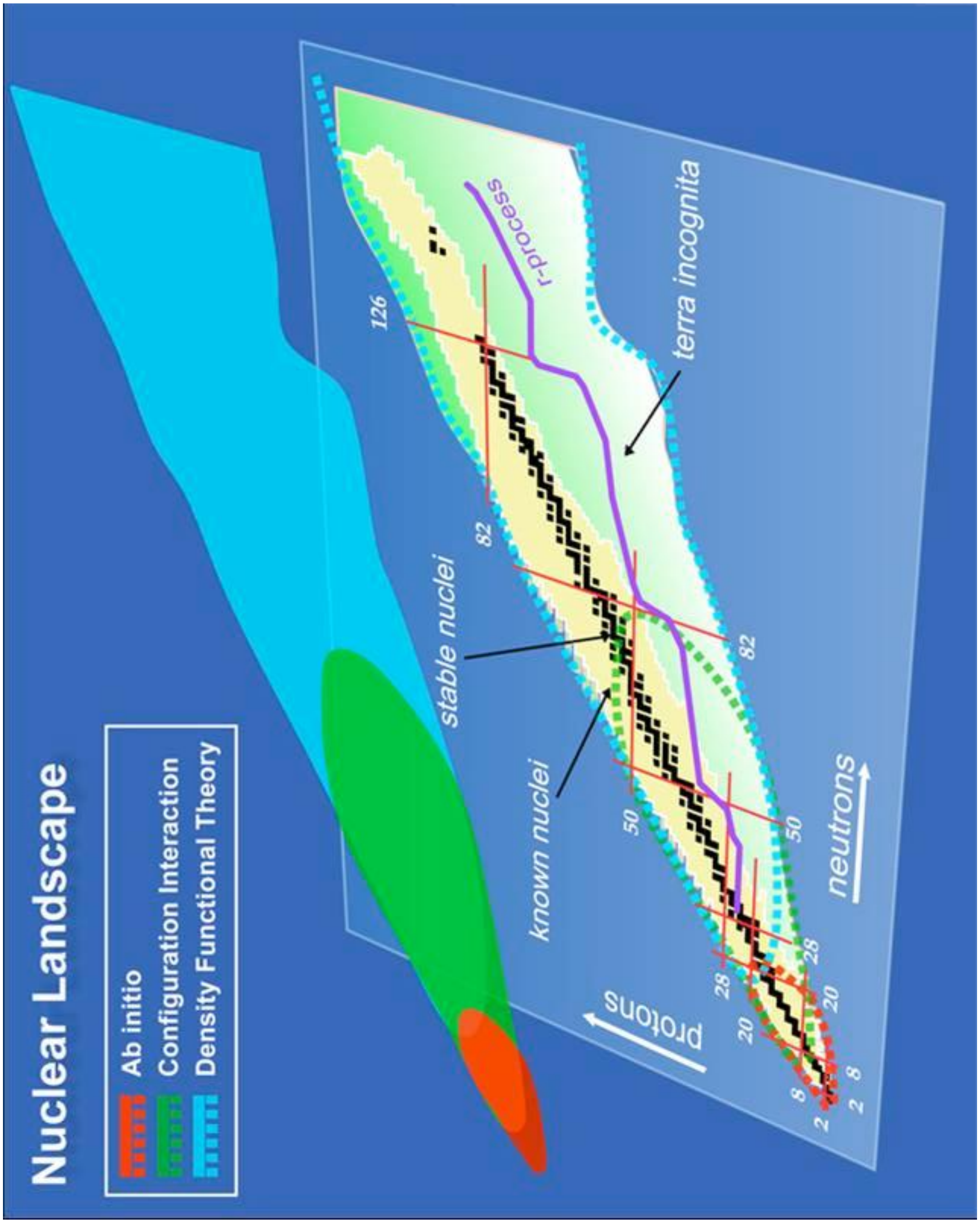

Figure 1.6: A chart of nuclides marked with regions of validity of various nuclear structure approaches. The figure is taken from the UNEDF website [24].

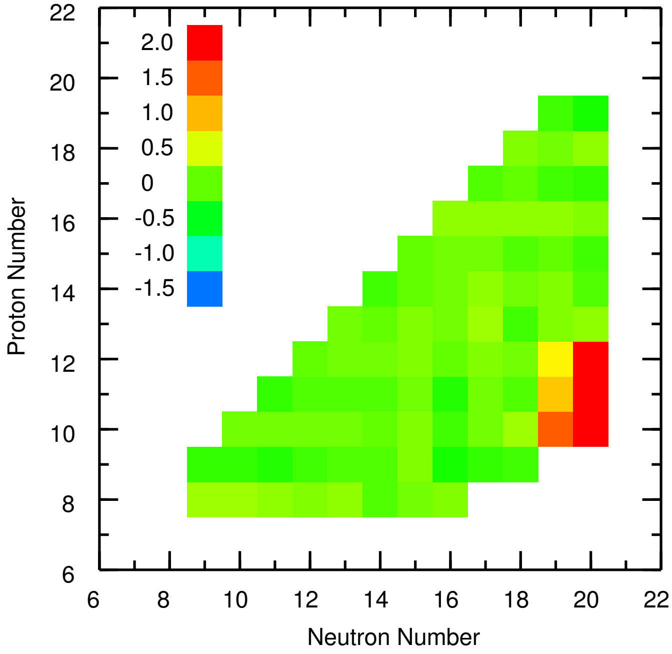

Figure 1.7: A plot of energy differences $E_{USDB} - E_{Exp.}$ in MeV calculated for nuclei in the *sd* shell, as shown by Brown and Richter in Fig. 10 of [15].

supposed shell closure $N = 20$ where pf neutron orbits are filled preferentially over *sd* orbits in ground states. See Section 1.1 and specifically the right side of Fig. 1.2 for a description of the single particle orbits and shell structure. Experimental evidence [42] confirms this picture of inversion, and similar "islands of shell-breaking" have been found or postulated in other regions of the nuclear chart [43], [44]. The lack of inclusion of pf orbits, which create additional correlation energy, results in underbinding in the USDB calculation for the island of inversion region. Even with an improved interaction fit to more neutron-rich data, these nuclei will not be calculated accurately in the *sd* model space. Theoretical results using the standard CI method can often be improved by producing better interactions in a standard model space (for instance, by fitting to more experimental data), but cannot necessarily be applied accurately to all states in the region. Another example of disagreement due to contributions from orbits outside the model space is seen in ^{18}O for the first excited 0^+ state at 3.63 MeV and the lowest 1^- state at 4.46 MeV. In the *sd* model space, which treats ^{16}O as the core and only allows valence particles to fill the positive parity *sd* orbits, negative parity states do not exist and the 1^- state cannot be calculated. The 0^+ state, while positive parity, is a four-particle two-hole excitation from ^{16}O [45], meaning that two *p* shell nucleons are excited into the *sd* shell. The theoretical capabilities can be expanded through an increase in the size of the model space, which requires the creation of a new effective interaction. For empirical interactions, the determination of an effective interaction is a lengthy procedure that requires the compilation of data. Especially with larger model spaces, available data does not span the space and computational resources limit the viability of full calculations.

Another demonstration where reliable results are difficult to obtain with the CI method is given by ^{42}Si. As can be seen from Fig. 1.8, ^{42}Si lies in a neutron-rich region outside of standard model spaces, in the middle of the *sd* shell for proton orbits (y-axis) and in the middle of the *pf* shell for neutron orbits (x-axis). First calculations for ^{42}Si were done in the so-called *sdpf* model space, with active *sd* proton orbits and *pf* neutron orbits. As can be seen from Fig. 1.8, little experimental data is known in this region. Deriving an empirical interaction for this model space cannot follow the procedure discussed in Section 1.1 since the number of parameters (SPE and TBME) is comparable to the number of experimental energy levels. Instead, the proton-proton TBME can be taken from an empirical *sd* shell interaction, and the neutron-neutron TBME can be taken from an empirical *pf* shell interaction, leaving only a cross-shell proton-neutron interaction which can be determined phenomenologically or via RG methods. An early *sdpf* interaction [46] was derived in this way, with improvements made by Nummela et al. [47] as more experimental properties of exotic nuclei were measured. However, such an approach fails due to the evolution of shell structure, as depicted in Fig. 1.9. The plot depicts the excitation energy of the first 2^+ state for both silicon and calcium isotopes from $N = 18$ to $N = 30$. Nuclei with magic numbers of nucleons have a high 2^+ energy relative to their neighbors, since more energy is required to excite a particle below the Fermi sea. The discussion earlier on magic

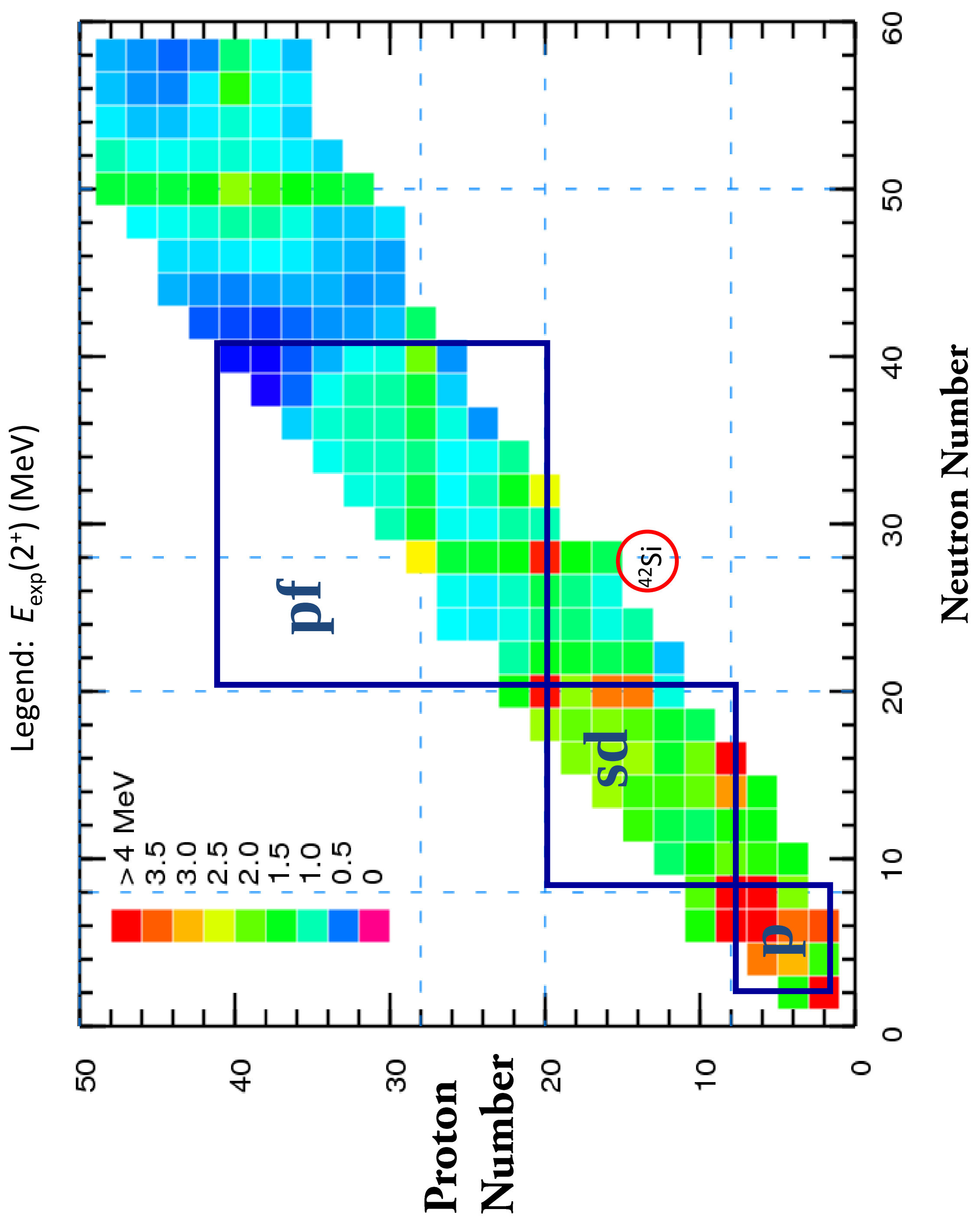

Figure 1.8: A chart of nuclides by 2^+ energy of even-even nuclei, limited to the range of applicability of the CI method. Also included are standard shell model spaces, with ^{42}Si highlighted as an exotic isotope outside of standard model spaces.

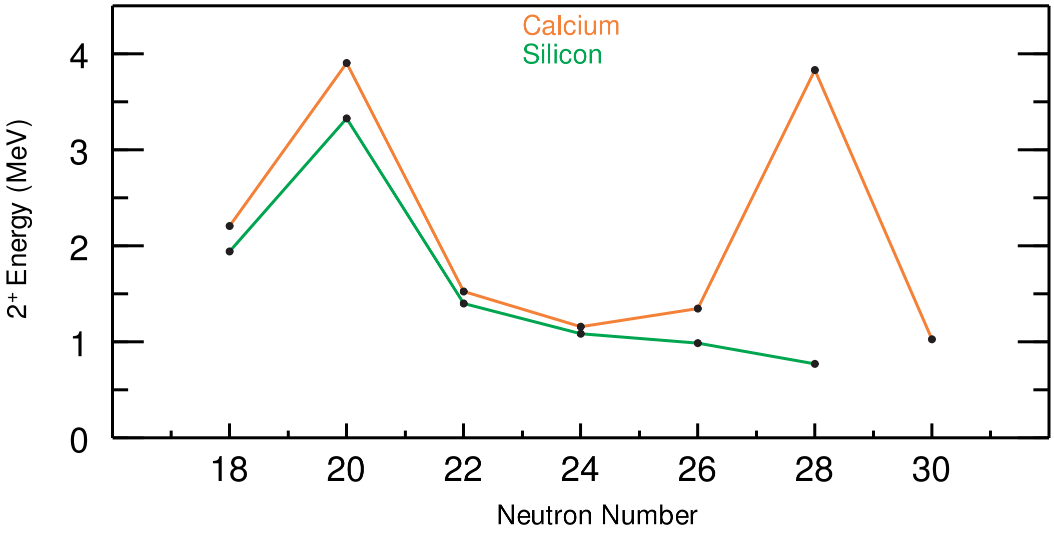

Figure 1.9: Excitation energy of the first 2^+ state in even-even silicon and calcium isotopes as a function of neutron number. Notice the difference in behavior for the supposed magic numbers of $N = 20$ and $N = 28$.

numbers cited 20 and 28 as experimentally determined values. As seen in Fig. 1.9, the peaked behavior is seen at the $N = 20$ shell closure for both ^{34}Si and ^{40}Ca, but the results diverge for $N = 28$. Whereas ^{48}Ca displays the behavior of a good shell closure, the 2^+ energies are similar for ^{40}Si and ^{42}Si (^{44}Si has not been measured). Shell structure evolves near the driplines, where it is no longer energetically favorable to add a neutron or proton (the excess nucleon of a particular type "drips" off the nucleus). As the neutron dripline is approached for neutron-rich nuclei, a change in magic numbers has been observed. The cause could be a weakening of the spin-orbit force (recall from Section 1.1 that $N = 28$ is the first shell closure caused by the spin-orbit force), or a change in the spacing between the p and f orbits in the $N = 3$ oscillator shell. Calculations with the $sdpf$ interaction of Retamosa et al. [46] are nearly 2 MeV too high for the 2^+ state of ^{42}Si. Even with the improvements made by Nummela et al. [47], the SDPF-NR interaction misses the excitation energy of the 2^+ state in ^{42}Si by 720 keV. The neutron-neutron TBME were taken from an empirical fit in the pf shell, therefore mimicking the behavior of pf orbits for stable and near-stable isotopes, like the calcium isotopes. The exotic behavior of the neutron pf orbits must be taken into account in order to calculate nuclei in the $sdpf$ shell such as ^{42}Si. A recent work by Nowacki and Poves [48] developed a new interaction called SDPF-U that empirically accounts for the shell structure of exotic nuclei by having different TBME for $Z \geq 15$ and $Z \leq 14$ (i.e., for stable and unstable shell structure, respectively). The piecewise TBME enable the SDPF-U interaction to reproduce the 2^+ states in ^{42}Si and ^{48}Ca within 50 keV. This topic will be revisited and treated in more detail in Chapter 3.

The goal of this work is to use hybrid methods, specifically an improved determination of effective model space interactions through a renormalization of microscopic NN potentials based on EDF methods, to produce reliable calculations of nuclear properties, especially for nuclei outside of standard shell model spaces which are accessible with current or planned experimental rare isotope facilities.

1.8 Methodology and Layout

Four nuclear structure techniques have been discussed in this introduction which will be implemented into the renormalization procedure; namely, Configuration Interaction theory, Energy Density Functional methods, renormalization group methods, and many-body perturbative techniques. The development of such a procedure would not have been possible without the previous work in these fields, or without the generous collaborative spirit in the nuclear structure community which led to the author's access to Fortran source codes. The renormalization of microscopic nucleon-nucleon potentials into the nuclear medium, implementing both renormalization group methods and many-body perturbative techniques, and including various ingredients (choice of potential, RG method, order of perturbation theory, etc.), had been developed by Morten Hjorth-Jensen and is accessible [49]. Minor modifications to the code were included in order to replace the standard harmonic oscillator radial wavefunctions with those derived from EDF methods and to output the effective interaction into the format required for the shell model codes utilized in this work. These codes, NUSHELLX [9] and OXBASH [6], produce CI calculations and were obtained from Alex Brown. Both codes include a Skyrme Hartree-Fock solver, which employs the equal filling approximation for odd nuclei (see Section 4.4). The renormalization codes [49] have been integrated into the newest version of NUSHELLX [9] by Alex Brown via the "ham" executable, including the modifications developed by the author. The main programming component of this work was the development of an iterative fitting procedure to constrain single particle energies and other parameters, as discussed in Section 5.1. The primary contribution of the author was the development of the renormalization procedure, in conjunction with Alex Brown, as well as the applications to produce effective interactions for nuclear structure calculations discussed throughout this dissertation.

The remainder of this work has the following layout:

(i) Chapter 2 describes the renormalization procedure, and includes an application for comparison to known results in the *sd* shell. Various ingredients of the procedure are varied, and their dependence on the output two-body matrix elements is evaluated.

(ii) Chapter 3 compares the standard harmonic oscillator single particle basis to the realistic Skyrme Hartree-Fock basis and to a mixed basis, consisting of Skyrme single particle energies and harmonic oscillator single particle radial wavefunctions. The effects of the basis on the renormalization procedure are evaluated in the *sdpf* model space with two different target nuclei. This chapter has previously been published [50] with few minor modifications in this work.

(iii) Chapter 4 discusses the meaning of single particle energies, both in the uncorrelated and centroid sense, and distinguishes both types from one-nucleon separation energies. Results are shown for both Configuration Interaction theory and Energy Density Functional methods to illustrate the general behavior of single particle energies, to display their role in effective interactions and nuclear structure calculations, and to emphasize the necessity of accurate single particle energies in effective interactions. Various methods to determine single particle energies for the renormalization procedure are specified at the conclusion of the chapter. Previous publications have included the results of Section 4.2, for the oxygen and fluorine isotopes [51] and for the argon and calcium isotopes [52].

(iv) Applications of the renormalization procedure have produced effective interactions in the island of inversion region and near ^{42}Si, and results obtained with these effective interactions are displayed and compared to experimental data in Chapter 5. The theoretical calculations have been utilized to predict the behavior of nuclei beyond the experimental capabilities with current rare isotope facilities; for instance, the neutron dripline has been determined from the effective interaction in the island of inversion region in Section 5.1. These applications of the renormalization procedure are presented for the first time in this work, but are expected to result in at least one publication, if not more, in 2011 or 2012.

(v) Finally, Chapter 6 provides a conclusion and outlook, focusing on future applications of the renormalization procedure, the potential addition of three-body forces, and further studies of single particle behavior, specifically for the Skyrme interaction.

Chapter 2

Renormalization Procedure

With the various techniques available for nuclear structure described in the introduction, the development of a hybrid method for calculations outside of standard model spaces can be achieved. This chapter will detail the procedure to renormalize a microscopic NN potential into the nuclear medium. The dependence on various aspects of the method, such as the choice of RG method, will be evaluated, and limitations or potential failures of the procedure will be discussed.

The following steps compose the hybrid method, hereafter called the Hybrid Renormalization Procedure (HRP).

(i) *Choose a model space and target nucleus.* The model space is determined by the region of the nuclear chart of interest. For ^{28}Si, for instance, which is in the middle of the *sd* shell, the *sd* model space would be chosen. In principle, the interaction can be determined for any model space. Computational limitations regarding the diagonalization of a matrix in the eventual CI calculation, which depends on the dimension of the matrix that increases with the size of the model space, require a judicious choice of model space as described in Section 1.1. While the core of the CI calculation is determined by the model space, the target nucleus can be inside or outside the model space with only one restriction: the renormalization requires a target with a closed subshell structure in the mean field. The summation over orbits in the Goldstone diagrams distinguishes between particle and hole orbits. Therefore, partially filled subshells, which cannot be classified as particle or hole orbits, are not allowed. Often the core and target will be identical.

(ii) *Calculate properties of the target nucleus in Skyrme Hartree-Fock theory.* The properties of the target nucleus, for instance its binding energy, single particle radial wavefunctions, and single particle energy spectra for protons and neutrons, are calculated with a Skyrme interaction.

(iii) *Choose the ingredients of the renormalization.* The selection of the microscopic potential (Argonne v_{18} or N3LO), renormalization group method (G-matrix or v_{lowk}), basis (to be covered later), order of perturbation theory (up to third order), and number of excitations in $\hbar\omega$ must be set at this stage.

(iv) *Evolve the microscopic potential with the RG method.* As discussed in Section 1.4, the decoupling of high- and low-momentum modes can be achieved, allowing many-body perturbative techniques to act on the low-momentum interaction.

(v) *Renormalize into the model space of interest.* The low-momentum interaction from step (iv), in the form of two-body matrix elements, provides the input for Rayleigh-Schrödinger perturbation theory. The model space interaction, again in the form of TBME, is determined from the calculation of Goldstone diagrams to the order of perturbation theory and number of excitations specified in step (iii).

(vi) *Perform calculations with a shell model code.* Using the TBME from step (v) and the SPE from step (ii), the effective interaction can be used as the input to a CI calculation in available shell model codes with the model space specified in step (i). Results can be compared to experiment.

(vii) *If necessary, make improvements.* If the theoretical results do not provide sufficient agreement with respect to experiment, the procedure can be improved. Due to the poor single particle energies calculated with Skyrme interactions, the SPE of the effective interaction can be taken from experiment or treated as parameters. See Chapters 4 and 5 for details. Other improvements are increases in the order of perturbation theory, the number of excitations, or the size of the model space.

2.1 Bases for Renormalization

In step (iii) of the HRP, the choice of basis is an ingredient to the renormalization. If the renormalization was performed to all orders and infinite $\hbar\omega$, the results would not depend on the basis. With limitations, the renormalization depends on the accuracy of the expansion in terms of a single particle basis. The standard basis is the harmonic oscillator basis, due to its simple analytic form and common use throughout nuclear structure, for example as the basis for shell model calculations. The harmonic oscillator basis is sufficient for most applications, but deviates from the realistic case away from stability. Realistic bases, such as the Woods-Saxon basis, reproduce experimental behavior to first order better, requiring fewer terms in the expansion. Furthermore, the renormalization scheme converges in fewer iterations for a realistic basis in comparison to the harmonic oscillator basis. The HRP utilizes a realistic basis from step (ii) in the procedure, rather than a Woods-Saxon basis, in an effort to maintain consistency and implement EDF methods as completely as possible.

While the basis derived from EDF methods is superior to the harmonic oscillator basis for renormalization, the harmonic oscillator basis is the standard for the nuclear structure community. The basis for renormalization remains an ingredient in the procedure so that a comparison of results with different bases can be achieved. Chapter 3 is devoted to this topic, emphasizing the importance of a realistic basis away from stability. Three bases for the renormalization are considered: harmonic oscillator single particle energies and wavefunctions (HO), Skyrme Hartree-Fock single particle energies and wavefunctions (SHF), and Skyrme Hartree-Fock single particle energies and harmonic oscillator single particle wavefunctions (MIX).

The MIX basis and HO basis give identical results to first order in perturbation theory since they use identical wavefunctions. The second order Goldstone diagrams in Fig. 1.5 are affected to leading order since the energies, which are different in the two procedures, enter higher-order diagrams via energy denominators, as discussed in [11]. The comparison between the MIX and HO bases displays the dependence of the two-body matrix elements on the single particle energies, and will be discussed in Chapters 3 and 4.

The harmonic oscillator basis is given by the solution of the harmonic oscillator mean field potential, as discussed in Section 1.1, without the spin-orbit potential. The wavefunctions are given by

$$\psi_{nlm_l}(\vec{r}) = R_{nl}^{HO}(r) Y_{lm_l}(\theta, \phi), \tag{2.1}$$

and the valence orbits are bound.

Skyrme Hartree-Fock radial wavefunctions, once solved on a mesh as discussed in Section 1.2, are implemented in the renormalization by using an expansion in terms of the harmonic oscillator basis via:

$$\psi_{nlj}^{SHF}(\vec{r}) = \sum_{n} a_n R_{nl}^{HO}(r) [Y_l(\theta, \phi) \otimes \chi_s]_j, \tag{2.2}$$

where a_n^2 gives the percentage of a specific harmonic oscillator wavefunction component in the Skyrme Hartree-Fock wavefunction. The Skyrme Hartree-Fock wavefunctions and single particle energies can only be determined for bound states. For unbound orbits, the harmonic oscillator basis remains in use, but the Gram-Schmidt process is used to ensure orthonormality of the single particle wavefunctions.

The Hybrid Renormalization Procedure, as stated in step (i), can be applied to any model space and closed-subshell target nucleus of interest. A proof of principle can be established by comparing to a standard model space, such as the *sd* model space with ^{16}O as the core and target nucleus, which will also allow for a comparison between different renormalization options, as shown throughout this chapter.

2.2 Application to *sd* Model Space

For the first application, the Hybrid Renormalization Procedure will be studied in a standard model space. The steps will be listed explicitly once to clarify the HRP.

(i) *Choose a model space and target nucleus.* The model space is the *sd* shell and the target nucleus is the doubly magic nucleus ^{16}O.

(ii) *Calculate the target nucleus in Skyrme Hartree-Fock theory.* Using the Skxtb Skyrme interaction [30], the solution to Hartree-Fock equations is found for ^{16}O.

(iii) *Choice of renormalization ingredients.* For this application, the N3LO potential, v_{lowk} RG method, and SHF basis will be used. Rayleigh-Schrödinger perturbation theory will be applied to second order and 6 $\hbar\omega$.

(iv) *Evolve the microscopic potential with the RG method.* Following the procedure in Section 1.4, the N3LO potential is renormalized using v_{lowk}.

(v) *Renormalize into the model space of interest.* Following the procedure in Section 1.5, the low-momentum interaction is renormalized to second order and $6\hbar\omega$.

(vi) *Perform calculations with a shell model code.* NUSHELLX [9] is used to calculate ^{18}O in the *sd* model space with the effective interaction called HRP-SD, comprised of TBME from step (v) and SPE from step (ii).

(vii) *If necessary, make improvements.* For an example, the procedure is repeated with third order in perturbation theory, with the remaining ingredients of the procedure identical. See Section 4.3 for results with improved single particle energies.

The results for ^{18}O are shown in Fig. 2.1. The low-energy spectrum is reproduced reasonably well, while the experimental level density above 3.5 MeV is much higher than the theoretical level density. The negative parity experimental states, as well as positive parity states with an even number of excitations from the *p* shell, cannot be reproduced with the choice of the positive parity *sd* orbits outside the ^{16}O core as discussed in Section 1.7. These excitations of the core occur around 4 MeV, such that the description of valence neutrons outside the ^{16}O vacuum fails. Therefore, the

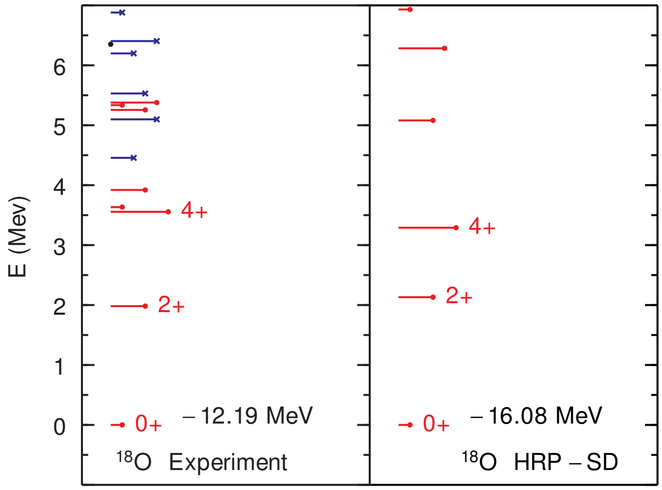

Figure 2.1: Comparison of the level schemes for experiment (left) and for the interaction HRP-SD (right). The color of the lines displays the parity, red for positive and blue for negative. The length of the line corresponds to the angular momentum of the state, with a label each time a highest J value occurs, starting from the ground state. Therefore, the ground state spin is always labeled. The ground state energy of the nucleus relative to the core (^{16}O in this case) is included for both theory and experiment, with the excitation energy of the states independent of the difference in binding energy. Experimental states are taken from the ENSDF database [53] unless otherwise cited. States in the ENSDF database without an assigned J^π value are plotted as black dots at the appropriate energies. The level schemes are displayed up to 7 MeV, although the theoretical level scheme includes a finite number of states for a given J^π value (ten unless otherwise noted). As a result, nuclei with a high density of states might not show the full theoretical level scheme through 7 MeV.

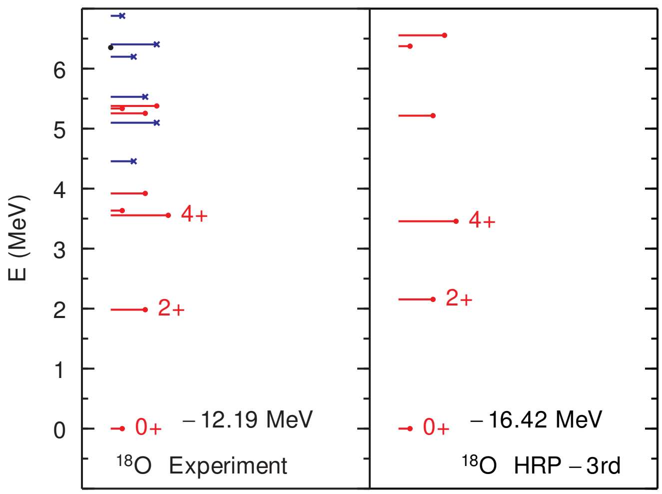

Figure 2.2: Results in comparison to Fig. 2.1, extending the renormalization to third order in perturbation theory. See the caption to Fig. 2.1 for details.

agreement between experiment and theory breaks down at high excitation energy.

The excitation energy of the 4^+ state, as calculated with HRP-SD, is 265 keV lower than experiment. The experimental two-particle 0^+ state at 5.34 MeV occurs at an excitation energy of 6.94 MeV. One possibility for improvement is to produce an interaction HRP-3rd by repeating the HRP to third order in perturbation theory, as discussed in step (vii) of this section. The results are shown in Fig. 2.2. The first excited theoretical 0^+ state now has an excitation energy of 6.37 MeV, 560 keV lower in energy than in Fig. 2.1 but still one MeV higher than experiment. The 4^+ state is calculated 165 keV lower in energy, now with a deviation from experiment of only 100 keV. As the empirical interactions in the *sd* shell produce an rms deviation of approximately 150 keV, as discussed in Section 1.1, the agreement with experiment is now satisfactory. However, in both Figs. 2.1 and 2.2, the binding energy of ^{18}O as determined from the Hybrid Renormalization Procedure is approximately 4 MeV larger than experiment. The small improvement in the excitation energy spectrum as a result of the extension to third order in perturbation theory fails to address a more significant problem in the interaction: the single particle energies from the Skxtb

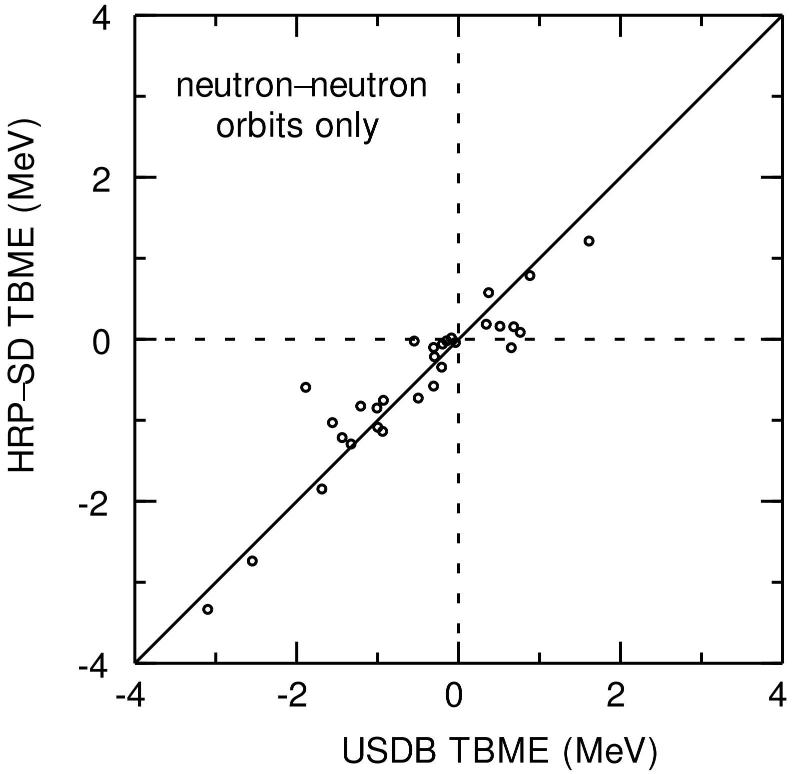

Figure 2.3: Comparison of the neutron-neutron TBME for the microscopic HRP-SD interaction and the empirical USDB interaction. The solid line $y = x$ denotes equivalence between the matrix elements for the two interactions.

interaction are not sufficient for the desired accuracy. The necessary improvement to the HRP in this case requires improved SPE, which necessitates a detailed discussion on the meaning and behavior of SPE. This topic will be revisited in Chapter 4, where a method to determine SPE for the effective interaction will be detailed.

The first nucleus outside the ^{16}O core which depends on the TBME of the interaction is ^{18}O. Thus, it is the simplest case for comparison. To determine the quality of results throughout the *sd* shell, rather than perform lengthy calculations for all nuclei, a comparison to the empirical USDB interaction is sufficient, since it produces good results throughout the *sd* shell (see Fig. 1.7). Because the USDB interaction is symmetric with respect to isospin, while the renormalization procedure includes Coulomb, charge-independence-breaking (CIB), and charge-symmetry-breaking (CSB) interactions, neutron-neutron TBME are best-suited for comparison. Fig. 2.3 shows the neutron-neutron TBME, plotted as HRP-SD vs. USDB. For perfect agreement between the two interactions, all TBME would lie along the line of equality ($y = x$). Instead, it serves as a reasonable trendline, with scattering in both directions on the order of 100 keV. One point, corresponding to the $J = 0\, d_{3/2} - d_{3/2}$ pairing matrix element, disagrees by 1.3 MeV, which would have a significant effect on calculations in the *sd* model space. It should be noted that the TBME are not expected to agree for the two interactions, as the empirical interaction includes contributions from all effects in the *sd* shell, such as many-body forces, while the HRP includes only a renormalization of a microscopic NN potential. Since three-body forces contribute at about an order of magnitude lower than two-body forces and the deviation between the empirical interaction and the microscopic interaction is on the order of 10%, the HRP produces results to the expected accuracy, and the proof of principle is completed.

To avoid treating three-body forces explicitly, which would be very difficult in the procedure delineated above, two approximate methods will be employed. When possible, the nuclei of interest will be close in proximity to the target nucleus on the chart of nuclides given in Fig. 1.8. Skyrme interactions are fit to experimental data to reproduce properties of nuclei throughout the chart of nuclides. As a result, they effectively include three-body effects up to the one-body level through the single particle energies in the SHF basis. As shown clearly in Fig. 7 of [54], the remaining residual three-body force and the effective two-body component of the NNN interaction contribute at another order of magnitude smaller than the effective one-body component. In fact, this is the primary reason for the lack of consistency in the initial interactions, since a Hartree-Fock calculation could be performed on the microscopic NN interaction once the hard core has been softened with an RG method in step (iv) of the HRP. However, a Hartree-Fock calculation with the low-momentum interaction would not include the essential effective one-body component of the three-body

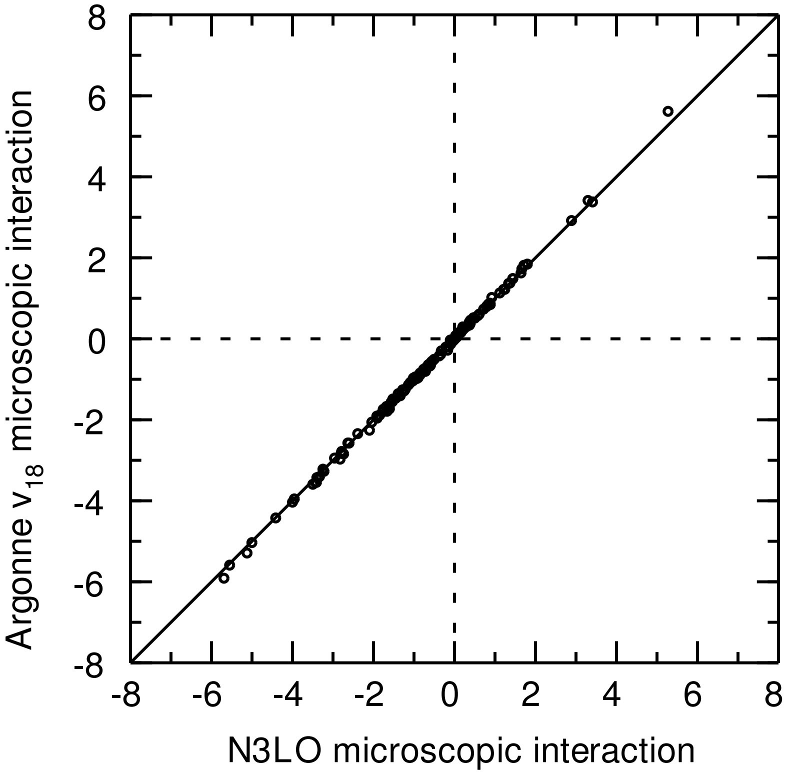

Figure 2.4: Two-body matrix elements when the microscopic nucleon-nucleon interaction in an otherwise identical HRP is the N3LO interaction (x-axis) or the Argonne v_{18} interaction (y-axis).

(and higher) terms of the interaction. If the calculated nuclei are similar to the target nucleus, the three-body effects are approximately taken into account with the SHF basis.

The second method to treat three-body forces implicitly is only employed in this work in Chapter 5. When nuclei far from the target are calculated, the three-body forces are treated by parameterizing the monopole terms of the CI calculation. This will be discussed in detail in Section 5.1.

At this point, the *sd* model space and ^{16}O target will be used to analyze the effects of different parameters in the HRP on the output two-body matrix elements.

2.3 Dependence on Microscopic Interaction

The first ingredient of interest is the choice of the initial microscopic NN interaction. The HRP was performed identically to Section 2.2, except with Argonne v_{18} as the microscopic NN interaction. Fig. 2.4 shows the comparison of all TBME for this new interaction to the HRP-SD interaction. Even though the N3LO and Argonne v_{18} interactions have very different behavior at high energy, they both agree with available scattering data up to 350 MeV as discussed in Sections 1.3 and 1.4. The HRP decouples the high-momentum modes, such that the resulting low-momentum interaction is nearly identical regardless of the initial microscopic NN potential. Fig. 2.4 is an application of the results shown in Fig. 17 of [31], which displays identical low-momentum interactions when v_{lowk} is applied to various phenomenological NN potentials. Therefore, the choice of intial potential will not affect the results in this work. The N3LO potential is preferred due to its connection to the underlying theory of QCD and its expansion based on power counting in χEFT.

2.4 Dependence on RG method

The next ingredient of interest is the renormalization group method of choice. The HRP was performed identically to Section 2.2, except with the G-matrix technique as the RG method. Fig. 2.5 shows the comparison of all TBME for this new interaction and the HRP-SD interaction. Again, the TBME lie along the line of equality with small deviation. While there is more deviation than Fig. 2.4, the agreement is still sufficient to assume that both RG methods accurately decouple the high-momentum modes from the low-momentum modes, such that the low-momentum interaction input for many-body perturbative techniques is acceptable. The v_{lowk} renormalization is preferred because the G-matrix technique takes approximately six times longer for the application to the *sd* model space and depends on a somewhat arbitrary starting energy.

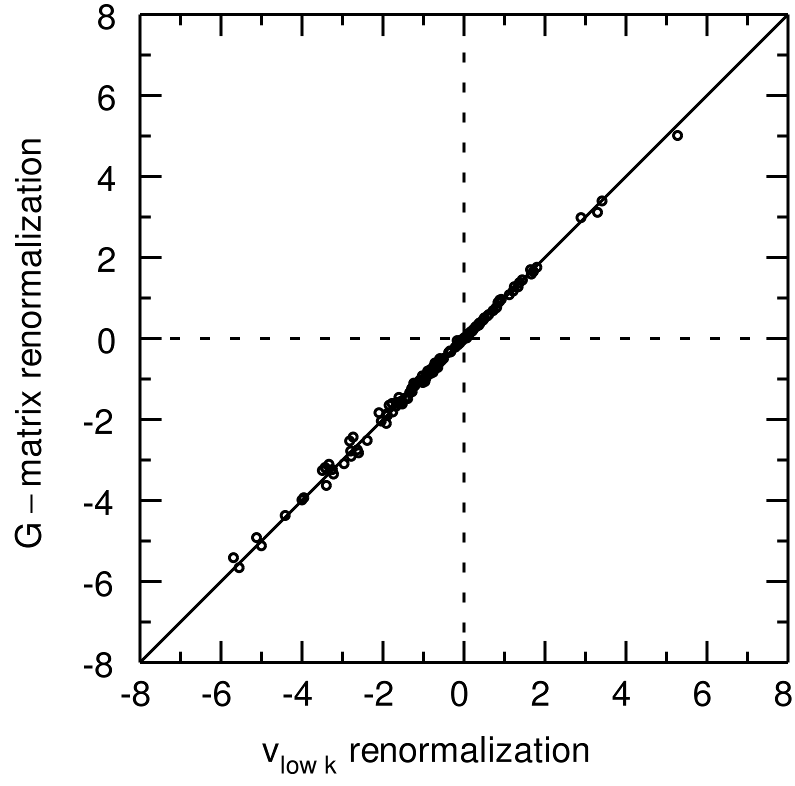

Figure 2.5: Two-body matrix elements for the v_{lowk} renormalization group method (x-axis) and for the G-matrix RG method (y-axis) in an otherwise identical HRP.

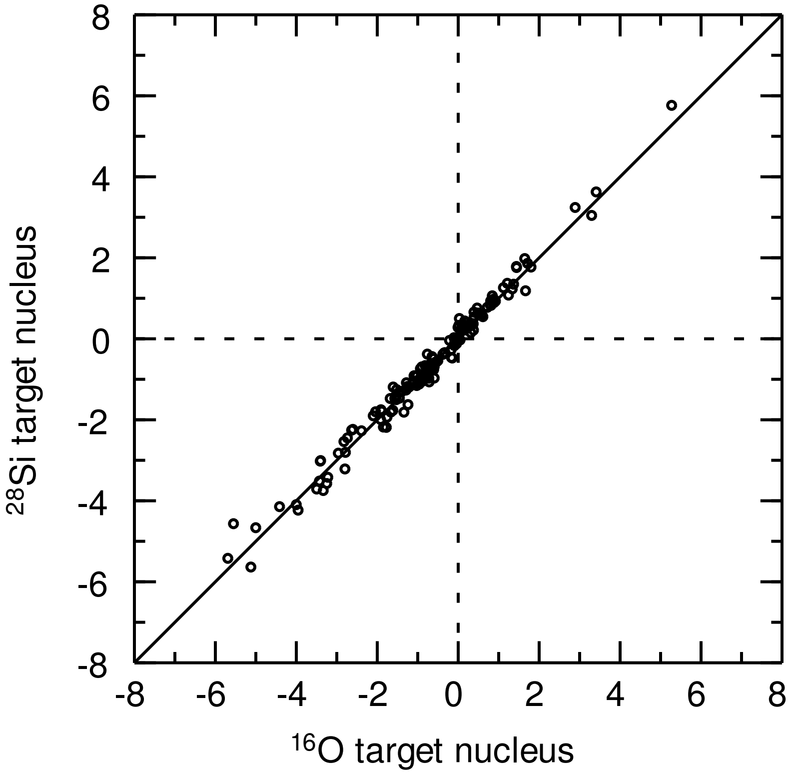

Figure 2.6: Two-body matrix elements when the core in an otherwise identical HRP is ^{16}O (x-axis) or ^{28}Si (y-axis).

2.5 Dependence on Target Nucleus

In order to compare the matrix elements, the model spaces must be identical. However, the choice of target nucleus is available for comparison and is important to study since multiple targets are available for each model space. The HRP-SD interaction was developed in a similar way to standard CI techniques, with the target as the vacuum in the CI calculations. If midshell nuclei are of interest, the nearest possible target, fulfilling the closed-subshell requirement, is ^{28}Si. The HRP was performed identically to Section 2.2, except with ^{28}Si as the target nucleus. In this application, the target nucleus is not the same as the vacuum in the CI calculation, which is always ^{16}O in the *sd* shell. Fig. 2.6 shows the comparison of all TBME for this new interaction and the HRP-SD interaction. The deviation from the line of equality is still relatively small, and occurs in both directions. While there is more deviation than in either of the options studied already, it can be traced to the change in the SHF basis for the different nuclei, which is partially due to three-body effects. At the same time, the agreement is still sufficient to choose a target in the middle of the model space, rather than the core, for calculations throughout the *sd* shell. As mentioned previously, the preference for any nucleus of interest is the closest target, in order to account for many-body effects as accurately as possible. It is important to note at this point that the agreement between the interactions derived for these two targets in the *sd* shell occurs because of the similarity in their behavior. Both targets are stable nuclei with similar shell structure. Moving away from stability, shell structure evolves, even changing the magic numbers described in Section 1.1. Results for exotic targets, as well as the study of the effects of the different bases in the HRP, will be discussed in Chapter 3.

2.6 Dependence on Skyrme Interaction

Another aspect of the renormalization to consider is the choice of Skyrme parameterization. As discussed in Section 1.2, two parameterizations of the Skyrme interaction are Skx and Skxtb, with similar values for the parameters listed in Table 1.1. Since the experimental data from the doubly magic ^{16}O nucleus constrained the fits for Skx and Skxtb, and the difference in the two interactions is mainly due to the tensor force, which only has a significant effect on single particle energies away from stability [55], the SPE for ^{16}O are nearly identical. Later applications will deal with exotic nuclei and therefore Skx and Skxtb will present larger deviations, an effect discussed in Chapters 4 and 5. For this application, a comparison to another Skyrme interaction is of interest and is presented in Fig. 2.7. The HRP is followed identically to Section 2.2 except with Sly4 [56] as the Skyrme interaction. Here the deviation follows a trend towards reduction with Sly4 as the Skyrme interaction. The SPE with the Sly4 interaction vary from the Skxtb and Skx values on the order of MeV because

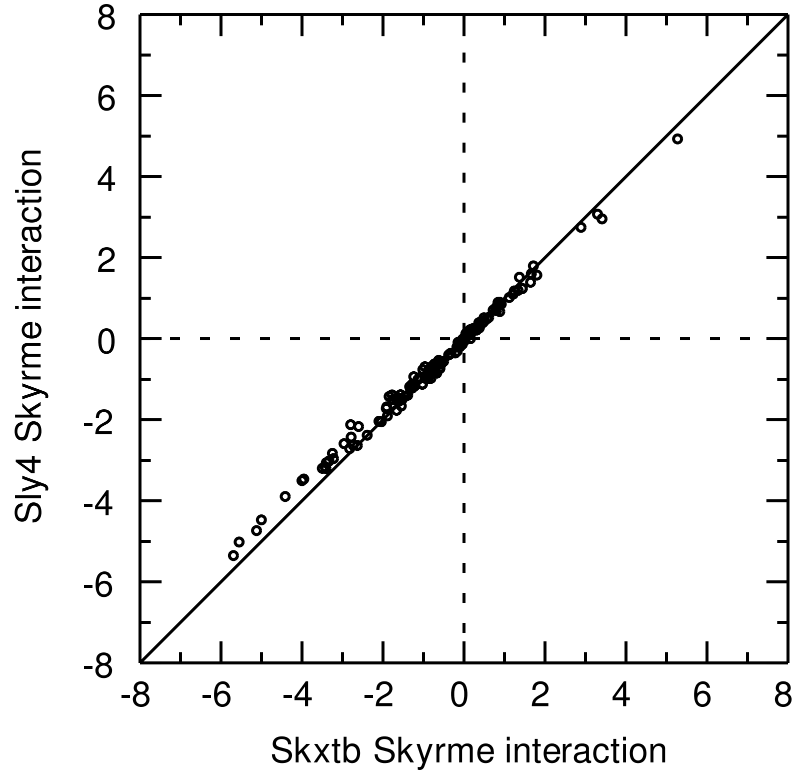

Figure 2.7: Two-body matrix elements when the Skyrme interaction in an otherwise identical HRP is the Skxtb interaction (x-axis) or the Sly4 interaction (y-axis).

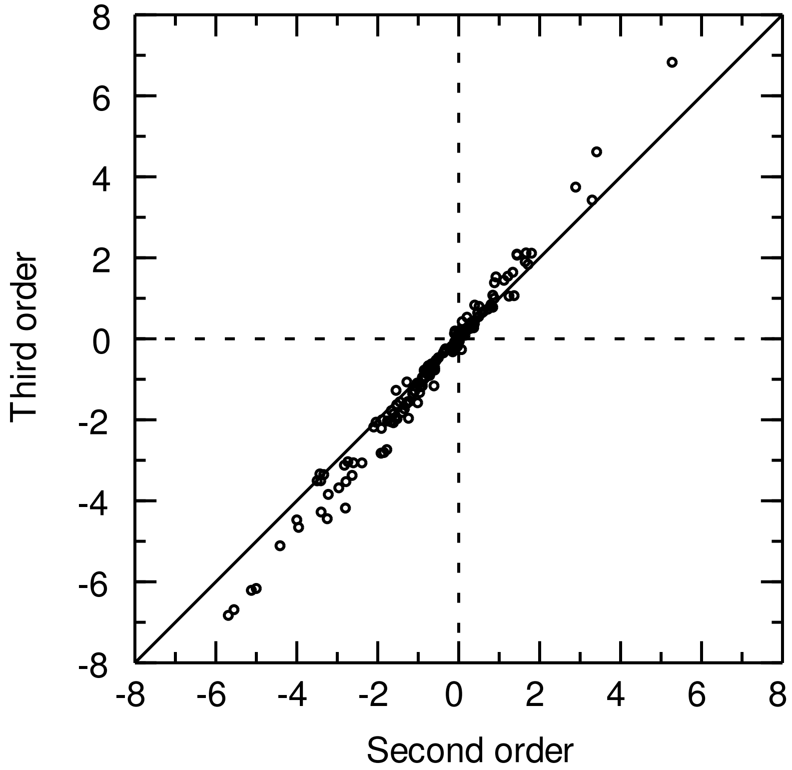

Figure 2.8: Two-body matrix elements to second order (x-axis) or to third order (y-axis) in perturbation theory in an otherwise identical HRP.

the effective mass of the Sly4 interaction is reduced by 20%, which results in a lower single particle density as discussed in Section 4.4. The single particle wavefunctions will also be affected, and these changes in the basis reduce the TBME on the order of 5-10%, as seen in Fig. 2.7. Therefore, the single particle energies and radial wavefunctions as determined from Skyrme parameterizations are an important aspect of the calculation and will be treated in more detail in Chapters 3 and 4.

2.7 Dependence on Order of Perturbation Theory

As analyzed by Hjorth-Jensen et al., and displayed in Figs. 1 and 2 of [57], the renormalization in the HO basis does not converge through third order in perturbation theory, which is as far as the Goldstone diagram representation of Rayleigh-Schrödinger perturbation theory has been derived for applications to nuclear structure. However, the renormalization in a realistic Brueckner-Hartree-Fock basis nearly converges at second order in perturbation theory, even though the results for ^{18}O and ^{18}F are in worse agreement with experiment than the calculations with the HO basis. Their realistic basis neglects many-body forces, so the Hybrid Renormalization Procedure in the SHF basis should produce better results with similar convergence properties. Fig. 2.8 compares the TBME for different orders of perturbation theory. The third order increases the strength of the TBME, such that convergence has not been achieved. The effect of the stronger interaction due to third order diagrams on ^{18}O can be seen from a comparison of Figs. 2.1 and 2.2, which shows that the calculation does not depend strongly on the order of interaction. Second order will be treated as sufficiently converged throughout this work.

2.8 Number of Excitations

To display the concept of excitations, Fig. 2.9 shows the expected ground state configurations of neutrons and protons for the ^{16}O target. Similar plots will be shown later, so the salient features of the figure will be discussed. The target nucleus and Skyrme interaction are displayed at the top of the figure. On the left, the proton single particle orbits as determined from the Skyrme Hartree-Fock calculation are shown, labeled by ℓ_{2j}. Occupied orbitals are marked by dots, with a total occupation of 8 protons shown at the bottom of the figure. The occupation of a particular orbital is given by $(2j+1)$, so each of the $0s_{1/2}, 0p_{3/2}$, and $0p_{1/2}$ orbits is fully occupied. The black box shows model space orbits, in this case the *sd* orbits. In the center of the figure, the same situation is shown for neutrons. For ^{16}O with the Skxtb interaction, the results for neutrons are similar to protons with the energy shifted down by approximately 4 MeV. On the right side of the figure, the results for the harmonic oscillator mean field potential are shown, with $\hbar\omega$ determined by the mass (see Section 1.1). The absolute

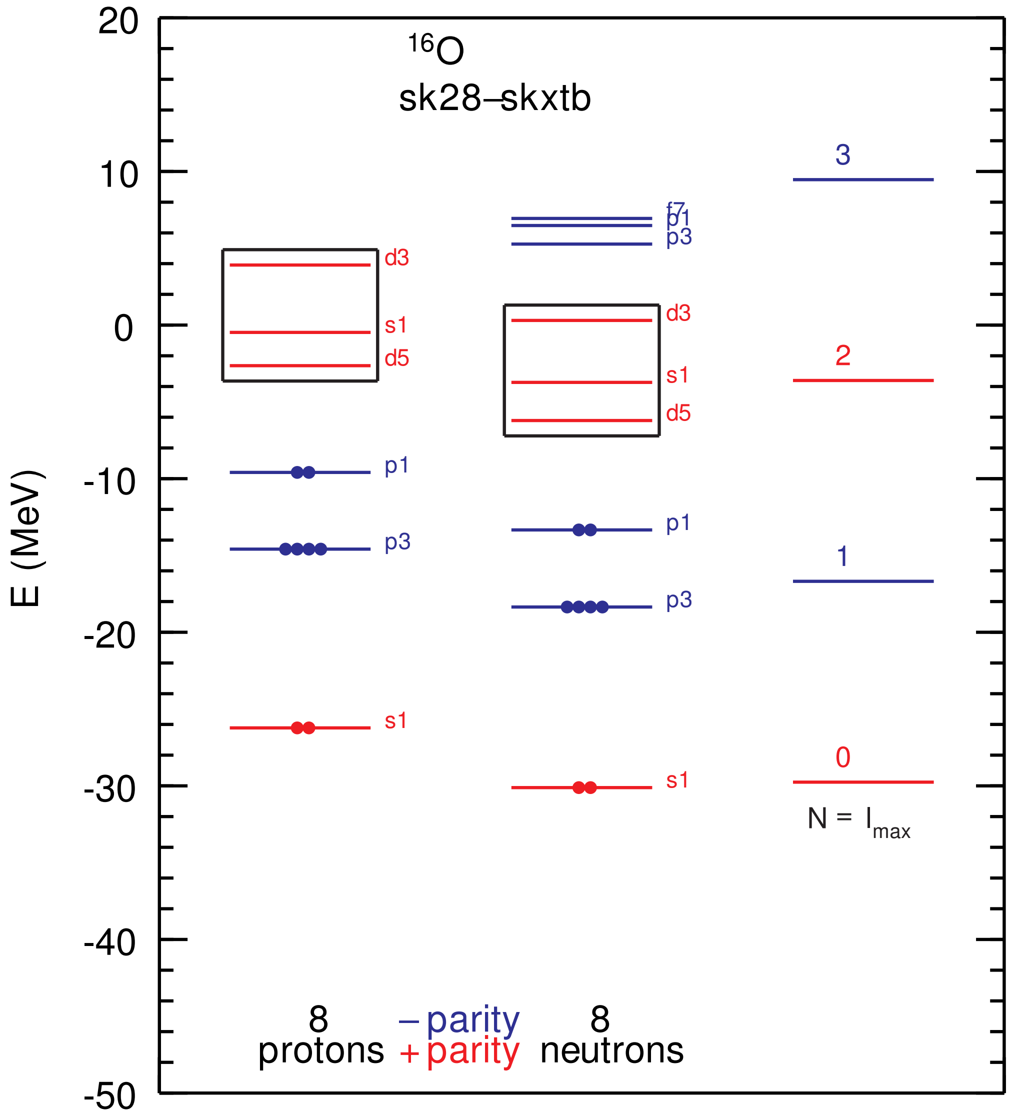

Figure 2.9: Single particle orbits for ^{16}O, as calculated with the Skxtb interaction for protons and neutrons and with a harmonic oscillator potential. Details are included in the text.

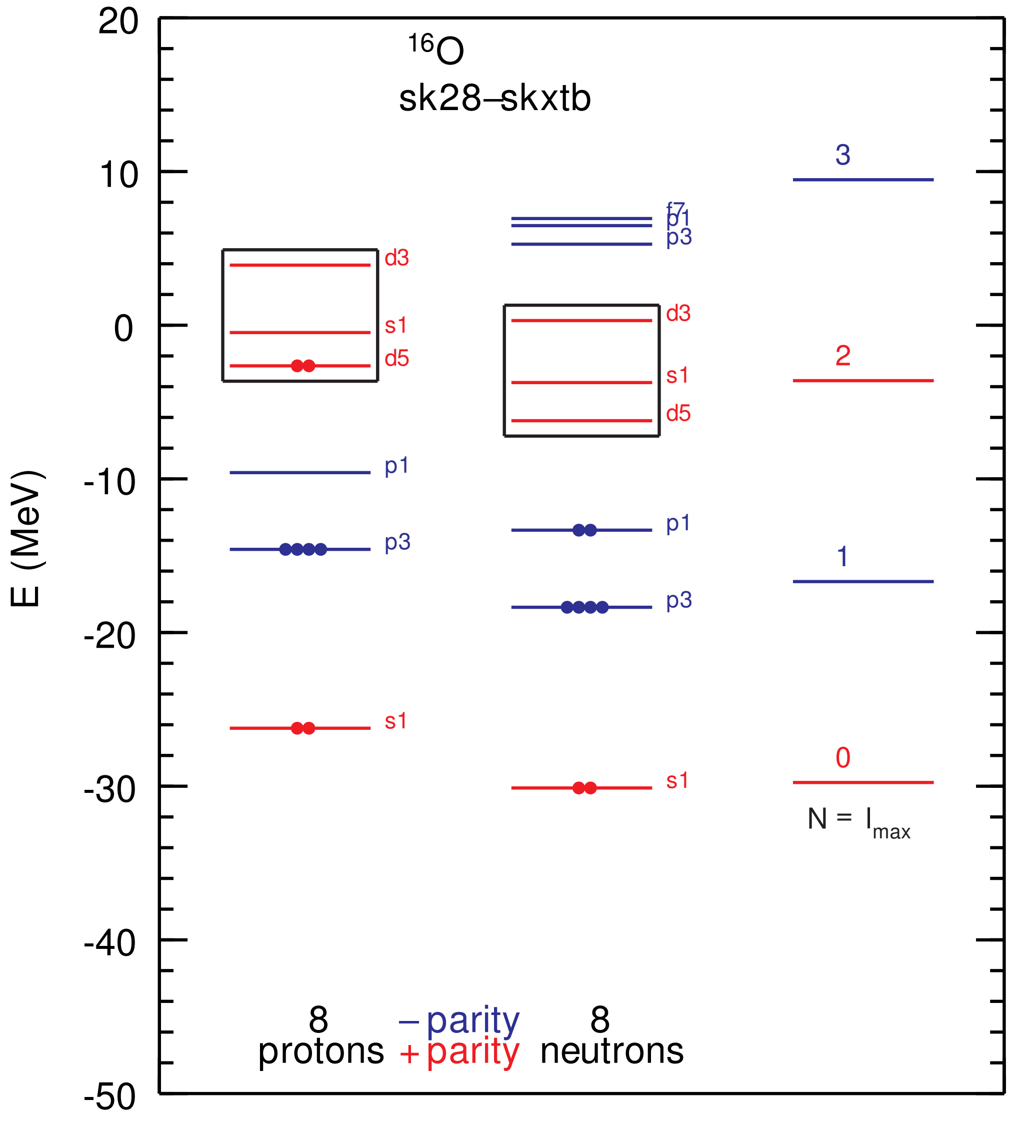

Figure 2.10: A pair of protons are excited one oscillator shell to produce a configuration representing a $2\hbar\omega$ excitation of the Skyrme Hartree-Fock ground state of Fig. 2.9.

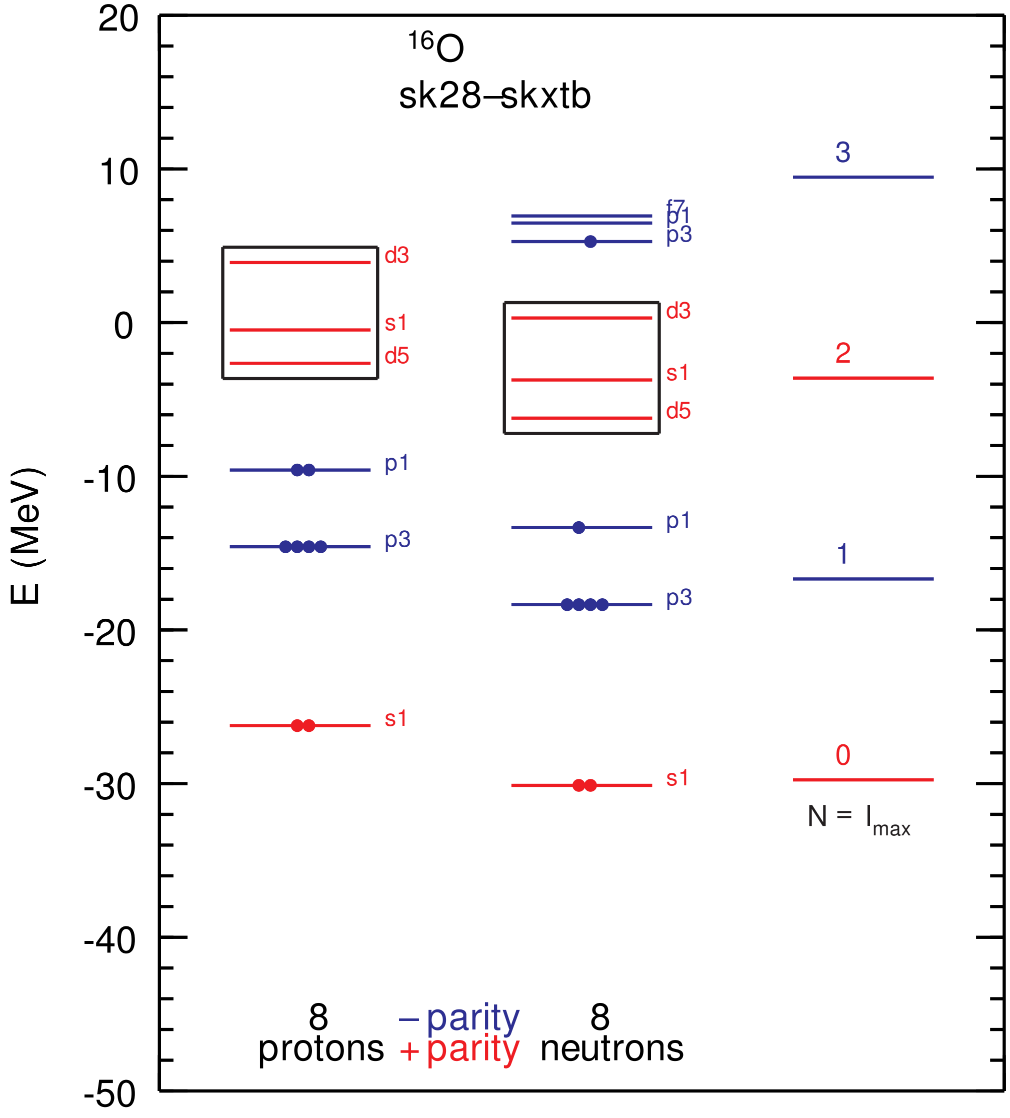

Figure 2.11: In this case, one neutron is excited two oscillator shells to produce a configuration representing a $2\hbar\omega$ excitation of the Skyrme Hartree-Fock ground state of Fig. 2.9.

energy of the harmonic oscillator orbits are chosen to correspond approximately to the Skyrme results. The oscillator shell is listed by the main quantum number N. For all three columns, the positive parity orbits are red and the negative parity orbits are blue.

From Fig. 2.9, which shows the ground state configuration as determined in a mean field calculation with Skyrme Hartree-Fock, excited configurations are produced by promoting either protons or neutrons into higher orbits. An excitation of one nucleon from the $N = 1$ p shell to the $N = 2$ sd shell corresponds to an increase of one $\hbar\omega$ in the total energy of the configuration in the harmonic oscillator potential. Figs. 2.10 and 2.11 display $2\hbar\omega$ configurations where, respectively, two protons are excited into the next oscillator shell and one neutron is promoted into the next oscillator shell of the same parity. A cutoff of $6\hbar\omega$ allows all excitations of protons and neutrons which combine to $6\hbar\omega$ or less, requiring the $N = 8$ oscillator shell in the calculation (from the greatest excitation possible of one model space nucleon).

For the number of excitations, the work of Shurpin et al. [58] shows that a folded diagram procedure in perturbation theory with a self-consistent basis accelerates the convergence of the interaction. Sommermann et al. [59] have shown that core polarization converges rapidly with modern potentials, such that $2\hbar\omega$ excitations are sufficient. Fig. 2.12 displays a comparison of TBME for $4\hbar\omega$ and $6\hbar\omega$ excitations, while Fig. 2.13 compares $6\hbar\omega$ and $8\hbar\omega$ excitations. In each case, the values of the TBME increase when more excitations are included. When the calculation is converged, an increase in the number of excitations will not affect the TBME. Computational restrictions prevent a determination of the number of excitations required for convergence. The inclusion of more excitations will produce stronger interactions, but as will be seen in Section 5.1, an overall normalization parameter will be introduced to account for the approximately linear dependence on the ingredients of the renormalization. In Section 5.1, a reduction in the strength of the interaction is necessary. If enough excitations were included for convergence, a smaller overall normalization factor would be neces-

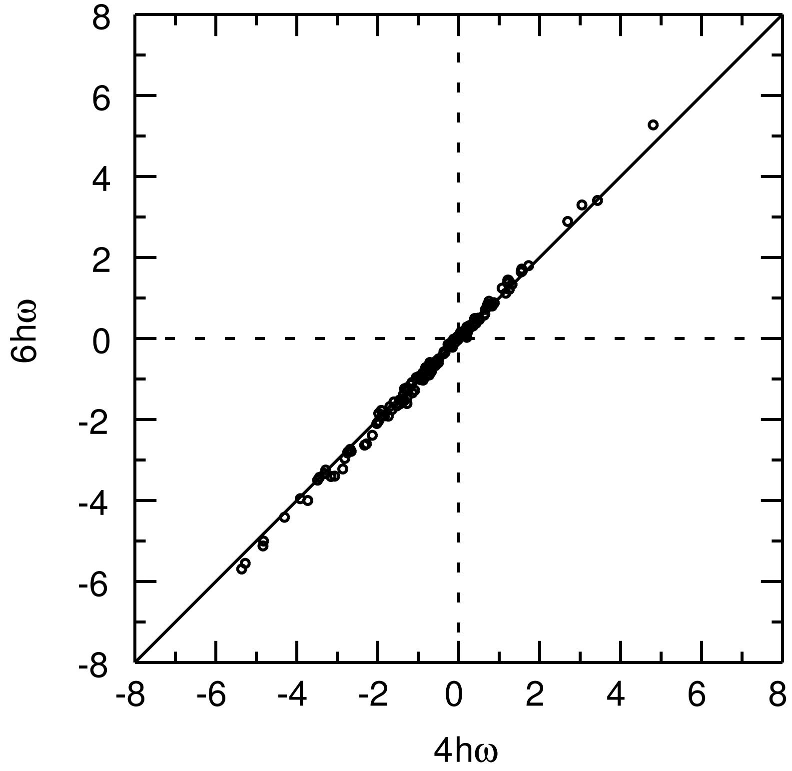

Figure 2.12: Two-body matrix elements including $4\hbar\omega$ (x-axis) or $6\hbar\omega$ (y-axis) excitations in an otherwise identical HRP.

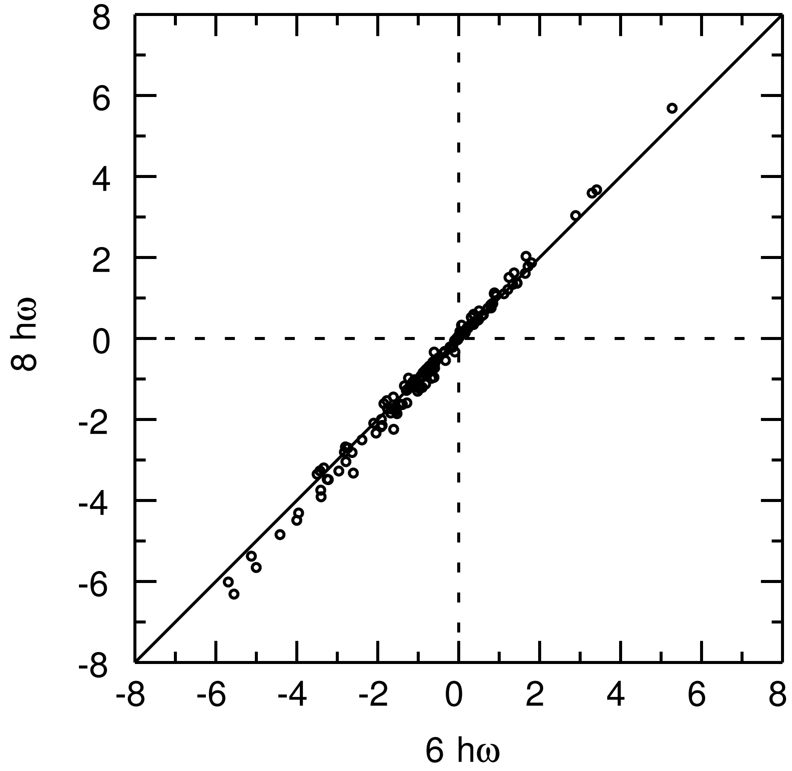

Figure 2.13: Two-body matrix elements including $6\hbar\omega$ (x-axis) or $8\hbar\omega$ (y-axis) excitations in an otherwise identical HRP.

sary. For computational reasons, excitations up to $6\hbar\omega$ will be included throughout this work to produce reasonable results.

2.9 Issues

Regardless of the ingredients of the Hybrid Renormalization Procedure, there are certain anomalies that arise in the procedure that can affect the accuracy of the output two-body matrix elements. In general, the concern relates to divergences in the TBME from calculations of Goldstone diagrams that contain energy denominators equal to or nearly equal to zero. Several situations can lead to divergences, and modifications to avoid these non-physical divergences must be considered. The methods employed in this work are detailed so that the results can be replicated.

The energy denominator for the $2p1h$ diagram in Fig. 1.4 will diverge in the harmonic oscillator basis if the hole line is $2\hbar\omega$ below the model space orbit and each particle line is an $\hbar\omega$ excitation. The procedures to calculate diagrams are detailed in [11] and [38]. For the example in the sd model space, the diagram for the $d_{5/2}$ orbit diverges in the HO basis if the particles are in the pf shell and the hole is in the $0s_{1/2}$ orbit. Even in the non-degenerate SHF basis, energy differences can approach zero, based on nearly constant spin-orbit splitting in different oscillator shells, for example. The folded diagram procedure is designed to overcome these types of divergences.

Derivatives of the $\hat{Q}$-box are evaluated to fifth order. The model space orbits are all set to the same valence energy such that the $\hat{Q}$-box and its derivatives are evaluated at the same energy for all contributing terms. The starting energy ω in each diagram is set at twice the valence energy of the model space, where the valence energy is determined from $\sum_{i=1}^{D}(2j+1)\epsilon_{nlj}$. For convenience, since only energy differences affect the results, a consistent starting energy of -10 MeV is applied in all cases. The proton and neutron single particle spectra, as calculated in either the HO or SHF basis, are shifted independently so that the valence energies are -5 MeV. As discussed in [11], calculating the $\hat{Q}$-box to higher orders should reduce the dependence on starting energies, but it can diverge due to intruder states outside of the model space. These divergences could be avoided with a larger model space, but prohibitively large calculations can result. Third order diagrams depend on the starting energy to a greater degree than second order diagrams. The generation of divergences occurs more readily when perturbative techniques are applied to third order, further supporting the restriction to second order in Rayleigh-Schrödinger perturbation theory throughout this work.

A large model space with orbits in multiple oscillator shells for one type of nucleon will lead to divergences in this approach, since all model space orbits are set to a constant valence energy. For instance, if the p and sd shells were included in a model space with ^{16}O as the target, divergences would result. This can be seen from the particle-particle ladder diagram in Fig. 1.5, for diagrams where p holes in the model space are excited to sd particles in the model space with the same energy. Therefore, when such a model space is necessary, the model space orbits will be placed in a common oscillator shell. The choice of shell can be determined on a case-by-case basis. This issue will only arise in Section 5.1 of this work and the specific treatment will be discussed there.

In addition to the issues already discussed, the choice of v_{lowk} as the renormalization group method requires additional parameters that have not yet been discussed. Four parameters enter the calculation, as seen from the definition of the v_{lowk} procedure in Section 1.4. First, a cutoff Λ must be chosen. Second, a limit to the integration must be implemented, since the non-analytic integral cannot be solved from 0 to ∞. Finally, the integrations, from zero momentum to the cutoff momentum and from the cutoff momentum to the integration limit, must be performed on a mesh in momentum space. Therefore, a specific number of mesh points is chosen for each integration. The cutoff should be $\Lambda \approx 2$ fm^{-1}, as motivated in Section 1.4. The integration limit is set to 20 fm^{-1}, which is more than sufficient to account for the low-energy behavior

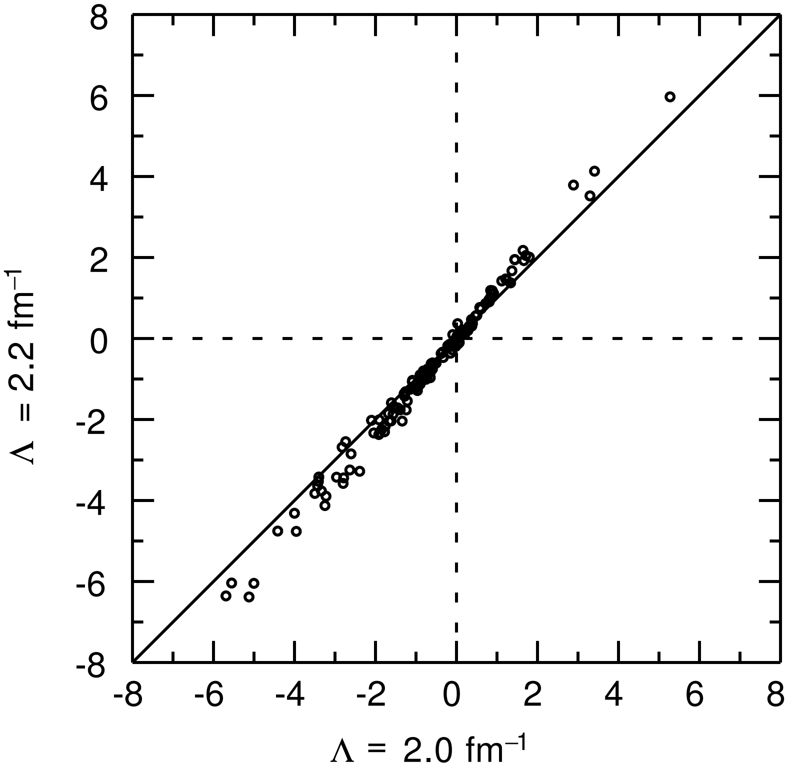

Figure 2.14: Comparison of the two-body matrix elements for a cutoff momentum of $\Lambda = 2.0$ fm^{-1} (x-axis) or $\Lambda = 2.2$ fm^{-1} (y-axis) in an otherwise identical HRP.

of the microscopic NN potentials fit to 350 MeV. Sixty integration points are utilized for both integrations. This produces a fine mesh at low-momentum (low-energy) and a coarse mesh above the cutoff momentum. The TBME have been found to depend on the number of integration points and the integration limit at the order of 10 eV. In other words, the choices of these parameters do not affect the TBME, which are sufficiently converged to the order necessary for calculations at the keV level. However, the cutoff does affect the results. Fig. 2.14 displays a comparison between the HRP-SD interaction, where $\Lambda = 2.0$ fm^{-1}, and a new interaction which follows the same HRP as Section 2.2 but employs a cutoff $\Lambda = 2.2$ fm^{-1}. The trend shows a reduction in strength of the TBME as the cutoff is lowered, with significant deviation from the line of equality. The cutoff dependence is related to the truncation of "induced" many-body forces [31], which contribute on the order of 15%. These induced many-body forces are independent of the explicit three-body forces not taken into account with a procedure based on the renormalization of a microscopic NN potential. See Fig. 35 of [31] for an example of the size of the various contributions as a function of the cutoff. The cutoff dependence provides an estimate of a theoretical uncertainty from the v_{lowk} renormalization, but will not be studied in detail.

2.10 Standard Implementation

At this point, all ingredients of the Hybrid Renormalization Procedure have been evaluated except for the choice of basis, which will be covered in detail in the next chapter. A standard approach can be established for future implementations of the HRP. In the standard implementation, the N3LO interaction will be converted to a low-momentum interaction using v_{lowk} with a sharp cutoff of $\Lambda = 2.0$ fm^{-1}, and will then be renormalized with Rayleigh-Schrödinger perturbation theory to second order and $6\hbar\omega$ with a realistic basis derived from the Skxtb interaction. In order to prevent divergences, a common valence energy is applied to all model space orbits, equal to half the starting energy of -10 MeV. When orbits of both positive and negative parity are included in the model space for either protons or neutrons, all valence orbits of that type of nucleon will be placed into a single oscillator shell.

Unless otherwise stated, the standard implementation will be assumed when discussing or referring to the HRP throughout the remainder of this work.

Chapter 3

Comparison of Bases

New facilities for rare isotope beams will push the experimental capabilities of nuclear physics with radioactive beams to more unstable, shorter-lived nuclei. Properties of these nuclei exhibiting different behavior than stable nuclei, like the evolution of shell structure, are of significant interest for the next decades of research. The production of model space interactions can be compared in stable and exotic regions of the nuclear chart to examine the importance of refining theoretical approaches for unstable nuclei.

In the past, the conversion of a realistic NN interaction into an interaction in the nuclear medium has typically employed renormalization methods in the harmonic oscillator basis for a doubly magic core. For more exotic closed-subshell nuclei, loosely bound orbits often play a role. Loosely bound orbits particularly deviate from the oscillator basis, by exhibiting a “long-tail” behavior with extended radial wavefunctions. The harmonic oscillator basis is therefore less applicable further from stability. However, few calculations have been done with a realistic radial basis for unstable nuclei with renormalized NN interactions.

Experimental interest in neutron-rich silicon isotopes and the failure of some shell model Hamiltonians to reproduce data in the region have led to modifications in the SDPF-NR interaction [47], which had been the standard for shell model calculations in the *sdpf* model space. The new SDPF-U interaction [48] has different neutron-

neutron pairing matrix elements for $Z \geq 15$ and $Z \leq 14$ to account for the behavior of pf neutron orbits relative to the number of valence protons, as discussed in Section 1.7. The $Z \leq 14$ version of the interaction treats neutron-rich unstable nuclei that exhibit different shell behavior than the less exotic nuclei in the $Z \geq 15$ nuclei. The interest in silicon isotopes and the nature of the SDPF-U interaction make ^{34}Si a suitable choice for the renormalization procedure with a realistic basis. A similar effect occurs for the neutron-rich carbon isotopes around the $N = 14$ closed subshell, requiring a 25% reduction in the neutron-neutron two-body matrix elements from the effective interactions derived for the oxygen isotopes [60].

3.1 Application to $sdpf$ model space

A deeper understanding of the need for multiple interactions in the $sdpf$ model space, as seen by the form of SDPF-U, can be gained by performing the renormalization for the same model space in multiple ways. The active orbits in the $sdpf$ model space are the sd proton orbits and pf neutron orbits. The Hybrid Renormalization Procedure is followed for two different target nuclei in all three bases, producing a total of six interactions. The two target nuclei are the stable ^{40}Ca doubly magic nucleus and the neutron-rich ^{34}Si semi-magic nucleus. Figs. 3.1 and 3.2 display the single particle bases for ^{40}Ca and ^{34}Si, respectively. Furthermore, the single particle energies of the SHF basis, using the Skxtb interaction, are presented in Table 3.1 for both target nuclei. For an SHF state that is unbound, the radial wavefunction is approximated by a state artificially bound by 200 keV, obtained by multiplying the SHF central potential by a factor larger than unity. The energy of the unbound state is estimated by taking the expectation value of this bound state wavefunction in the original SHF potential.

In the SHF basis, the calculation of single particle energies shows that the proton orbits are shifted down in energy for ^{34}Si relative to ^{40}Ca, while the neutron orbits

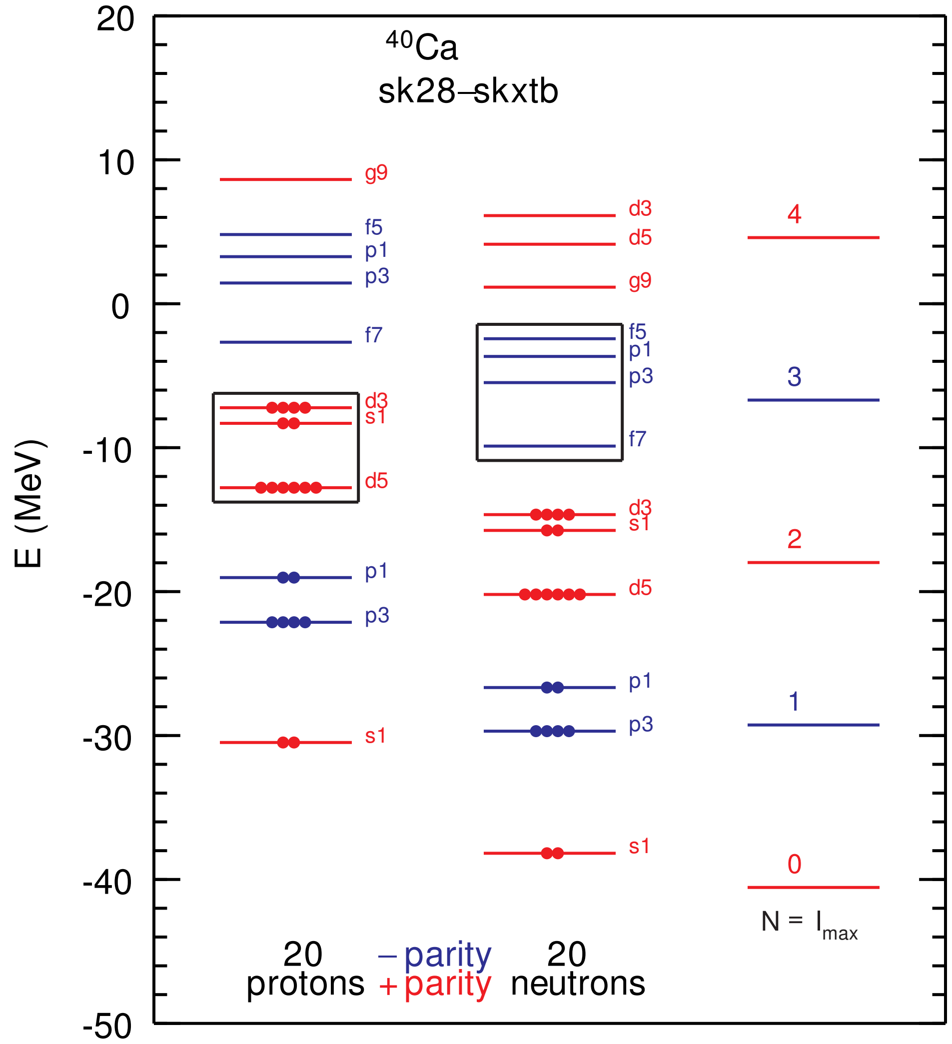

Figure 3.1: Single particle orbits for ^{40}Ca as calculated with the Skxtb interaction. See Fig. 2.9 and discussion in Section 2.8 for details.

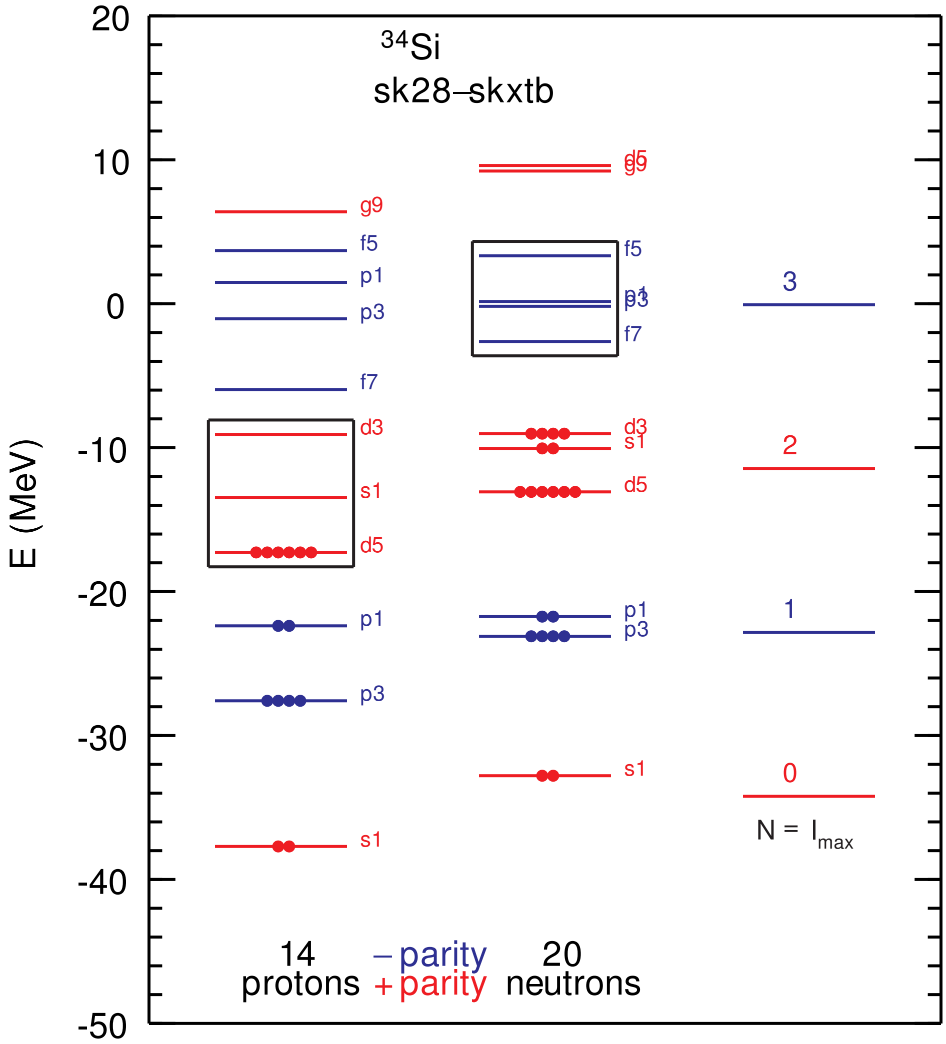

Figure 3.2: Single particle orbits for ^{34}Si as calculated with the Skxtb interaction. See Fig. 2.9 and discussion in Section 2.8 for details.

Table 3.1: Single particle energies from the solution to the Skyrme Hartree-Fock mean field for ^{34}Si and ^{40}Ca using the Skxtb interaction. Values in bold are in the model space.

nℓ_j	^{34}Si proton	^{34}Si neutron	^{40}Ca proton	^{40}Ca neutron
$0s_{1/2}$	-37.73	-32.79	-30.49	-38.18
$0p_{3/2}$	-27.60	-23.10	-22.14	-29.70
$0p_{1/2}$	-22.39	-21.74	-19.03	-26.67
$0d_{5/2}$	**-17.29**	-13.07	**-12.79**	-20.20
$0d_{3/2}$	**-9.08**	-9.03	**-7.23**	-14.65
$1s_{1/2}$	**-13.49**	-10.04	**-8.31**	-15.75
$0f_{7/2}$	-5.97	**-2.62**	-2.68	**-9.89**
$0f_{5/2}$	3.70	**3.33**	4.81	**-2.43**
$1p_{3/2}$	-1.06	**-0.40**	1.44	**-5.48**
$1p_{1/2}$	1.49	**-0.27**	3.27	**-3.66**
$0g_{9/2}$	6.39	9.22	8.63	1.15
$0g_{7/2}$	18.26	18.23	18.76	10.28

Table 3.2: Single particle energies for ^{34}Si and ^{40}Ca in the harmonic oscillator basis. The energy shift is chosen so that the valence energy is identical in both bases. Values in bold are in the model space.

nℓ_j	^{34}Si proton	^{34}Si neutron	^{40}Ca proton	^{40}Ca neutron
$0s_{1/2}$	-36.93	-34.59	-32.22	-39.21
$0p_{3/2}$	-25.42	-23.09	-21.20	-28.19
$0p_{1/2}$	-25.42	-23.09	-21.20	-28.19
$0d_{5/2}$	**-13.91**	-11.58	**-10.18**	-17.17
$0d_{3/2}$	**-13.91**	-11.58	**-10.18**	-17.17
$1s_{1/2}$	**-13.91**	-11.58	**-10.18**	-17.17
$0f_{7/2}$	-2.40	**-0.07**	0.84	**-6.15**
$0f_{5/2}$	-2.40	**-0.07**	0.84	**-6.15**
$1p_{3/2}$	-2.40	**-0.07**	0.84	**-6.15**
$1p_{1/2}$	-2.40	**-0.07**	0.84	**-6.15**
$0g_{9/2}$	9.11	11.44	11.86	4.87
$0g_{7/2}$	9.11	11.44	11.86	4.87

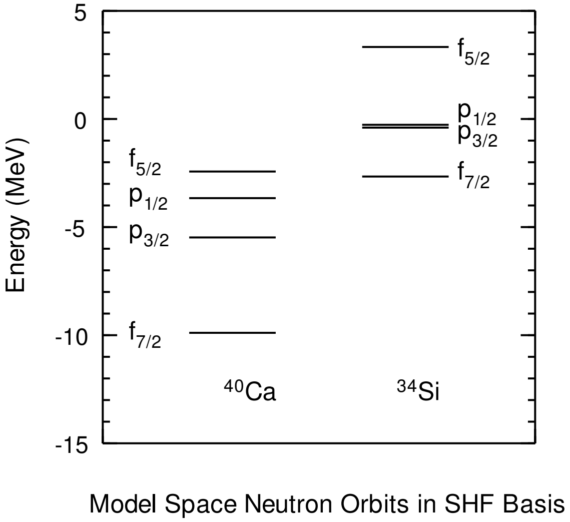

Figure 3.3: Single particle neutron orbits for ^{40}Ca and ^{34}Si as calculated with the Skxtb interaction. The same valence orbits are shifted to higher energy for the exotic, neutron-rich ^{34}Si relative to ^{40}Ca, such that the valence orbit radial wavefunctions are no longer well-described by harmonic oscillator wavefunctions.

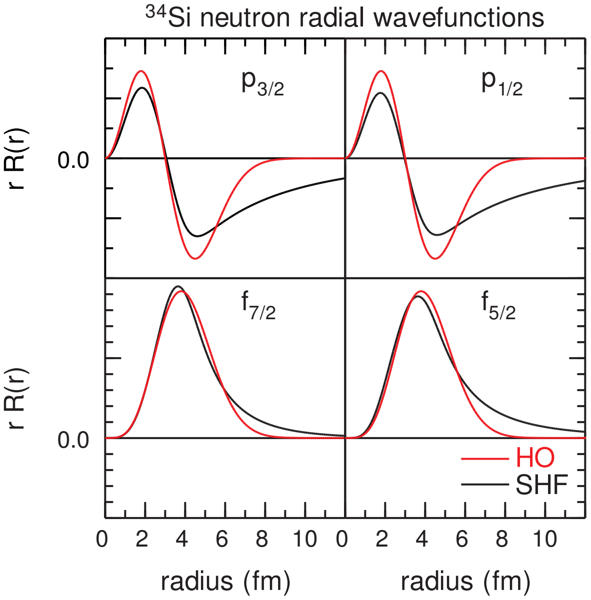

Figure 3.4: Comparison of the single particle radial wavefunctions for ^{34}Si in the HO and SHF bases.

are shifted up. For the valence neutrons, this shift results in a switch from four orbits bound by 5.4 MeV on average for ^{40}Ca to four orbits centered at 0.0 MeV for ^{34}Si. The shift is highlighted in Fig. 3.3, which shows the single particle neutron orbits in the SHF basis for ^{40}Ca and ^{34}Si. This change, specifically the loosely bound energies of the $p_{3/2}$ and $p_{1/2}$ orbits, has a significant effect on the wavefunctions, as seen in Fig. 3.4. The harmonic oscillator radial wavefunctions fall off rapidly at large distances, while the realistic radial wavefunctions exhibit long tail behavior, extending beyond 10 fm. The effects of the shape of the wavefunction will be discussed in more detail later.

For comparison, the single particle energies used in the HO basis are given in Table 3.2. The Blomqvist-Molinari formula [5] $\hbar\omega = (45A^{-1/3} - 25A^{-2/3})$ MeV gives 11.508 MeV for $A = 34$ and 11.021 MeV for $A = 40$. The absolute value of the harmonic oscillator basis is irrelevant, as only energy differences come into the diagrams in Rayleigh-Schrödinger perturbation theory. For a better comparison to the SHF basis, the absolute value is chosen separately for protons and neutrons such that $\sum\limits_{1}^{D}(2j+1)\epsilon_\alpha$ is identical in the HO and SHF bases, where D, the number of valence orbits, is three for protons and four for neutrons and ϵ_α is the energy of the single particle orbit given by the $\alpha = n, l, j$ quantum numbers.

Fig. 3.5 shows a comparison of the pf matrix elements in MeV when the Hybrid Renormalization Procedure is followed for both target nuclei in the HO basis. The $J = 0$ pairing matrix elements are singled out in color due to their importance in ground state properties of even-even nuclei. The TBME in Fig. 3.5 deviate slightly from the line of equality but agree well with each other. Therefore, the choice of target nucleus, whether ^{34}Si or ^{40}Ca, has little effect on the matrix elements in the HO basis. In the explanation of Nowacki and Poves [48], the SDPF-U interaction has different neutron-neutron pairing matrix elements for $Z \geq 15$ and for $Z \leq 14$ to account for $2p2h$ excitations of the core correctly, depending on whether ^{34}Si or ^{40}Ca should be considered the core. The SDPF-U neutron-neutron pairing matrix

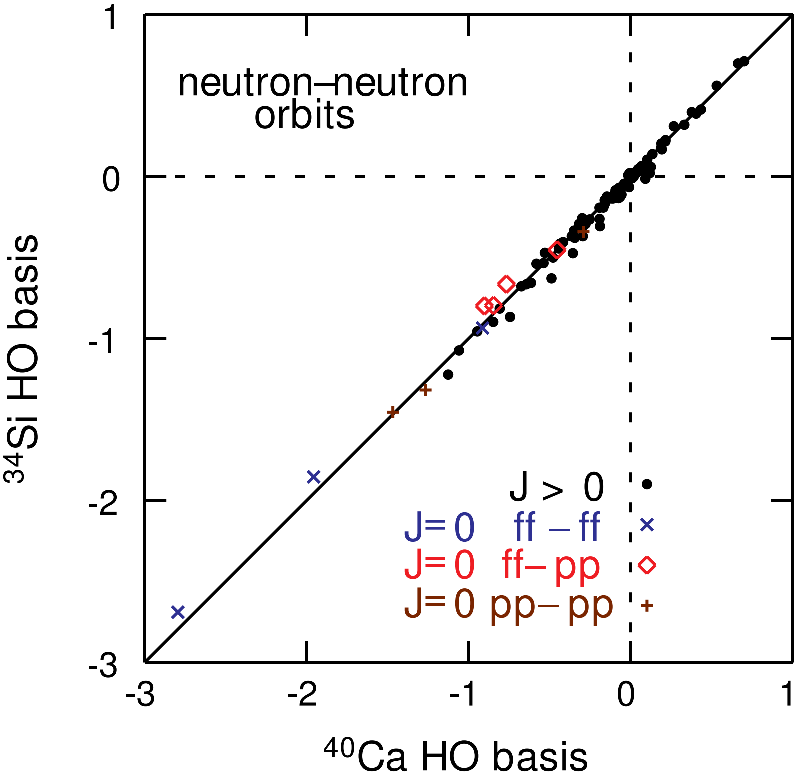

Figure 3.5: Comparison of pf neutron-neutron matrix elements (in MeV) for the renormalization procedure in the HO basis for the two target nuclei. Black dots correspond to matrix elements with $J > 0$, while the $J = 0$ matrix elements are split into three groups: $ff - ff$ (crosses), $ff - pp$ (diamonds), and $pp - pp$ (plus signs). The solid line $y = x$ denotes where the matrix elements would be identical.

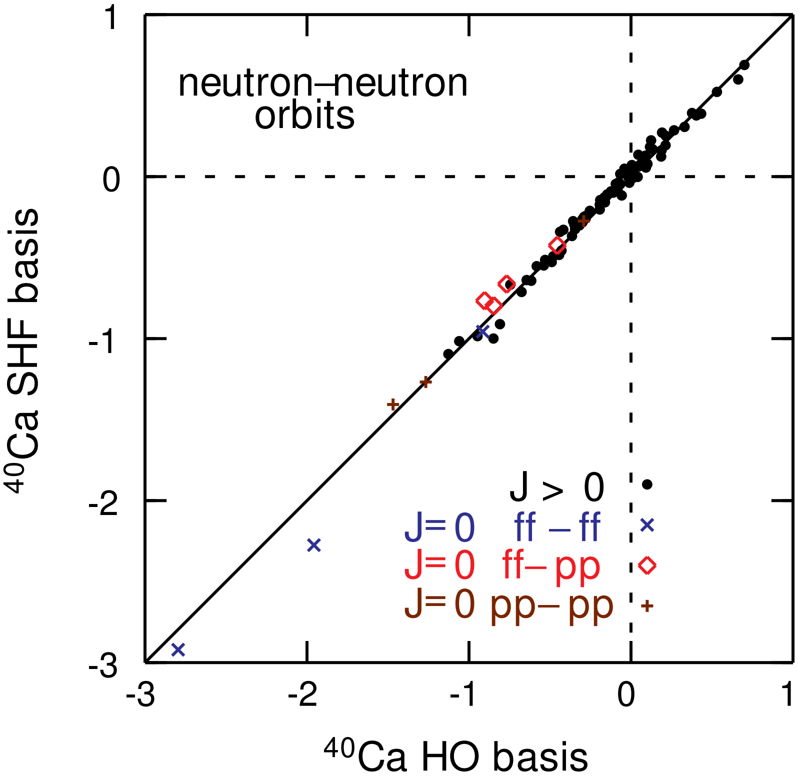

Figure 3.6: Comparison of pf neutron-neutron matrix elements (in MeV) for the renormalization procedure for ^{40}Ca in the HO and SHF bases. Black dots correspond to matrix elements with $J > 0$, while the $J = 0$ matrix elements are split into three groups: $ff - ff$ (crosses), $ff - pp$ (diamonds), and $pp - pp$ (plus signs). The solid line $y = x$ denotes where the matrix elements would be identical.

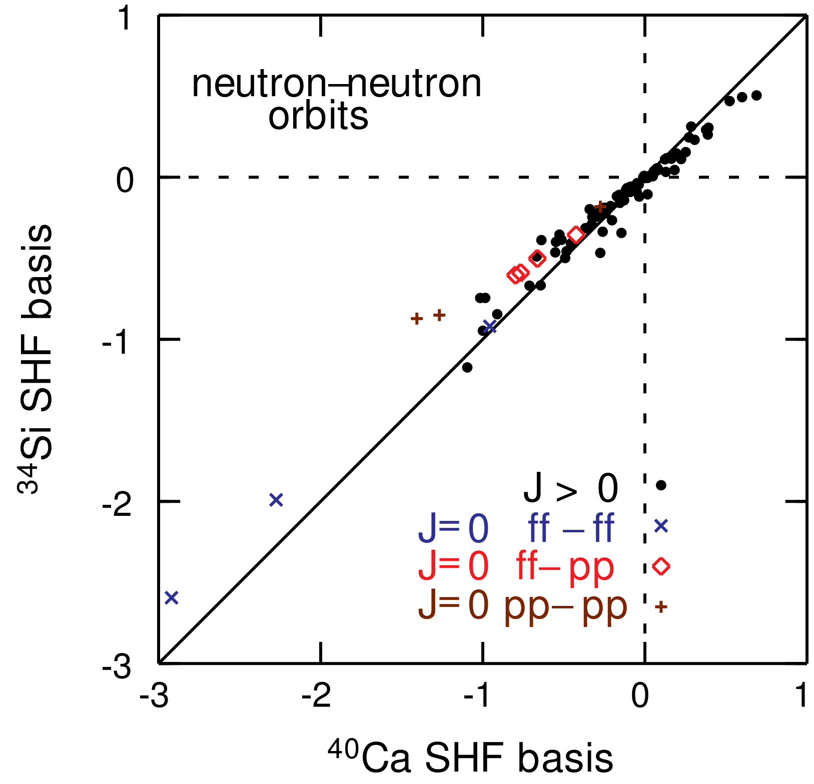

Figure 3.7: Comparison of pf neutron-neutron matrix elements (in MeV) for the renormalization procedure in the SHF basis for the two target nuclei. Black dots correspond to matrix elements with $J > 0$, while the $J = 0$ matrix elements are split into three groups: $ff - ff$ (crosses), $ff - pp$ (diamonds), and $pp - pp$ (plus signs). The solid line $y = x$ denotes where the matrix elements would be identical.

elements are reduced by 300 keV for $Z \leq 14$ in order to produce results in better agreement with experimental data. However, the change in target in the Hybrid Renormalization Procedure mimics the change in core for the SDPF-U interaction, and yet the TBME do not show a reduction in the HO basis. While the occupation of proton orbits has changed, the neutron-neutron pairing matrix elements are not affected. Diagrams involving excitation of protons are unlinked, and are not included in Rayleigh-Schrödinger perturbation theory. Still, the reduction in pairing matrix elements is empirically necessary and should result from a microscopic treatment of the interaction.

For the stable ^{40}Ca target, where the valence orbits are all bound by multiple MeV, the HO basis reproduces the realistic nucleus well as expected from the discussion in Section 1.1. The results in Fig. 3.6 are consistent for ^{40}Ca regardless of the choice of basis. However, in Fig. 3.7, where the comparison is for both target nuclei in the SHF basis, a reduction in the strength of the interaction for ^{34}Si is observed. This reduction with ^{34}Si as the target nucleus is due to the weakly bound nature of the pf neutron orbits.

In the SHF basis, the $f_{7/2}$ orbit is bound by 2.6 MeV, and its radial wavefunction agrees reasonably well with the harmonic oscillator wavefunction as seen in Fig. 3.4. The Skyrme wavefunction is expanded in the harmonic oscillator basis up to $n = n_{max}$ and the a_n coefficients are renormalized to ensure that $\sum_{n=0}^{n_{max}} a_n^2 = 1$. For the Hybrid Renormalization Procedure, orbits up to $(2n + l) = 9$ are included, which gives $n_{max} = 3$ for the $f_{7/2}$ and $f_{5/2}$ orbits and $n_{max} = 4$ for the $p_{3/2}$ and $p_{1/2}$ orbits. These values include over 99% of the strength for the f orbits, but only 93% and 92% for the $p_{3/2}$ and $p_{1/2}$ orbits respectively. A first order calculation can be done to $n_{max} = 6$ for all orbits, which gives 100%, 98%, and 97% for the f, $p_{3/2}$, and $p_{1/2}$ expansions respectively.

With this procedure, 99% of the $f_{7/2}$ orbit is represented by the R_{03}^{HO} wavefunction, but the 1% represented by R_{23}^{HO} and R_{33}^{HO} has a significant effect at large radii. The $p_{3/2}$ and $p_{1/2}$ orbits are only bound by 400 and 269 keV, respectively. The expected harmonic oscillator component R_{11}^{HO} only makes up 80% and 78% of the respective radial wavefunctions. Higher n orbits which extend farther away from the center of the nucleus contribute the remaining strength. The $f_{5/2}$ orbit is unbound by three MeV, but the solution for the Skyrme radial wavefunction is determined by assuming that the orbit is bound by 200 keV. With this method, 97% of the realistic radial wavefunction is given by the R_{03}^{HO} wavefunction. Single particle radial wavefunctions of valence space neutron orbits, shown in Fig. 3.4 in both the HO and SHF basis, enter directly in the evaluation of TBME. The long tail behavior of the realistic basis is evident, as the wavefunctions have significant strength beyond 8 fm unlike the oscillator wavefunctions, especially for the loosely bound p orbits.

The $J = 0$ matrix elements in Fig. 3.7 deviate more from the line of equality, i.e. the pairing matrix elements are most reduced for ^{34}Si when the N3LO interaction is renormalized in the SHF basis. The pairing matrix elements in Fig. 3.7 are reduced for the ^{34}Si target by 214 keV on average, relative to the case with ^{40}Ca as the target, in comparison to the 300 keV reduction of the SDPF-U interaction. The reduction of 214 keV is due solely to the change in occupation of the $d_{5/2}$ proton orbit, as the target nucleus is the only change in the HRP for the two interactions in Fig. 3.7. However, the change in occupation affects not only the single particle energies and radial wavefunctions, but also the available orbits in second-order diagrams. The change in single particle radial wavefunctions plays the most significant role, as suggested by Figs. 3.5 and 3.7, but the contribution of each effect can be analyzed.

Table 3.3 isolates a few matrix elements and compares the total matrix elements and their various components for both target nuclei in all three bases. Three diagrams contribute at second order, denoted as core polarization, particle-particle ladder, and four-particle two-hole, shown diagrammatically in Fig. 1.5. The total matrix element is not a simple summation of the first and second order diagrams, as the folded diagram procedure tends to reduce the matrix element via the blocking of orbitals

Table 3.3: First order, particle-particle ladder, core polarization, four-particle two-hole, and total matrix elements in MeV of the form $\langle aa|V|bb\rangle_{J=0}$ for different renormalization procedures.

			^{34}Si			^{40}Ca		
a	b		HO	MIX	SHF	HO	MIX	SHF
$f_{7/2}$	$f_{7/2}$	first	-0.906	-0.906	-0.807	-0.938	-0.938	-0.870
		2p-ladder	-0.409	-0.414	-0.422	-0.409	-0.418	-0.450
		core pol.	-0.449	-0.377	-0.417	-0.637	-0.649	-0.768
		4p2h	-0.376	-0.442	-0.435	-0.374	-0.434	-0.499
		total	-1.855	-1.869	-1.824	-1.957	-1.982	-2.084
$f_{7/2}$	$p_{3/2}$	first	-0.518	-0.518	-0.322	-0.518	-0.518	-0.368
		2p-ladder	-0.148	-0.157	-0.119	-0.152	-0.164	-0.138
		core pol.	-0.121	-0.118	-0.074	-0.282	-0.309	-0.283
		4p2h	-0.123	-0.141	-0.104	-0.126	-0.142	-0.143
		total	-0.800	-0.822	-0.552	-0.903	-0.926	-0.749
$f_{7/2}$	$p_{1/2}$	first	-0.585	-0.585	-0.421	-0.572	-0.572	-0.452
		2p-ladder	-0.042	-0.050	-0.039	-0.049	-0.062	-0.038
		core pol.	-0.055	-0.041	-0.043	-0.212	-0.236	-0.231
		4p2h	-0.057	-0.058	-0.037	-0.062	-0.060	-0.052
		total	-0.665	-0.663	-0.492	-0.767	-0.779	-0.642
$p_{3/2}$	$p_{3/2}$	first	-1.109	-1.109	-0.776	-1.096	-1.096	-1.082
		2p-ladder	-0.233	-0.242	-0.165	-0.233	-0.237	-0.242
		core pol.	-0.037	0.001	0.000	-0.021	-0.005	-0.037
		4p2h	-0.085	-0.093	-0.057	-0.090	-0.098	-0.109
		total	-1.319	-1.313	-0.931	-1.267	-1.252	-1.278
$p_{3/2}$	$p_{1/2}$	first	-1.540	-1.540	-0.857	-1.478	-1.478	-1.382
		2p-ladder	-0.060	-0.069	-0.078	-0.068	-0.081	-0.077
		core pol.	0.068	0.082	0.045	-0.038	-0.069	-0.080
		4p2h	-0.048	-0.051	-0.026	-0.053	-0.054	-0.056
		total	-1.456	-1.462	-0.863	-1.469	-1.488	-1.409

[11]. The reduction for total matrix elements involving p orbits in the SHF basis with ^{34}Si as the core is dramatic ($\approx 30\%$) and is primarily due to the extension of wavefunction strength to large distances. Kuo et al. [61] noted a reduction of core polarization in the harmonic oscillator basis and used different oscillator parameters to account for the core nucleons and valence nucleons separately in halo nuclei. While ^{34}Si is not a halo nucleus, the loosely bound p orbits behave in much the same way as the valence nucleons in a halo nucleus. The reduction in core polarization is seen going from the ^{40}Ca target to the ^{34}Si target in any basis in Table 3.3, although the size of the polarization is reduced for nucleons far from the core. As noted in [61], the core interacts less with nucleons far away, so the excitations of the core are reduced. The core polarization for matrix elements solely involving p orbits is under 100 keV. Nowacki and Poves [48] attributed the reduction in neutron-neutron pairing matrix elements for the empirical SDPF-U interaction to a decrease in core polarization for the ^{34}Si target. Table 3.3 shows that the core polarization can be reduced significantly without a proportional reduction in the total matrix element. For instance, the $\langle f_{7/2}f_{7/2}|V|f_{7/2}f_{7/2}\rangle$ matrix element is only reduced by 5% from ^{40}Ca to ^{34}Si in the HO basis even though the core polarization is reduced by 30%. In the SHF basis, which takes into account the realistic wavefunction, the total matrix element is reduced by 13% while the core polarization is reduced by 46%. For this matrix element, the reduction due to core polarization is 188 and 351 keV in the HO and SHF basis, while the first order reduction due only to the change in wavefunction is 32 and 63 keV. For the $\langle p_{3/2}p_{3/2}|V|p_{3/2}p_{3/2}\rangle$ matrix element, and other TBME involving only loosely bound p orbits, the core polarization becomes very small, skewing percentage comparisons. However, the reduction in core polarization is negligible relative to the wavefunction contribution of 306 keV in the first order diagram for the SHF basis. There is no reduction for the first order diagram in the HO basis. Ogawa et al. [62] produce seemingly consistent results, identifying a 10%-30% reduction in nuclear interaction matrix elements involving loosely bound orbits using

a realistic Woods-Saxon basis. However, they were limited to comparisons of ratios of matrix elements and did not include core polarization. Core polarization suppression and reduction due to spread of the wavefunctions are both important effects which should be included, as well as the other diagrams which contribute at second order. The full treatment of the renormalization in a realistic basis, as developed here, is necessary for accurate results. With the improvements based on the HRP, calculations for neutron-rich silicon isotopes can be performed directly.

3.2 Calculations for ^{36}Si and ^{38}Si

The effect of the different interactions on nuclear structure calculations can be evaluated as neutrons are added to ^{34}Si. In order to obtain a consistent starting point, the proton-proton and proton-neutron matrix elements of SDPF-U have been used, with proton SPE that reproduce those obtained by SDPF-U. Because SDPF-U overbinds ^{35}Si, the SDPF-U neutron SPE have been increased by 660 keV. The six interactions use neutron SPE that reproduce the values of this modified SDPF-U interaction.

The only difference in the six interactions used in the calculations are the neutron-neutron matrix elements. Calculations have been done in the *sdpf* model space with the shell model code NUSHELLX [9]. Fig. 3.8 shows the lowest $J = 0, 2, 4, 6$ states in ^{36}Si, relative to ^{34}Si. The HO basis and the MIX basis deviate by no more than 20 keV for the same target nucleus. However, the SHF basis noticeably shifts the states, with the largest effect being 300 keV less binding in the ground state with ^{34}Si as the target nucleus. The binding energy of ^{36}Si changes by nearly 500 keV depending on which renormalization procedure is used. Furthermore, the level schemes for ^{36}Si are more spread out for the crosses where ^{40}Ca is chosen as the target nucleus.

Fig. 3.9 shows the same states in ^{36}Si relative to ^{34}Si, but now the comparison includes the SDPF-U calculations and experimental data. The MIX basis results are not included since they are so similar to the HO basis calculations. The level

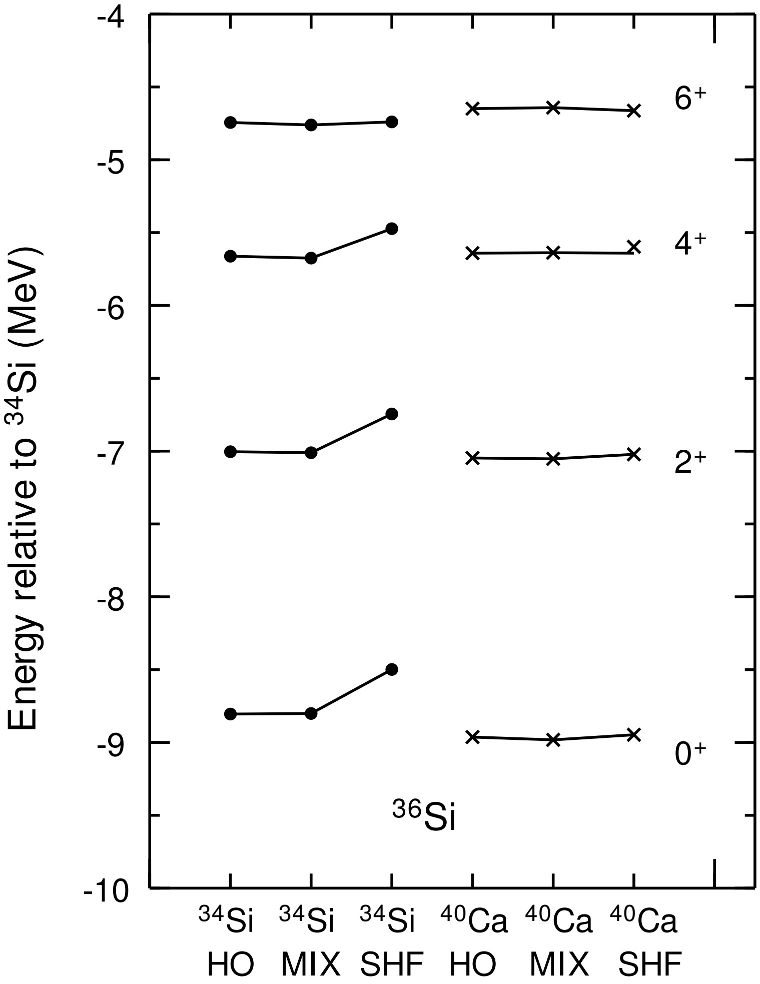

Figure 3.8: Calculations of the lowest-energy states for $J = 0, 2, 4, 6$ in ^{36}Si relative to ^{34}Si from the renormalization procedure for ^{34}Si and ^{40}Ca, in the HO, MIX, and SHF bases for both target nuclei. Crosses are used for calculations with ^{40}Ca as the target nucleus.

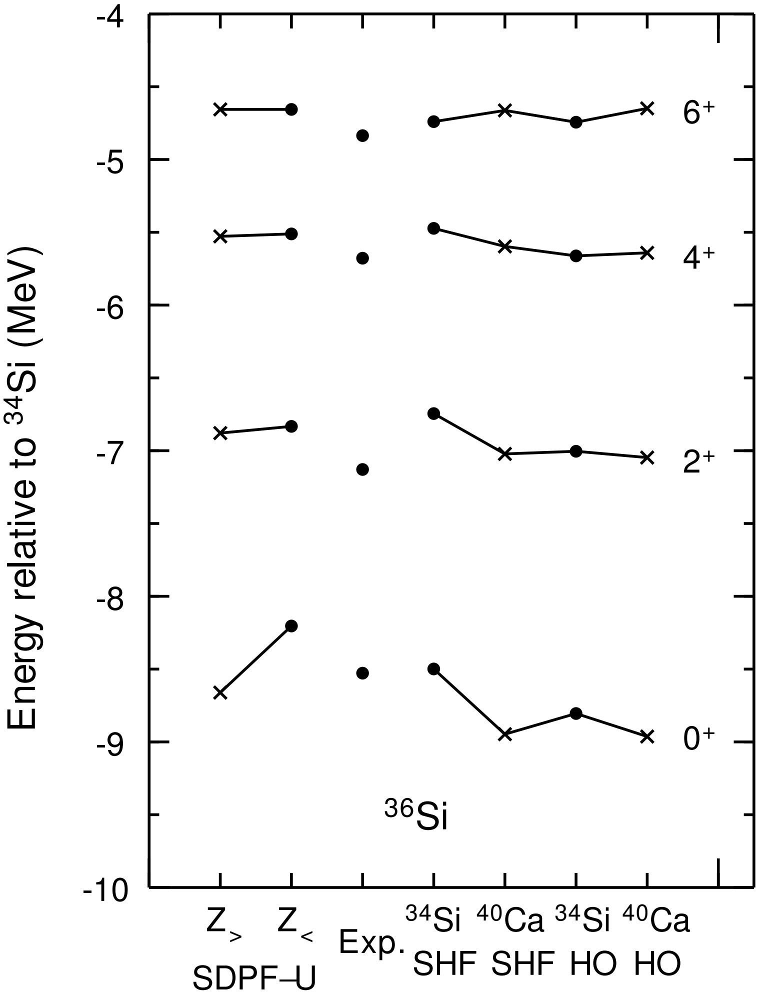

Figure 3.9: Calculations of the lowest-energy states for $J = 0, 2, 4, 6$ in ^{36}Si relative to ^{34}Si using the empirical SDPF-U interaction and the renormalization procedure for both ^{34}Si and ^{40}Ca as target nuclei, using the SHF and HO bases. Experimental data is shown for comparison, with a new mass from [63]. Crosses are used for calculations with ^{40}Ca as the target nucleus.

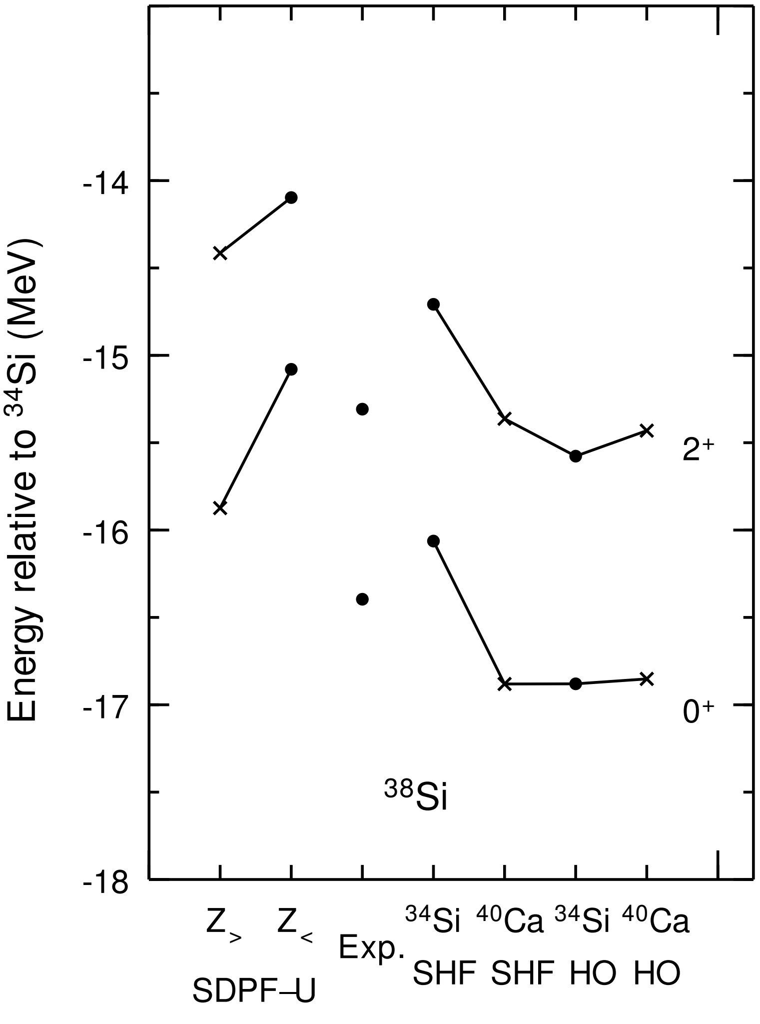

Figure 3.10: Calculations for the lowest-energy states for $J = 0$ and $J = 2$ in ^{38}Si relative to ^{34}Si using neutron-neutron matrix elements from SDPF-U and the renormalization procedure for both ^{34}Si and ^{40}Ca as target nuclei, in the SHF and HO bases. Crosses are used for calculations with ^{40}Ca as the target nucleus.

scheme for ^{36}Si is more spread out for the $Z \geq 15$ SDPF-U calculation than for the $Z \leq 14$ calculation, in agreement with the results discussed above. Calculations for each method are in reasonable agreement with the comparable SDPF-U calculation; the 0^+ state differs most with about 300 keV more binding compared to the respective empirical interaction for each core. The experimental binding energy relative to ^{34}Si is taken from a new mass measurement of ^{36}Si which is 140 keV higher in energy than previously measured [63]. The excitation energies of the $Z \leq 14$ SDPF-U calculation are comparable to experiment, as expected from an interaction fit specifically to neutron-rich silicon isotopes. While no interaction reproduces the experimental data very well, general trends can be seen. The calculations with ^{40}Ca as the target nucleus depicted by crosses result in level schemes that are too spread out in comparison to the experimental data. The reduction in the strength of the interaction for ^{34}Si using the SHF basis results in a reduction of the energy of the states in ^{36}Si, especially for the ground state (the pairing matrix elements were most reduced). The rms deviation between experiment and theory with ^{34}Si as the target nucleus in the SHF basis is 223 keV for the four states shown. One reason for this deviation is the lack of three body forces in the procedure. The inclusion of the NNN interaction, at least via the effective two-body part, is important for a higher level of accuracy. Additionally, the chosen SPE may contribute to the deviation, which would be better constrained if all the single particle states in ^{35}Si were known experimentally. For exotic nuclei, the calculated single particle state is often above the neutron separation energy and determination of the experimental single particle states may not be possible with current facilities. Thus it is essential to improve energy density functionals such that they provide reliable single particle energies.

As more nucleons are added, the disagreement between the various models increases as seen in Fig. 3.10, which plots the level scheme of ^{38}Si relative to ^{34}Si. Only the 0^+ and 2^+ states are shown since the 4^+ and 6^+ states are not known experimentally, but the binding energy is best reproduced by the calculations with ^{34}Si in the

SHF basis. As noted in the ^{36}Si case, the excitation energy of the 2^+ state is too high in the SHF basis but is reproduced well by the $Z \leq 14$ SDPF-U calculation for ^{38}Si. While the theoretical calculations of the binding energy vary by more than 750 keV for ^{36}Si in Fig. 3.9, the effect gets magnified as more particles are added. The binding energy of ^{38}Si varies by 1.8 MeV for twice the number of valence nucleons. Accurately accounting for the two-body interaction in the exotic medium is essential for calculations of exotic nuclei. The renormalization of a microscopic nucleon-nucleon interaction into the nuclear medium with a realistic basis and an appropriate target nucleus offers an improvement in the description of exotic nuclei, resulting in a decrease in the strength of the interaction and less binding in exotic nuclear systems.

The renormalization was performed in three different bases: harmonic oscillator, Skyrme Hartree-Fock, and a mix of harmonic oscillator and Skyrme Hartree-Fock. The choice of basis can significantly affect the value of matrix elements, as shown in the comparisons of pf neutron-neutron matrix elements for the stable ^{40}Ca and the neutron-rich ^{34}Si nuclei. The difference primarily results from the long tail of the radial wavefunctions relative to the harmonic oscillator wavefunction, especially for valence orbits bound by only a few hundred keV. The loosely bound orbits cause a reduction in the overall strength of the interaction, an effect that becomes magnified as full scale shell model calculations are performed. Accounting for the properties of the orbits by using a realistic basis is essential for an accurate description of the nuclear interaction in exotic nuclei as determined by the renormalization of an NN interaction, but NNN forces must be included for accuracy at the level of 100 keV.

Chapter 4

Single Particle Energies

Single particle energies enter the Hybrid Renormalization Procedure in two ways: through the basis in the calculation of Goldstone diagrams and through the effective interaction in the CI calculation. The dependence on SPE via Goldstone diagrams is minimal, as evidenced by the calculations in Chapter 3. Tables 3.1 and 3.2 display SPE for ^{34}Si and ^{40}Ca in the SHF basis and HO basis, respectively. Although the energies deviate on the order of MeV in the two different bases, the two-body matrix elements resulting from the calculation of Goldstone diagrams in Rayleigh-Schrödinger perturbation theory are not significantly affected by the energy differences. The MIX basis, which utilizes harmonic oscillator wavefunctions and SHF SPE, can be compared to the HO basis to quantify the contribution due to changes of the SPE on the order of MeV. In Table 3.3, the greatest deviation between a total matrix element in the HO and MIX bases for the same target is 25 keV. For a comparison with different targets, the core polarization diagram of Fig. 1.5 must be excluded since the occupation of proton orbits affects the size of the core polarization. For the remaining components of the two-body matrix elements (first order, particle-particle ladder, and four-particle two-hole), the deviations are still on the order of tens of keV, even though small changes in the HO wavefunctions for the two targets contribute as well.

The second form of SPE dependence, as a part of the CI calculation, will influence the results to a much larger degree. Therefore, it will be essential to evaluate the reliance on SPE as accurately as possible.

4.1 Definition of Single Particle Energy

Unfortunately, the term “single particle energy” is used throughout the nuclear structure community to describe several concepts, and so far in this work has not been treated carefully. As a result, a division into two categories, effective and uncorrelated SPE, is necessary. Uncorrelated SPE are defined as the solution to the mean field Hamiltonian in Eq. 1.6, where the energies represented by ϵ_α are completely independent. As seen from Eqs. 1.5 and 1.8, the energy difference between a nucleus with mass number A and a nucleus with mass number $A+1$ is $\epsilon_{\alpha_{A+1}}$. For instance, $E(^{17}O) - E(^{16}O) = \epsilon_{0d_{5/2}}$ assuming the standard filling of orbits as depicted in Fig. 2.9. Uncorrelated SPE do not correspond to an experimental quantity, because the single particle picture is only an approximate representation of physical nuclei. Uncorrelated SPE in the CI method are defined as the difference in energy between a single-reference calculation for the nucleus with mass number A and a single-reference calculation for the $A+1$ nucleus with the additional particle in a particular orbit. For example, in the *sd* shell with ^{16}O as the core, the calculation of ^{17}O with the USDB interaction is displayed in Fig. 4.1. The $5/2^+$ ground state and the $1/2^+$ and $3/2^+$ excited states are the only possible levels in the theoretical calculation since there is only one particle in the valence space. The selection of the *sd* model space enforces the single-reference nature of the ^{16}O and ^{17}O wavefunctions, such that no correlations from configuration mixing are included in the calculation. The energies of the states represent uncorrelated SPE for the model space orbits. As discussed in Section 1.1, effective interactions in standard model spaces often implement experimental energy differences as SPE. In particular, the USDB effective interaction treats the SPE as parameters, and reproduces the lowest experimental states in ^{17}O as seen in Fig. 4.1.

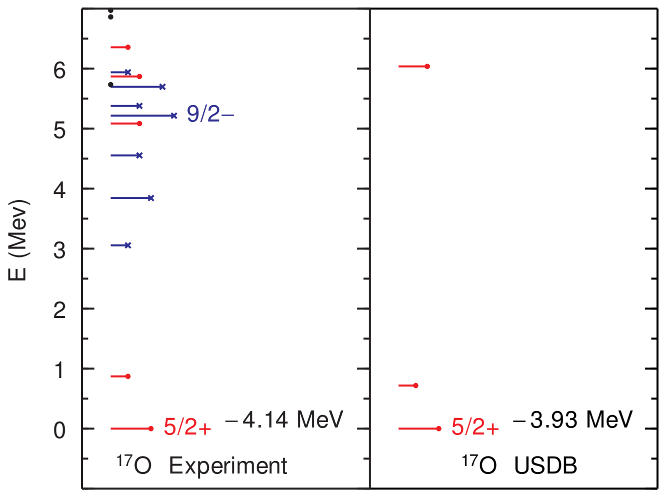

Figure 4.1: Comparison of the ^{17}O level schemes for experiment and for the USDB interaction. See the caption to Fig. 2.1 for details.

The accuracy of treating the ground state of ^{17}O as a $0d_{5/2}$ neutron coupled to a single Slater determinant, occupying the $N = 0$ and $N = 1$ oscillator shells, can be evaluated from experimental considerations. Spectroscopic factors for the addition and removal of a nucleon can be defined generally as

$$S_\alpha^+ = \mid \langle \Psi^{A+1} \mid a_\alpha^\dagger \mid \Psi^A \rangle \mid^2 \tag{4.1}$$

$$S_\alpha^- = \mid \langle \Psi^{A-1} \mid a_\alpha \mid \Psi^A \rangle \mid^2, \tag{4.2}$$

where the particle number has been singled out in the wavefunction. For a nucleus with even mass number A, the spectroscopic factors will be referred to generally as S, with the distinction between addition and removal apparent from the final state. To evaluate the treatment of ^{16}O as a single Slater determinant, the spectroscopic factor S^+ is of interest, with $A = 16$ and $\alpha = 0d_{5/2}$. A spectroscopic factor of unity would denote the accuracy of the single particle picture, such that the experimental energy would provide an uncorrelated SPE ϵ_α. However, physical states never achieve a unit spectroscopic factor as defined in Eq. 4.1. A neutron transfer reaction, such as

^{17}O(p,d)^{16}O, will probe the behavior of the "last" neutron in ^{17}O and can be used to determine spectroscopic factors. For this reaction, the spectroscopic factor of the ground state to ground state transition ranges from 0.74 to 0.99, with a proposed best value of 0.81 [64]. In Section 1.1, the mean field description of nuclei motivated the description of ^{16}O as a good core, such that ^{16}O could be treated as a vacuum. Even though the spectroscopic factor shows that other configurations contribute significantly, calculations throughout the *sd* shell confirm the validity of the shell model approximation. Local and short-range correlations contribute in nuclei; local correlations can be quantified by the behavior of valence particles in the *sd* model space, while short-range correlations are missing and contribute to physical properties at higher excitation energies (> 5 MeV as estimated from the energy to break the ^{16}O core). Configuration mixing must be taken into account to produce local correlations and to understand properties such as the fragmentation of spectroscopic strength.

Uncorrelated SPE for a Skyrme interaction are determined by the solution of the Skyrme Hartree-Fock equation for a particular nucleus. These uncorrelated SPE are determined in the potential well of the spherical mean field of the nucleus. As a result, the solution to one nucleus provides the entire single particle spectrum. The Skyrme SPE cited in the previous chapters were uncorrelated SPE determined in Skyrme Hartree-Fock theory.

An effective single particle energy (ESPE) is provided by the prescription of Baranger [65], who defines a centroid energy as

$$\epsilon_\alpha = \frac{\sum\limits_f (E_o - E_f^-) C^2 S_{\alpha_f}^- + (2J+1)(E_f^+ - E_o) C^2 S_{\alpha_f}^+}{\sum\limits_f C^2 S_{\alpha_f}^- + (2J+1) C^2 S_{\alpha_f}^+}. \tag{4.3}$$

For the ^{16}O $0d_{5/2}$ neutron ESPE, a sum over final states f in ^{17}O (S^+) and ^{15}O (S^-) is necessary, where E_o is the energy of ^{16}O, E_f^- are the energies of $5/2^+$ states in ^{15}O, E_f^+ are the energies of $5/2^+$ states in ^{17}O, and C is the isospin Clebsch-

Gordan coefficient [4]. Both particle and hole strength are included in Eq. 4.3. The denominator gives the total available occupation $(2J+1)$ of a given orbit α. The infinite summation can be prohibitive if the spectroscopic strength is fragmented across many states. Additionally, experimental restrictions on the detection of states at high excitation energies and on the determination of the principal quantum number for the spectroscopic factor prevent the full spectroscopic strength from being measured. In physical states, the local and short-range correlations cannot be isolated from one another. Spectroscopic strength can also be difficult to calculate theoretically, particularly with EDF methods which produce neither the explicit wavefunctions nor the necessary excited states. Configuration Interaction theory can be employed to determine theoretical ESPE. For the ^{16}O $0d_{5/2}$ ESPE in the sd model space, the hole states are outside the model space and the complete theoretical spectrum is given in Fig. 4.1. In this particular case, for one particle outside the core in the shell model, the summation over final states is eliminated and the effective and uncorrelated SPE are identical. The ESPE of model space orbits can be determined even for midshell nuclei, providing information solely on the local correlations.

The term single particle energy is used in scientific literature to denote other concepts beyond the uncorrelated SPE of Eq. 1.6 and the ESPE of Eq. 4.3. An example that will be referenced throughout this work is more accurately denoted the one-nucleon separation energy. The one-nucleon addition energy for particles outside a core with A nucleons is given by

$$E_\kappa^+ = \langle \Psi_\kappa^{A+1} \mid H \mid \Psi_\kappa^{A+1} \rangle - \langle \Psi^A \mid H \mid \Psi^A \rangle, \tag{4.4}$$

where κ denotes the quantum numbers of the $A+1$-body state of interest. A similar equation can be derived for the one-nucleon removal energy E_κ^- of holes from the core. The separation energies for a nucleus are given by E_κ^+ and E_κ^-. Experimental one-nucleon separation energies, as given by experimental binding energy differences, include all correlations. In the lowest-state approximation, the experimental one-nucleon separation energy from an even-even nucleus with ground state 0^+ to an odd-A nucleus with $J_k^\pi = j^{(-1)^\ell}$ represents the ESPE of the orbit with $\alpha = (n, \ell, j)$. Only in a purely single particle picture, i.e. assuming a spectroscopic factor of one, would the energy difference between the two physical states exactly determine the ESPE of the orbit α. The lowest-state approximation for single particle energies is evaluated in Sections 4.2 and 5.1.

For uncorrelated SPE, a nearly identical equation can be written, substituting H_0 for H and Ψ_0 for Ψ, where the Slater determinant Ψ_0 is the solution to H_0 in Eq. 1.5. Theoretically, one-nucleon separation energies are determined by making an approximation to the nuclear Hamiltonian. For instance, with the nuclear potential in the form of the Skyrme interaction, one-nucleon separation energies can be determined from Skyrme Hartree-Fock solutions to three nuclei with mass number $A, A-1$, and $A+1$, where the wavefunction Ψ is represented by a single Slater determinant. Similarly, the truncation to a reduced model space, where Ψ and H represent the many-body wavefunction and Hamiltonian outside the core, enables the calculation of one-nucleon separation energies with Configuration Interaction theory.

4.2 Comparison of Effective SPE and One-Nucleon Separation Energies

A comparison between ESPE and one-nucleon separation energies is instructive, especially since the distinction is not generally made in the literature. Michimasa et al., in a study of ^{23}F, found that the low-lying states were not reproduced accurately by the USD interaction [66]. They conclude that “this may be attributed to an increase in the energy difference of the single-particle energies,” and found reasonable agreement with experiment by changing the SPE parameters in the USD effective interaction. They cited an increase in spin-orbit splitting for the $0d_{5/2}$ and $0d_{3/2}$

Table 4.1: Comparison of spectroscopic factors C^2S for experiment and for three *sd* Hamiltonians in the proton capture reaction on ^{22}O.

E (MeV)	J^π	Exp.	USD	USDA	USDB
0.00	$5/2^+$	n/a	0.80	0.77	0.78
2.27	$1/2^+$	$0.36^{+0.10}_{-0.16}$	0.67	0.64	0.65
4.06	$3/2^+$	$0.24^{+0.07}_{-0.09}$	0.47	0.56	0.47

proton orbits relative to the case at ^{17}F. Their conclusion was based on a comparison between the lowest-energy experimental states with large spectroscopic factors in the proton transfer reaction ^{4}He(^{22}O,^{23}Fγ)^{3}H and the single particle states in ^{17}F, consisting of one proton outside the ^{16}O vacuum. Though they did not make the distinction, Michimasa et al. were comparing one-nucleon separation energies instead of the appropriate ESPE. Since the physical states in ^{23}F are not represented accurately by single particle states, a better comparison between ^{17}F and ^{23}F is achieved with effective SPE from Eq. 4.3.

Table 4.1 includes the experimental and theoretical values for the strong proton transfer spectroscopic factors for three *sd* shell Hamiltonians. (In Fig. 5 of [66], the authors list values of $(2J+1)C^2S$ for two experimental levels and for the USD calculations. However, the theoretical values listed are actually for $(2J+1)S; C^2 = 6/7$ for this reaction.) The three Hamiltonians give similar results, with at most 20% difference for the $3/2^+$ state. The ratio of the experimental and theoretical spectroscopic factors of about 0.50 is consistent with the global reduction factor observed in nucleon transfer and nucleon knockout reactions shown in Fig. 2 of [67]. This reduction factor is attributed to configuration mixing beyond the *sd* shell, including those due to the short-range and tensor two-nucleon correlations [68].

Fig. 4.2 shows summed proton transfer C^2S_f values as a function of $E_f - E_o$ for USDB, where E_f are the energies of states in ^{23}F and E_o is the energy of the ^{22}O ground state. The calculated energy difference between ^{22}O and ^{23}F includes the 3.48 MeV Coulomb energy correction for $Z = 9$ relative to $Z = 8$ [15]. This plot shows that the lowest-energy state for each spin only contains 50-80% of the total strength.

The remaining strength is fragmented over many final states up to 15 MeV higher in energy. The large fragments of strength near $E_f - E_o = 0 - 5$ MeV correspond to the strength going to the $T \geq 7/2$ isospin states that are the isobaric analogues of the low-lying states of ^{23}O.

The centroid single particle energies given by Eq. 4.3 are shown on the right-hand side of Table 4.2. The S^- terms do not contribute because nitrogen is outside of the *sd* model space. The centroid energies are significantly higher than the lowest-state energies, with energy shifts of four MeV for the $0d_{3/2}$ and $1s_{1/2}$ orbits with all interactions.

The best experimental information available for the fragmentation of proton single particle strength in the fluorine isotopes is from the ^{18}O(d,n)^{19}F experiment of [69]. The spectroscopic factors from this experiment are compared to the calculation with USDB in Fig. 4.3. The fragmentation to $T \geq 5/2$ states is large, as evidenced by the behavior of the lowest $T = 5/2$ state, which is the strong $5/2^+$ state at 7.54 MeV (at $E_f - E_o = -0.46$ MeV in Fig. 4.3). The experimental data stops at an excitation energy of 14 MeV where the experimental lines stop in Fig. 4.3. Most of the theoretical strength is below 14 MeV excitation with the exception of a large value for $3/2^+$ near 14 MeV. Thus some $d_{3/2}$ strength may be missed. The overall pattern of experimental strength distributions is in excellent agreement with theory except that the $d_{3/2}$ strength above 10 MeV in excitation (above $E_f - E_o = 2$ MeV in Fig. 4.3) is more fragmented in experiment than theory, presumably due to mixing with intruder states coming from two nucleons excited from the *p* shell to the *sd* shell or from the *sd* to the *pf* shell.

For ^{23}F, a comparison of USDA and USDB results gives an estimate of the theoretical error in the centroid energy of 0.1, 0.4 and 0.4 MeV for $0d_{5/2}$, $1s_{1/2}$ and $0d_{3/2}$, respectively. The $0d_{5/2} - 0d_{3/2}$ proton spin-orbit splitting for ^{23}F is thus estimated to be 6.2(4) MeV. With USDB, the spin-orbit splitting can be found from the proton-drip line, 6.0 MeV in ^{17}F, to the neutron drip line, 6.9 MeV in ^{29}F. Thus, including the

Table 4.2: Proton separation energies for ^{23}F relative to ^{22}O based on the lowest state for each spin and the centroid energy from Eq. 4.3 for each n,ℓ, j value.

	lowest-energy state				centroid energy		
nℓ_j	Exp.	USD	USDA	USDB	USD	USDA	USDB
$0d_{5/2}$	-13.20	-13.05	-13.28	-13.26	-11.16	-11.21	-11.31
$1s_{1/2}$	-10.93	-11.27	-11.03	-11.27	-7.58	-6.92	-7.34
$0d_{3/2}$	-9.14	-9.55	-9.59	-9.28	-5.04	-5.46	-5.09

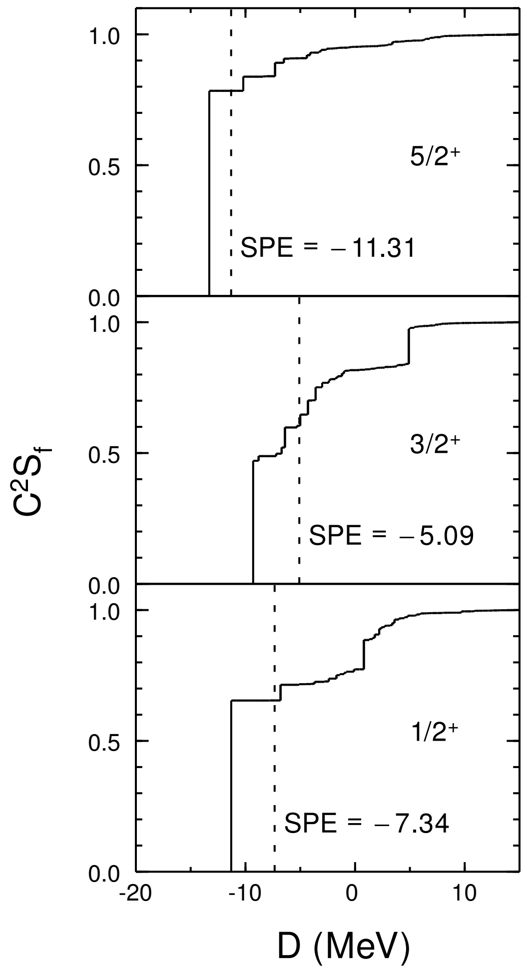

Figure 4.2: C^2S_f vs. D= $E_f - E_o$ for ^{23}F as the product of a proton transfer reaction using the USDB Hamiltonian. The dotted lines mark the centroid energies.

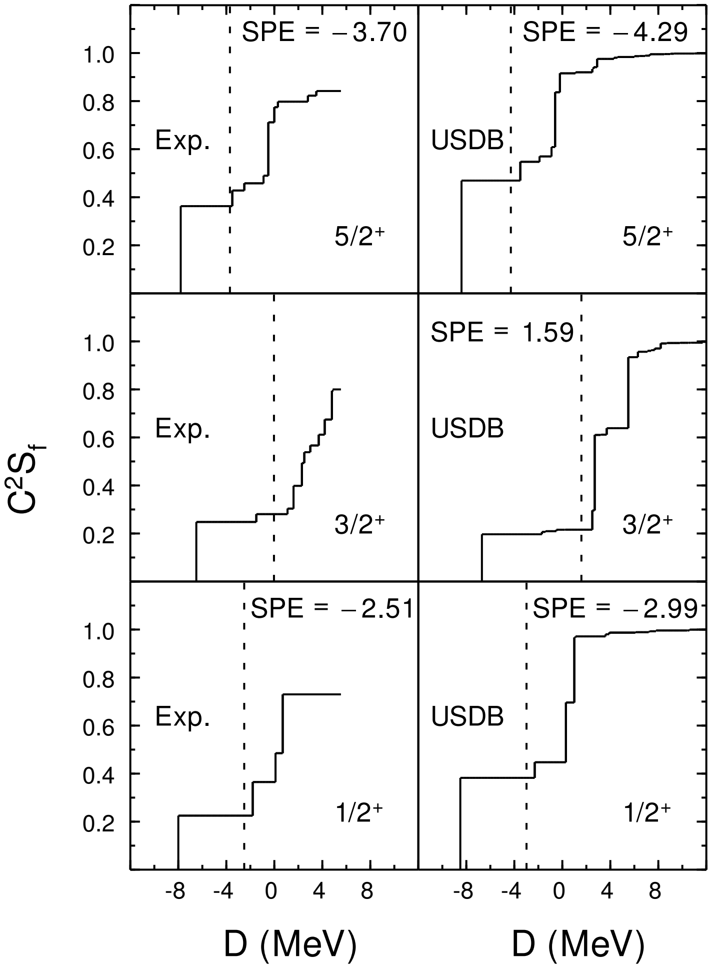

Figure 4.3: C^2S_f vs. D= $E_f - E_o$ for experimental [69] and USDB calculations for ^{19}F as the product of a proton transfer reaction. The dotted lines mark the centroid energies. The $3/2^+$ experimental centroid energy is not listed because the strength was not measured above $E_f - E_o = 6$ MeV, near the theoretical state at $E_f - E_o = 5.54$ with a large spectroscopic factor.

uncertainty of the calculation, the spin-orbit splitting is nearly constant as a function of neutron number when comparing ESPE from the centroid energy instead of the lowest-state energy from an approximate single particle picture.

Similarly, Gaudefroy et al. discuss the behavior of the spin-orbit splitting in ^{49}Ca and ^{47}Ar based upon one-nucleon separation energies given by lowest-energy states observed in the ^{46}Ar(d,p)^{47}Ar reaction [70]. They deduce a 45(10)% reduction in the $p_{3/2} - p_{1/2}$ spin-orbit splitting for Ar ($Z = 18$) compared to Ca ($Z = 20$). However, there is significant fragmentation of the pf-shell spectroscopic strength between ^{45}Ar and ^{47}Ar which must be taken into account to evaluate the shifts of ESPE and to determine the spin-orbit splitting.

The calculations for ^{47,48,49}Ca and ^{45,46,47}Ar were carried out using OXBASH [6] and the *sdpf* interaction from Nummela et al. [47], where proton excitations are restricted to the *sd* shell and neutron excitations are restricted to the *pf* shell. The same calculation was carried out in [70] to produce a level scheme for ^{47}Ar in reasonably good agreement with experiment. In both ^{47}Ar and ^{49}Ca the first excited state has $J^{\pi} = 1/2^{-}$ with experimental (theoretical) excitation energies of 2.02 (1.70) MeV for ^{49}Ca and 1.13(8) (1.28) MeV for ^{47}Ar. Gaudefroy et al. deduce a reduction of spin-orbit splitting around the $N = 28$ shell closure as a result of this decrease in excitation energy. Taking into account both particle and hole strength through Eq. 4.3 for the $p_{1/2}$ and $p_{3/2}$ orbits, the reduction does not occur. For all final nuclei, 200 states were included; this is enough to exhaust over 99% of the $(2J+1)$ sum-rule strength for all isotopes of interest. As seen in Fig. 4.4, the lowest-energy states in ^{49}Ca account for 95% of the total spectroscopic strength for the $p_{1/2}$ and $p_{3/2}$ orbits, whereas the lowest-energy states in ^{47}Ar account for only 80% and 65%, respectively, of the total strength. The change of the spin-orbit splitting is of interest: $\delta\epsilon_{so} = [\epsilon(\mathrm{Ar}, p_{1/2}) - \epsilon(\mathrm{Ar}, p_{3/2})] - [\epsilon(\mathrm{Ca}, p_{1/2}) - \epsilon(\mathrm{Ca}, p_{3/2})]$. Given that there is some difference between experiment and theory for the energies of the lowest $3/2^{-}$ and $1/2^{-}$ states in ^{47}Ar and ^{49}Ca (as noted above), the experimental shift of

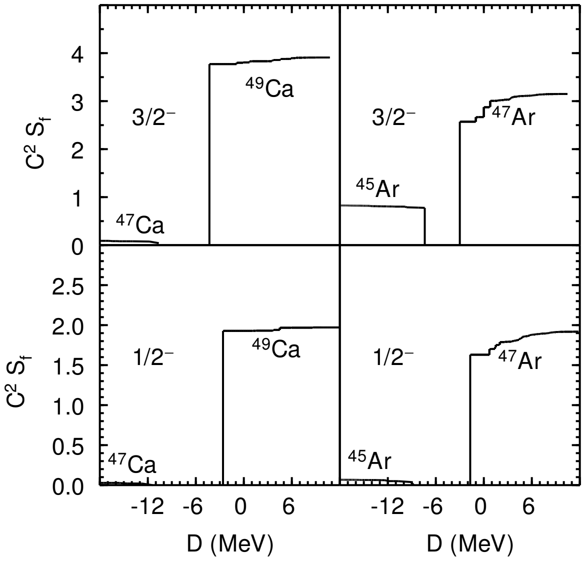

Figure 4.4: C^2S_f vs. D= $E_f - E_o$ from the initial ground states in ^{48}Ca and ^{46}Ar to $1/2^-$ and $3/2^-$ states via the addition or subtraction of a neutron. The large fragmentation of strength for ^{46}Ar, not evident in ^{48}Ca, results in deviation between the ESPE and the energy of the lowest state in ^{47}Ar.

$-0.89(13)$ MeV provides a starting point as the difference in experimental one-nucleon separation energies. A theoretical correction due to fragmentation, $+0.88$ MeV, is determined by the theoretical shift from the lowest-state energy to the centroid energy. This correction is added to the change in one-nucleon separation energies to obtain $\delta\epsilon_{so} = -0.01(13)$ MeV. In another procedure, the experimental binding energies and theoretical excitation energies are entered directly into Eq. 4.3 to obtain $\delta\epsilon_{so} = +0.09(13)$ MeV. In either case, the result shows no change in the spin-orbit splitting within the uncertainty in the calculation. Again, a comparison of ESPE rather than the lowest state of a given value of total angular momentum is necessary to determine spin-orbit splitting. The splitting is constant for changes in proton number at $N = 28$, in agreement with the result for fluorine isotopes as a function of neutron number.

4.3 SPE Dependence of CI Calculations

As seen in Fig. 2.1, the binding energy of ^{18}O with the HRP-SD interaction is 3.9 MeV larger than experiment. Extending the calculation to third order in perturbation theory increases the deviation to 4.2 MeV, although it improves the description of the 4^+ state as mentioned in Section 2.2. The two interactions employ identical single particle energies, determined from the Skyrme Hartree-Fock solution to the mean field for ^{16}O with the Skxtb interaction. If the one-nucleon separation energies of the Skxtb calculation as determined by Eq. 4.4 were implemented in the HRP-SD interaction, the result would not change significantly. Table 4.3 compares the uncorrelated Skxtb single particle energies, along with the ESPE from the empirical USDB interaction and the lowest experimental $5/2^+, 3/2^+, 1/2^+$ states in ^{17}O. From the definitions in Section 4.1, the experimental states provide neither uncorrelated or effective SPE, but are the appropriate input for an effective interaction in the *sd* shell with ^{16}O as the core. Unlike the CI calculation, the physical states cannot simply be represented by an *sd* neutron coupled to a configuration of ^{16}O with filled $N = 0$ and $N = 1$ oscillator shells and instead include all correlations. The spectroscopic factors for these states are not equal to one, indicating that ^{16}O can only approximately be treated as a core. Without accounting for the full fragmentation of the single particle strength, which is not known experimentally, the experimental ESPE cannot be determined. The USDB interaction, as fit to data throughout the *sd* shell, can provide an estimate for the single particle energies necessary to reproduce local correlations in the *sd* shell. A comparison to the values determined from experimental states in ^{17}O suggests that only the $0d_{3/2}$ orbit has significant modification, with an increase in energy from 0.94 to 2.11 MeV. The uncorrelated SPE for the Skxtb interaction differ from both the USDB ESPE and the experimental states for all three orbits. Since the USDB ESPE differ significantly from the results with the Skyrme interaction, the binding energy for ^{18}O with the HRP-SD interaction deviates significantly from experiment. If the

Table 4.3: A comparison of the lowest-energy experimental states in ^{17}O for each spin, neutron ESPE with the USDB interaction, and the uncorrelated SPE of the Skxtb interaction from the Skyrme Hartree-Fock solution to the mean field in ^{16}O.

$n\ell_j$	Exp.	USDB	Skxtb SPE
$0d_{5/2}$	-4.14	-3.93	-6.22
$1s_{1/2}$	-3.27	-3.21	-3.73
$0d_{3/2}$	0.94	2.11	0.30

two-body matrix elements from the HRP-SD interaction are combined with the USDB ESPE (experimental one-nucleon separation energies), the binding energy of ^{18}O relative to ^{16}O is 11.75 (12.24) MeV, in reasonable agreement with the experimental value of 12.19 MeV. If instead the TBME derived from a calculation to third order in perturbation theory are used, the resultant binding energy is 12.18 (12.65) MeV. In other words, the Skxtb interaction produces a $0d_{5/2}$ uncorrelated SPE approximately two MeV too low in energy, which results in a four MeV increase in the binding energy of ^{18}O. As more valence particles are added, the agreement with experiment worsens.

Single particle energies also contribute to the CI calculation through the amount of configuration mixing, which is a function of the energy differences or gaps between model space SPE. This nonlinear effect depends on the complicated matrix diagonalization, and will not be evaluated quantitatively. It is essential for the effective interaction to contain accurate SPE in order to produce reliable results throughout the model space. As discussed in Section 1.1, lowest-energy experimental states and uncorrelated SPE often provide the single particle energies of effective interactions. For standard model spaces, this approximation is reasonable, as seen in the two leftmost columns of Table 4.3. However, the approximation is not viable for the HRP as described in Chapter 2 if the target nucleus does not have large energy gaps at the Fermi surface, i.e. if the target is not a magic nucleus. The uncorrelated SPE of Skyrme forces, which have been used as the one-body component of effective interactions thus far, must be evaluated in greater detail for midshell nuclei.

Table 4.4: Uncorrelated neutron single particle energies in MeV for ^{16}O with the Skx, Skxtb, Sly4, and MSk7 interactions.

$n\ell_j$	Skx	Skxtb	Sly4	MSk7
$0s_{1/2}$	-30.20	-30.11	-34.52	-28.95
$0p_{3/2}$	-18.38	-18.36	-19.23	-18.14
$0p_{1/2}$	-13.45	-13.34	-13.48	-12.54
$0d_{5/2}$	-6.16	-6.22	-5.79	-6.82
$0d_{3/2}$	0.24	0.30	0.61	0.29
$1s_{1/2}$	-3.72	-3.73	-3.37	-4.38
$0f_{7/2}$	7.07	6.94	6.32	5.65
$0f_{5/2}$	15.44	15.47	13.83	14.68
$1p_{3/2}$	5.31	5.27	4.34	4.52
$1p_{1/2}$	6.50	6.48	5.50	6.00

Table 4.5: Uncorrelated neutron single particle energies in MeV for ^{22}O with the Skx, Skxtb, Sly4, and MSk7 interactions.

$n\ell_j$	Skx	Skxtb	Sly4	MSk7
$0s_{1/2}$	-28.85	-28.71	-37.97	-29.16
$0p_{3/2}$	-16.94	-17.50	-20.72	-17.35
$0p_{1/2}$	-12.73	-11.05	-15.42	-12.16
$0d_{5/2}$	-5.96	-6.85	-6.26	-6.49
$0d_{3/2}$	0.24	1.42	0.73	1.03
$1s_{1/2}$	-4.81	-4.84	-4.10	-5.05
$0f_{7/2}$	5.69	4.65	5.79	4.91
$0f_{5/2}$	14.42	15.70	14.61	15.45
$1p_{3/2}$	4.15	3.93	3.86	3.70
$1p_{1/2}$	5.01	5.64	4.81	4.80

4.4 Skyrme Single Particle Energies

The Hybrid Renormalization Procedure is designed to connect to the underlying physics and to avoid unnecessary parameters. However, an effective interaction requires reliable single particle energies in order to reproduce low-energy excitations throughout the model space. For a target nucleus outside of the core of a model space, an approximate method to determine single particle energies introduces as many parameters as model space orbits and fits to experimental data in the model space. This procedure is implemented for the application of the HRP to the island of inversion region in Section 5.1. The parameters are unnecessary if Skyrme interactions are able to provide uncorrelated SPE or one-nucleon separation energies that are consistently close to the experimental ESPE. The ten lowest uncorrelated SPE for the doubly magic ^{16}O and the exotic closed subshell ^{22}O are shown in Tables 4.4 and 4.5, respectively, for different paramaterizations of the Skyrme interaction. In addition to the Skx and Skxtb interactions discussed in detail in Section 1.2, SPE are obtained from the Sly4 [56] and MSk7 [71] interactions. For the exotic case, the difference between the Skx and Skxtb results in Table 4.5 display the effect of the tensor force, which can be greater than one MeV as seen from the $0d_{3/2}$ orbit, for instance. For orbits in the valence space of these nuclei (the *sd* model space), the values change by about one MeV for the four parameterizations of the Skyrme interaction. As noted in Section 4.3, this corresponds to a change of two MeV in the binding energy of ^{18}O. For practical purposes, since a reproduction of the low-energy states of nuclei in a given model space on the hundred keV level is desired, the Skyrme SPE are unsatisfactory.

The level density of the single particle spectrum in Skyrme Hartree-Fock calculations is dependent on the effective mass of the Skyrme interaction, which differs for the four parameterizations in Tables 4.4 and 4.5. As a result, the uncorrelated SPE for deeply bound orbits can vary significantly, by nearly ten MeV for the $0s_{1/2}$ orbit in ^{22}O. An effective mass approximately equal to the mass of a nucleon, as in the Skx and Skxtb interactions, can provide an accurate single particle spectrum for ^{208}Pb, while a reduction of 20% as in Sly4 is necessary to reproduce the spectra in light nuclei [29]. However, it is impossible to reproduce experimental one-nucleon separation energies for both ^{208}Pb and light nuclei with the Skyrme interaction [29]. Since an energy density functional should describe all nuclei equally, the mass dependence indicates that the Skyrme interaction does not correspond to the realistic microscopic functional. With a microscopic energy density functional that has an effective mass equal to the mass of a nucleon, the one-nucleon separation energies are expected to describe the experimental ESPE, and therefore will not necessarily agree with the experimental one-nucleon separation energies. To reproduce the experimental energy spectrum and spectroscopic behavior, multi-reference EDF methods must be applied on top of the SR-EDF calculation. Such calculations are outside the scope of this work, but the single particle properties of both light and heavy nuclei are not reproduced by any current functionals, whether single- or multiple-reference EDF methods are employed.

The one-nucleon separation energies of the Skyrme interaction should have been preferentially chosen over the uncorrelated SPE as the input to effective interactions. Even though the Skyrme interaction is described as a mean field interaction, the one-nucleon separation energies are only approximately given by Eq. 1.8. The density-dependent term in Eq. 1.18 represents a zero-range three-body force and produces correlations which vary based on the parameterization [72]. To solve the Skyrme Hartree-Fock equation for odd nuclei, the symmetry related to time-reversal invariance must be broken. To calculate the one-nucleon separation energies with a time-reversal invariant Skyrme Hartree-Fock code, the equal filling approximation is implemented, where an average over time-reversal partners is considered. The energy in this approximation will be greater than the solution which breaks time-reversal invariance, but the accuracy of the equal filling approximation is not currently known and must be analyzed in more detail. From preliminary investigations with the equal filling approximation, the one-nucleon separation energies of different Skyrme parameterizations have a smaller variance than the uncorrelated SPE, another beneficial result. However, the results from either method deviate significantly from experiment for light nuclei. A complete evaluation of the one-nucleon separation energies and their relation to uncorrelated SPE for stable and exotic nuclei with EDF methods is a topic for future research. The implementation of Skyrme separation energies into the effective interactions in Chapter 3 and Sections 2.2 and 5.2 should be performed (see Chapter 6) but is not expected to require modification to the conclusions drawn in this work.

Tables 4.4 and 4.5 display a variation of uncorrelated SPE of approximately one MeV in the valence space for the different parameterizations. However, there is no guarantee that the range of values agrees with the physical ESPE. The $0d_{5/2}$ neutron SPE from Table 4.4, which vary from -5.79 to -6.82 MeV, differ from the experimental one-nucleon separation energy and the USDB SPE from Table 4.3, -4.14 and -3.93 MeV respectively, by as much as 2.9 MeV. It should be noted that light nuclei in general are not reproduced by the Skyrme functionals, which better describe heavier nuclei. Until a functional is derived that improves upon the Skyrme single particle spectra, an uncertainty of at least one MeV in SPE must be accepted when experimental data does not provide approximate values.

The difficulty in obtaining ESPE and the unreliability of uncorrelated Skyrme SPE motivate several methods to determine SPE for effective interactions derived from the Hybrid Renormalization Procedure:

(i) Select a core such that the lowest-energy experimental states are good representations of single particle states as discussed in Section 4.2. For ^{17}O, the three lowest positive parity states in Fig. 4.1 have large spectroscopic factors [73] with J^{π} values that correspond to one valence nucleon outside of the core. The energy of these lowest states should approximate the physical ESPE, which cannot be determined experimentally.

(ii) As in the case of empirical interactions like USDB, treat the SPE as parameters and fit to available data in the region. In this way, the SPE are constrained to reproduce values close to the ESPE by the data.

(iii) Directly utilize results from Skyrme Hartree-Fock theory with caution, realizing that the deviation from the ESPE can be more than one MeV.

The remainder of this dissertation is devoted to applications of the HRP, with a focus on comparison to recent experimental quantities of interest. Effective interactions will consist of two-body matrix elements calculated from the HRP as described in Chapter 2, with single particle energies determined from one of the three methods above in order to provide the most reliable comparison to experimental data.

Subsequent to the completion of this dissertation, a forthcoming work by Duguet et al. [74] was brought to the author's attention. Two important results relevant to this work are:

(i) One-nucleon separation energies determined via EDF methods can be identified with SR-EDF ESPE. As discussed above, but now based on a formal derivation, the one-nucleon separation energies from the Skyrme interaction should supplant the Skyrme uncorrelated SPE in the SPE component of effective interactions derived with the HRP.

(ii) The treatment of ESPE in Eq. 4.3 is an approximation. The meaningful definition of ESPE requires the computation of a centroid matrix, as described in the work of Baranger [65], which reduces to Eq. 4.3 only in the diagonal basis of the matrix. The off-diagonal terms in the bases constructed in this work have been neglected. The effect on the ESPE as a result is unknown and must be studied in more detail.

See Section 6.3 for a discussion of possible future work based on these results.

Chapter 5

Applications

As discussed in Section 1.7, standard Configuration Interaction techniques struggle to produce accurate results outside of standard model spaces in the region of applicability, shown in Fig. 1.6. The island of inversion region and neutron-rich silicon isotopes were identified as cases of recent experimental interest which are appropriate for the Hybrid Renormalization Procedure. Extensive calculations will be performed with interactions derived from the HRP in order to display the utility and accuracy of the method.

5.1 Island of Inversion Region

The first evidence of the island of inversion region was noted by Thibault et al. during a study of the masses of neutron-rich sodium isotopes [42]. Particularly for ^{31}Na, which should display extra stability in comparison to nearby isotopes due to the closure of the sd neutron shell at $N = 20$, the measured binding energy was larger than the shell model predictions. The occupation of pf orbits in the ground state increases the binding energy in the form of additional correlation energy. The inversion of the standard filling of neutron orbits near $N = 20$ has since been identified for several nearby nuclei, and this island of inversion is currently under investigation in several experimental facilities.

The island of inversion exists at the edge of nuclear structure research with exotic beams, so the boundaries of the region have not yet been determined. The inversion has been observed in nuclei with both $N \geq 19$ and $Z \leq 13$, but the extent of ground states in this region with inverted configurations is unknown. The high-N and low-Z boundaries have not been investigated at all experimentally. Following the Hybrid Renormalization Procedure of Chapter 2, the first step requires the selection of a model space and target nucleus near the region of interest. The island of inversion region, as determined by an evaluation of the available experimental evidence, is centered around ^{31}Na. The selected model space to calculate nuclei in this region is composed of the $0d_{5/2}, 0d_{3/2}, 1s_{1/2}$ proton orbits and of the $0d_{3/2}, 1s_{1/2}, 0f_{7/2}, 1p_{3/2}, 1p_{1/2}$ neutron orbits. The entire *sd* and *pf* shells cannot be included for the neutron orbits due to computational restrictions on the diagonalization of the Hamiltonian. Therefore, the $0d_{5/2}$ and $0f_{5/2}$ orbits, the most bound and unbound orbits respectively, are excluded from the model space. Calculations in the *sd* shell suggest that excitations from the $0d_{5/2}$ orbit affect level schemes on the order of 250 keV around $N = 18$, while the six MeV spin-orbit splitting between the $0f_{7/2}$ and $0f_{5/2}$ orbits causes a minimal contribution from the exclusion of the $0f_{5/2}$ orbit up to $N = 28$.

The core of the model space, ^{22}O, is selected as the target nucleus for the Hybrid Renormalization Procedure. Even though it is further away from ^{31}Na than ^{34}Si or ^{28}O, the core is more conducive to a straightforward treatment of three-body forces through the addition of monopole terms to the Hamiltonian. As shown by Otsuka et al. in Fig. 2 of [75], the main contribution of the three-body force can be represented by a repulsive two-body monopole interaction between two valence nucleons and one nucleon in the core. Additionally, ^{22}O has approximately the correct asymmetry for the region ($N/Z = 1.8$, in comparison to $N/Z = 2.1$ for ^{31}Na).

With the standard implementation of the Hybrid Renormalization Procedure in this model space with ^{22}O as the target, the low-energy behavior of nuclei in the model space is not reproduced. Two problems with the HRP, previously discussed in Section 2.2, are the Skyrme single particle energies and lack of three-body forces. Following step (vii) of the HRP and the discussion in Chapter 4, three-body forces and SPE are parameterized. Twelve free parameters are included: SPE for each orbit (eight total), and valence monopole terms for a proton-proton, neutron-neutron, proton-neutron, and three-nucleon interaction. The two-body monopoles are given by $\frac{C_{ij}}{1+\delta_{ij}} O_i(O_j - \delta_{ij})$, where i, j denote the type of nucleon (proton or neutron) and O_i is the occupation number of valence nucleons of type i. The three-body monopole is symmetric with respect to isospin and is given by $\frac{C_3}{6} A_{val}(A_{val} - 1)(A_{val} - 2)$. With these twelve parameters, the 2^+ energies of even-even nuclei in the model space could not be reproduced to the desired accuracy. Therefore, a phenomenological normalization of the two-body matrix elements was included as a thirteenth parameter, serving to reduce the overall strength of the interaction by approximately 10%. In Chapter 3, a reduction in the overall strength of the interaction was observed due to loosely bound orbits. With ^{22}O as the target, there are no loosely bound orbits, whereas a target nucleus near the island of inversion region like ^{28}O or ^{34}Si has loosely bound neutron orbits with the Skxtb interaction. The overall normalization can represent an empirical way to account for the reduction in the strength of the interaction due to these loosely bound orbits.

With thirteen parameters, a fit to data is required. Even though ^{22}O, the core of the model space, was selected as the target in the HRP, the single particle properties in the island of inversion region are more comparable to those of the midshell nucleus ^{34}Si. Therefore, the known states with one particle added to or removed from ^{34}Si are included in the fit to constrain the single particle energy parameters. From the ENSDF database [53], the lowest two states in ^{33}Al (both $5/2^+$), the lowest two states in ^{35}P ($1/2^+$, $3/2^+$), and the lowest four states in ^{33}Si ($3/2^+$,$1/2^+$, $7/2^-$,$3/2^-$) are known. Nuclei whose spin and parity have been determined from "weak" rules [76] are assumed to be accurate throughout this section. The three lowest states in ^{35}Si ($7/2^-$,$3/2^-$,$3/2^+$) were determined in [47], but the $1/2^-$ state is also necessary to constrain the $1p_{1/2}$ SPE. The value is estimated from a systematic study of spin-orbit splitting in $N = 20$ isotones with the Skxtb interaction; the result is 350 keV higher than a recently identified state in ^{35}Si. The spin and parity have not been determined in the preliminary results, but a full analysis of the experimental data is still in progress [77]. The overall normalization is constrained by including the 0^+ and 2^+ states of ^{34}Si and two-particle or two-hole excitations from ^{34}Si. The monopoles are constrained by including data from the lightest isotopes to the heaviest isotopes of interest, but states near the island of inversion are also included to better reproduce the primary region of interest. The ground states of the light nuclei ^{24}O (0^+) and ^{27}F ($5/2^+$), the three lowest known states of the heavy nuclei ^{37}Cl ($3/2^+$,$1/2^+$,$5/2^+$) and ^{38}S (0^+,2^+,4^+), and the island of inversion nuclei ^{31}Na ($3/2^+$,$5/2^+$), ^{30}Ne (0^+,2^+,4^+) [78], ^{30}Mg (0^+,2^+,0^+) [79], and ^{31}Mg ($1/2^+$,$3/2^+$,$3/2^-$,$7/2^-$) [80] are also included. These 43 states are implemented in an iterative fitting procedure to constrain the thirteen parameters.

The parameters are included in Table 5.1. The small three-body monopole supports the conclusion of Otsuka et al. [75] that the three-body force can be represented by repulsive two-body monopole interactions. The rms deviation to the 43 experimental states is 370 keV, larger than the standard CI Hamiltonians in the *sdpf* space by approximately a factor of two. An effective interaction applicable throughout the island of inversion region, called IOI, is composed of the four monopole terms, the eight parameterized SPE and the two-body matrix elements from the HRP multiplied by the overall normalization.

One hundred nuclei were calculated from proton number $Z = 8$ to $Z = 17$ and from neutron number $N = 15$ to $N = 24$. The first quantity of interest is the binding energy of these nuclei relative to experiment. Fig. 5.1 displays the calculated energy differences, with experimental masses taken from [81]. However, it must be

Table 5.1: Values of parameters for the IOI interaction obtained from a fit to 43 experimental states near the island of inversion region of the nuclear chart. The first eight parameters are single particle energies, the next four are coefficients in monopole terms, and the final parameter is a normalization coefficient for the two-body matrix elements. The initial values of the first eight parameters are uncorrelated SPE obtained from the Skyrme Hartree-Fock solution to the mean field for ^{34}Si with the Skxtb interaction, while the final values are uncorrelated SPE from a single-reference CI calculation, as discussed in Section 4.1. Typically, the one-nucleon separation energies for ^{34}Si with the Skxtb interaction would be chosen as the initial values as discussed in Section 4.4, but the output of the fit, i.e. the final SPE, should not be affected. Other than the unitless normalization, all entries are in MeV.

Parameter	Initial	Final
$\pi 0d_{5/2}$ SPE	-17.29	-18.43
$\pi 0d_{3/2}$ SPE	-9.08	-10.94
$\pi 1s_{1/2}$ SPE	-13.49	-12.38
$\nu 0d_{3/2}$ SPE	-9.03	-7.87
$\nu 1s_{1/2}$ SPE	-10.04	-7.60
$\nu 0f_{7/2}$ SPE	-2.62	-2.71
$\nu 1p_{3/2}$ SPE	-0.40	-1.61
$\nu 1p_{1/2}$ SPE	-0.27	1.01
C_{pp}	0.00	0.515
C_{pn}	0.00	0.020
C_{nn}	0.00	0.288
C_3	0.00	-0.008
overall normalization	1.00	0.918

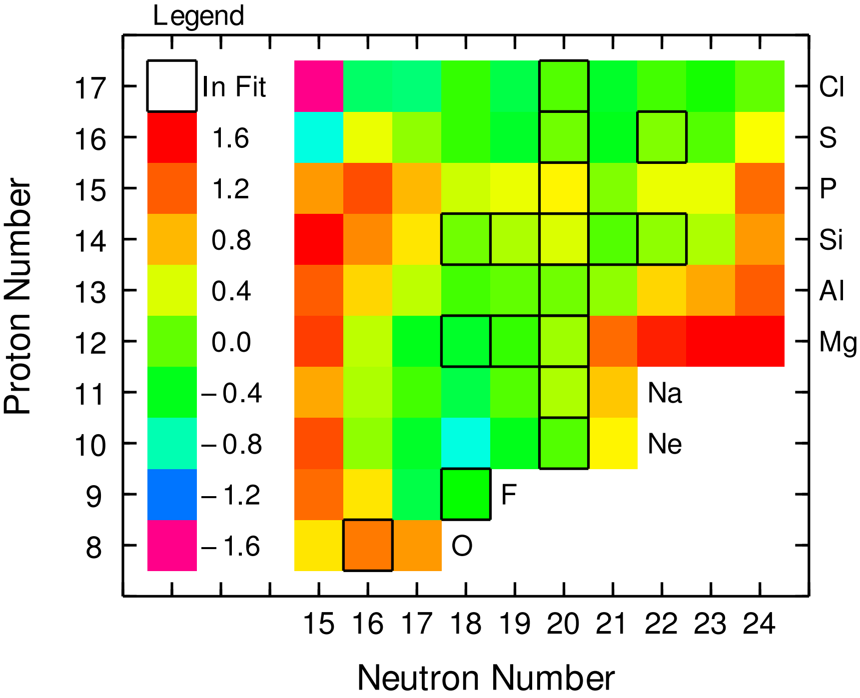

Figure 5.1: A plot of energy differences $E_{IOI} - E_{Exp.}$ in MeV calculated for one hundred nuclei in or near the island of inversion region. The black boxes denote nuclei which constrain the parameters in the IOI interaction. Experimental masses are taken from [81], excluding non-experimental masses estimated by extrapolation.

noted that the fit to data was performed with the older, published masses from [82]. Specifically, the binding energy of ^{24}O decreased by 521 keV from [82] to [81] such that $E_{IOI} - E_{Exp.} = 1.090$ MeV in Fig. 5.1, even though ^{24}O was included in the fit. As expected, the 370 keV rms deviation provides an approximate uncertainty for calculations in this model space, with the binding energy differences in Fig. 5.1 consistent within this uncertainty in most cases. The exceptions are the $N = 15$ and some $N = 16$ isotones, suggesting that excitations from the $0d_{5/2}$ orbit are essential for the description of these nuclei, and the magnesium isotopes ($Z = 12$). Standard and inverted configurations coexist for the magnesium chain near $N = 20$. It is unclear why the $N \geq 21$ isotopes are not reproduced, considering that the sodium and aluminum isotopes are reproduced to sufficient accuracy.

The rms deviation of 370 keV is sufficient for detailed studies in the island of inversion region. The capabilities of interactions derived with the Hybrid Renormalization Procedure and the structure of nuclei near the island of inversion can be explored by studying local trends, level schemes of specific nuclei, and reactions of particular interest.

5.1.1 Systematic Trends

The discussion in Chapter 4 led to the parameterization of single particle energies. A comparison of SPE in the model space is depicted in Fig. 5.2. The uncorrelated single particle energies obtained from the Skx and Skxtb interactions for the unstable ^{34}Si nucleus display the effect of the tensor interaction. The contribution from the tensor force can be larger than one MeV, as seen from the proton and neutron $0d_{3/2}$ orbits. As stated in Section 4.4, the one-nucleon separation energies, which are better representations of ESPE with SR-EDF methods, do not vary as much as the uncorrelated SPE in the equal filling approximation. The contribution of the tensor force might be smaller than evident from Fig. 5.2 as a result. The uncorrelated Skyrme SPE significantly deviate from the lowest experimental states. The IOI uncorrelated

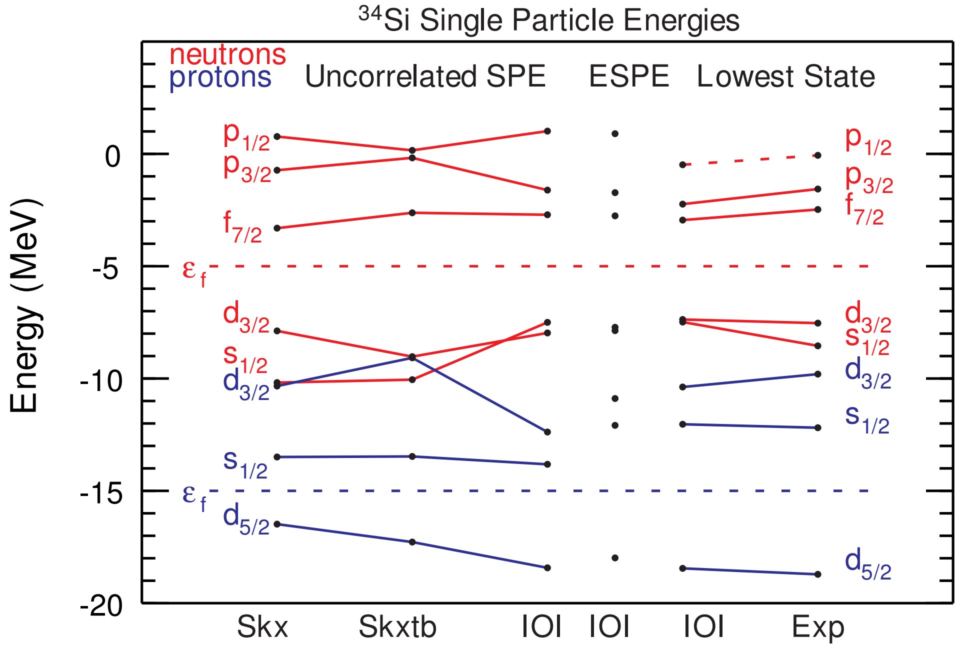

Figure 5.2: Single particle energies for ^{34}Si evaluated with different methods as described in Section 4.1. On the right, the lowest state approximation is compared for experiment and for calculations with the IOI interaction. On the left, uncorrelated SPE are shown as determined from the Skx and Skxtb interactions and the IOI interaction, as previously presented in Table 5.1. In the middle, the centroid or effective SPE of Eq. 4.3 is determined for the IOI interaction by including at least 99% of the strength of each orbit. The Fermi energy ϵ_f for ^{34}Si is represented by a dotted line for neutron orbits (red) and proton orbits (blue).

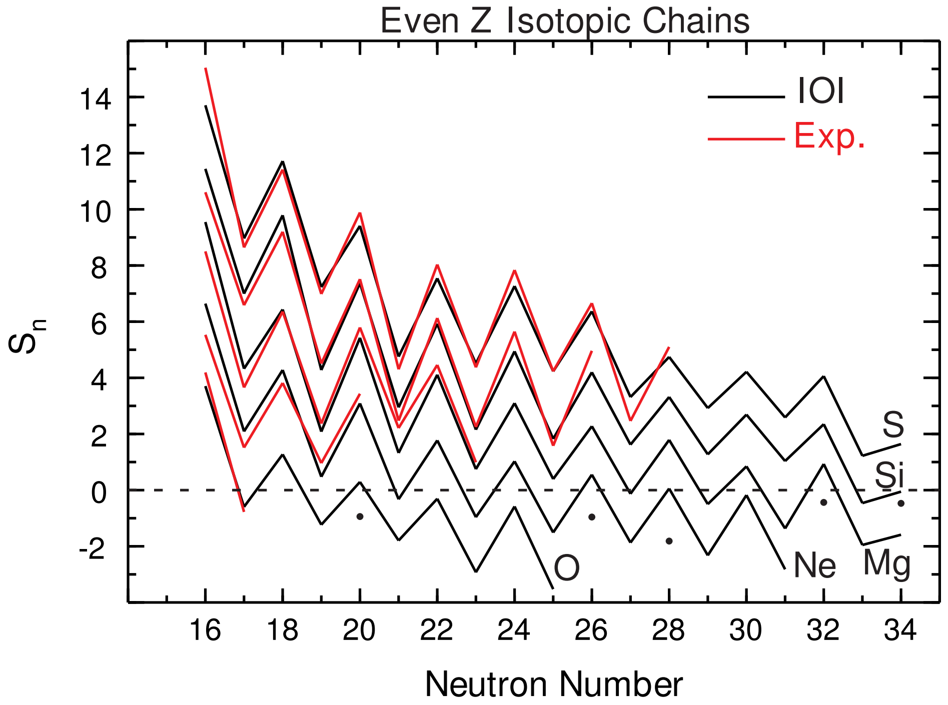

Figure 5.3: Neutron separation energy vs. neutron number for the isotopic chains with an even number of protons for both experimental data [81] and calculations with the IOI interaction. Non-experimental masses estimated by extrapolation and experimental masses with uncertainties greater than or equal to the rms deviation of the IOI interaction are excluded from the plot. The value of the two-neutron separation energy S_{2n} for unbound nuclei is represented by a black dot.

SPE from the fitting procedure are in much better agreement with the experimental states, which are not the effective SPE but are good approximations of single particle states for ^{34}Si. As mentioned in Chapter 4, microscopic energy density functionals which focus on reproducing single particle properties should improve upon the Skyrme SPE, providing values consistently close to experiment. Until then, the experimental states or parameterized SPE are preferred. The lowest states with the IOI interaction are in good agreement with experiment, and the amount of fragmentation can be inferred from the shift between the lowest state and ESPE for the IOI results. Only the $p_{1/2}$ orbit has significant fragmentation, implying that ^{34}Si exhibits the behavior of a magic nucleus.

The neutron dripline can only be reached for the lightest isotopes with current

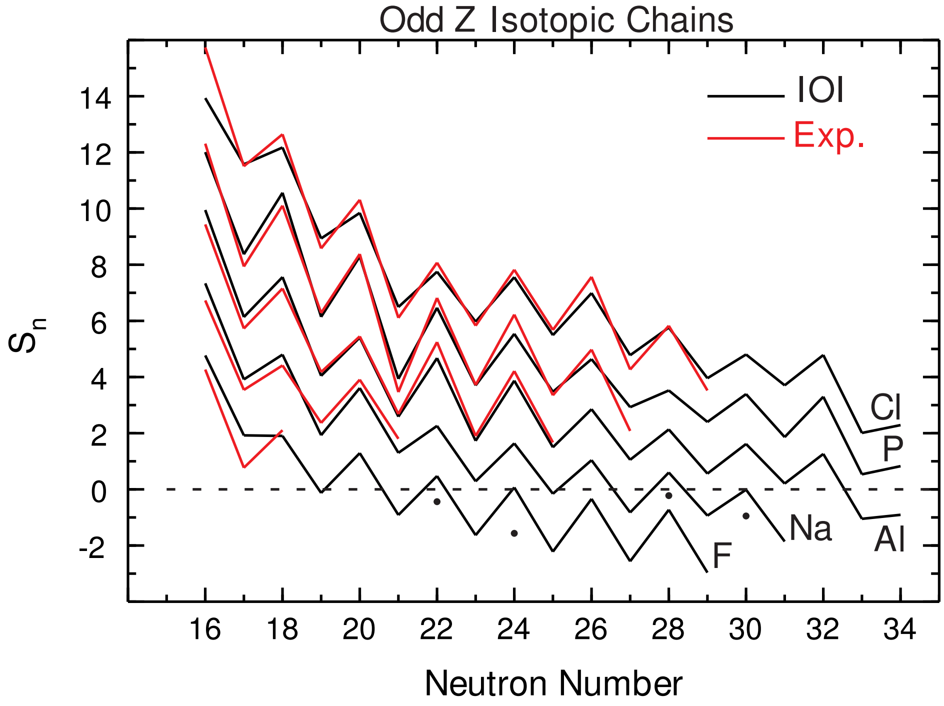

Figure 5.4: Neutron separation energy vs. neutron number for the isotopic chains with an odd number of protons for both experimental data [81] and calculations with the IOI interaction. Non-experimental masses estimated by extrapolation and experimental masses with uncertainties greater than or equal to the rms deviation of the IOI interaction are excluded from the plot.The value of the two-neutron separation energy S_{2n} for unbound nuclei is represented by a black dot.

experimental facilities, and has therefore only been established with certainty up to $Z = 8$. The neutron separation energy $S_n(^{A}Z) = BE(^{A}Z) - BE(^{A-1}Z)$ becomes negative at the first unbound nucleus. The odd-even behavior of the separation energy is prevalent due to the pairing interaction in nuclear physics. The separation energy is plotted as a function of neutron number for the ten isotopic chains in Figs. 5.3 and 5.4. The isotopic chains with an even number of protons are displayed in Fig. 5.3, and the agreement between experiment and calculations with the IOI interaction is excellent. For the oxygen isotopes, the binding energies for $N \geq 18$ are determined by an extrapolation from nearby masses and suggest that ^{24}O resides on the neutron dripline. Even though the theoretical S_n is positive for ^{28}O, albeit by less than the rms deviation, ^{28}O is not bound. The two-neutron separation energy S_{2n} is negative, such that the ground state decays by two-neutron emission to ^{26}O. For ^{26}O, however, the IOI interaction predicts a bound state since both S_n and S_{2n} are positive, with values 1.27 MeV and 0.68 MeV respectively. The experimental values from the extrapolated masses are 0.28 MeV and -0.50 MeV, and experimental evidence suggests that ^{26}O is unbound [83], [84]. Although ^{24}O is included in the fit to constrain the monopole terms for the lightest isotopes in the model space, the single particle energies are fit to data around ^{34}Si. The neutron $0d_{3/2}$ SPE is 6.3 MeV higher than the $1s_{1/2}$ SPE at ^{22}O with Skxtb, leading to the shell gap at $N = 16$ that is reflected in the stability of ^{24}O relative to its neighbors. However, for ^{34}Si, the $0d_{3/2}$ SPE is only one MeV higher in energy than the $1s_{1/2}$ SPE. The neutron separation energy of the oxygen isotopes, and therefore the neutron dripline, may not be reproduced with the ^{34}Si SPE. The evolution of SPE for calculations away from the nuclei in the fit will be discussed in Section 5.2. Another possibility, presented by Otsuka et al. [75], requires three-body forces for the accurate description of the neutron dripline for oxygen isotopes.

Another feature of Fig. 5.3 that is not reproduced in the calculation is the behavior of the $N = 21$ isotones. In the calculation, the spacing between the five nuclei is relatively large and consistent with the behavior throughout the rest of the model space. However, the experimental S_n for ^{33}Mg and ^{35}Si are nearly identical. Both nuclei have less than 50 keV uncertainty in their binding energies, but a remeasurement of both masses, or at least ^{33}Mg, is recommended. The effect is not reproduced by the IOI interaction but is interesting for future study.

The calculated dripline can be read off from the plot, where the last bound nucleus is ^{26}O, ^{34}Ne, ^{44}Mg, and ^{46}Si. All sulfur nuclei in the model space are bound, terminating at the closure of the $1p_{1/2}$ orbit at $N = 34$ for ^{50}S. The excluded $0f_{5/2}$ orbit may be important as the $N = 34$ subshell closure is approached.

The isotopic chains with an odd number of protons are displayed in Fig. 5.4. The agreement between experiment and theory is not quite as good as in Fig. 5.3, but the trends are still reproduced. The fluorine isotopic chain has been measured up to $N = 22$. The odd-odd isotopes are unbound starting with ^{28}F, but ^{31}F, the most neutron-rich isotope observed to date, is bound with respect to one and two neutron decay [85]. The theoretical predictions with the IOI interaction reproduce the experimental trend for the neutron separation energy, with only $N = 17$ deviating significantly. The binding energy of ^{26}F agrees with experiment within 120 keV, but ^{25}F and ^{24}F are underbound by 0.73 MeV and 1.14 MeV, respectively. Excitations from the $0d_{5/2}$ orbit are likely the cause, which do not affect the predictions for the more neutron-rich isotopes. The neutron dripline for the fluorine isotopes has not been determined experimentally, but the particle stability of ^{31}F has been identified [85]. The ground state of ^{31}F is unbound by two-neutron emission in the calculation with the IOI interaction, on the order of the rms deviation. The next odd-even fluorine isotope, ^{33}F, has a neutron separation energy of 70 keV and a two-neutron separation energy of -1.57 MeV with the IOI interaction. The ground state is unbound, and therefore the observed ^{31}F nucleus is predicted to reside at the neutron dripline. The dripline is not reached in this model space for the chlorine and phosphorus isotopes, but occurs at ^{37}Na and ^{45}Al. In addition to the caution as $N = 34$ is approached, the dripline assignment is tentative since ^{39}Na is unbound to two-neutron emission

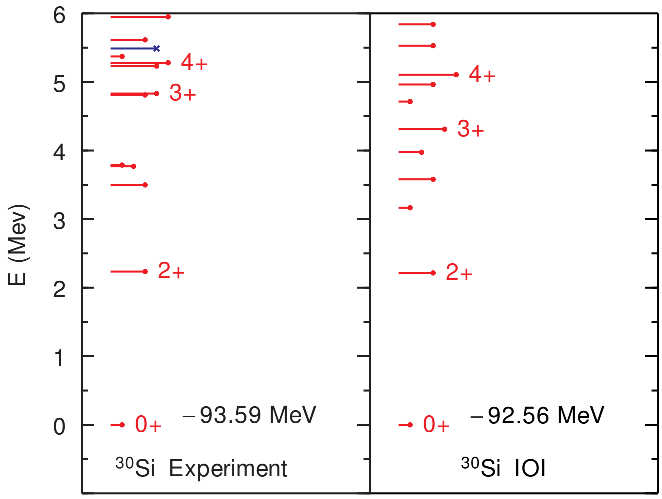

Figure 5.5: Comparison of experimental and theoretical level schemes for ^{30}Si up to 6 MeV. See the caption to Fig. 2.1 for further explanation.

by less than the rms deviation.

5.1.2 Level Schemes of Representative Nuclei

To present the predictive power of the IOI interaction, level schemes of representative nuclei in the model space will be compared to experimental data.

While ^{22}O is the target of the Hybrid Renormalization Procedure for the reasons discussed at the beginning of Section 5.1, the single particle energies are fit to states near ^{34}Si in order to better approximate their properties in the island of inversion. Relative to ^{34}Si, the valley of stability can be reached via the removal of four neutrons or by the addition of two protons. Since states in ^{36}S were included in the fit, the stable isotope ^{30}Si provides a comparison of experimental and theoretical level schemes in Fig. 5.5. The IOI interaction underbinds ^{30}Si by 1.03 MeV, which again can be attributed to the missing excitations from the $0d_{5/2}$ orbit. The excitation energy is consistent within the rms deviation for most states, and the level density is similar up to five MeV. The experimental level density is greater at higher energies, with a negative parity state at 5.5 MeV. The first negative parity state occurs at 7.8 MeV

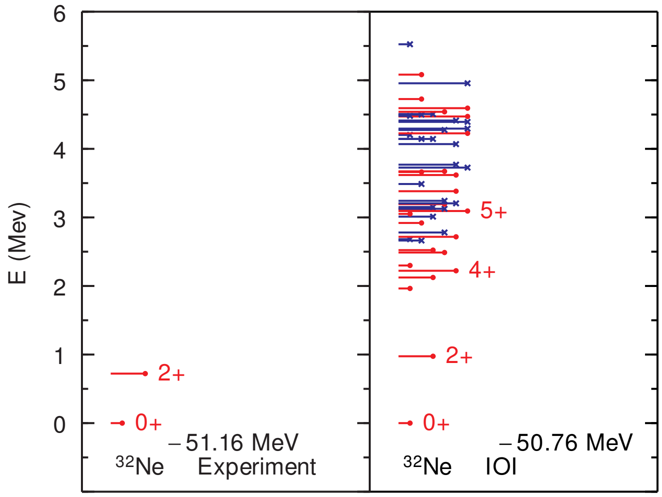

Figure 5.6: Comparison of experimental and theoretical level schemes for ^{32}Ne up to 6 MeV. Four states of each J^{π} are included in the figure. See the caption to Fig. 2.1 for further explanation.

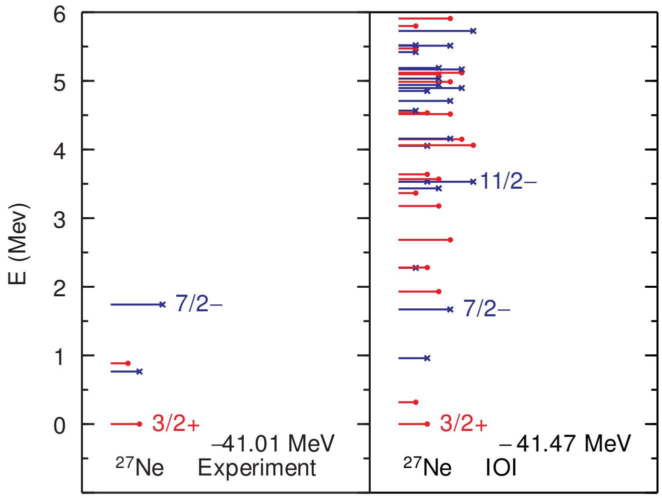

Figure 5.7: Comparison of experimental and theoretical level schemes for ^{27}Ne up to 6 MeV. Experimental data from [86] is included in addition to the ENSDF database. Four states of each J^{π} are included in the figure. See the caption to Fig. 2.1 for further explanation.

with the IOI interaction, suggesting that excitations of the ^{22}O vacuum must be included to reproduce states above 5 MeV.

If four protons are removed from ^{34}Si instead of four neutrons, the ^{30}Ne nucleus, which lies in the island of inversion region, is reached. However, the 0^+, 2^+, and 4^+ states in ^{30}Ne, i.e. all currently known states, were included in the fit. Therefore, the experimental and theoretical level schemes of ^{32}Ne, including an additional two neutrons, are compared in Fig. 5.6. The binding energy for theory and experiment differ by approximately the rms deviation of the fit. Only the ground state and first excited state are known, which are the only bound states with the IOI interaction. The unbound states have a high level density with the 4^+ state of primary interest for comparison to the known states in ^{30}Ne, occurring 450 (437) keV above the theoretical (experimental) neutron separation barrier. On the other side of the $N = 20$ shell closure, ^{27}Ne is shown in Fig. 5.7. Only the ground state is included in the ENSDF database [53], but three excited states have recently been detected experimentally. The negative parity states correspond to single particle excitations into the pf shell. Brown et al. [86] report that the gap between the sd and pf neutron orbits is reduced since calculations with the WBP interaction, including the sd and pf orbits, are unable to reproduce experiment. They conclude that "it would be interesting to develop a new shell model interaction that would succeed in reducing the effective gap between the $0d_{3/2}$ orbital and the $1p - 0f$ shell in a natural way, without the need for ad-hoc changes." The IOI interaction does not require any modification to reproduce nuclei throughout the island of inversion region. The theoretical binding energy is in reasonable agreement with experiment, and the level scheme is reproduced. The $3/2^-$ and $1/2^+$ states are inverted in the theoretical calculation, but are only separated by 120 keV experimentally. The energies of the negative parity states provide insight into the effective gap between the $0d_{3/2}$ orbital and the pf shell, such that the IOI interaction reasonably reproduces the gap.

Experimental evidence places ^{31}Mg [80] and ^{33}Na [87] in the island of inversion.

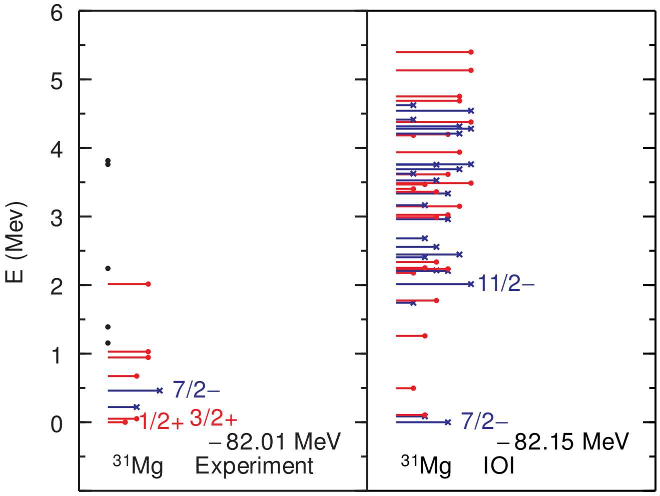

Figure 5.8: Comparison of experimental and theoretical level schemes for ^{31}Mg up to 6 MeV. The lowest four states are included in the fit to data for the IOI interaction. Experimental data from [80] is included in addition to the ENSDF database. The angular momentum is unassigned for the state at 1.15 MeV since the two sources have inconsistent values. Four states of each J^{π} are included in the figure. See the caption to Fig. 2.1 for further explanation.

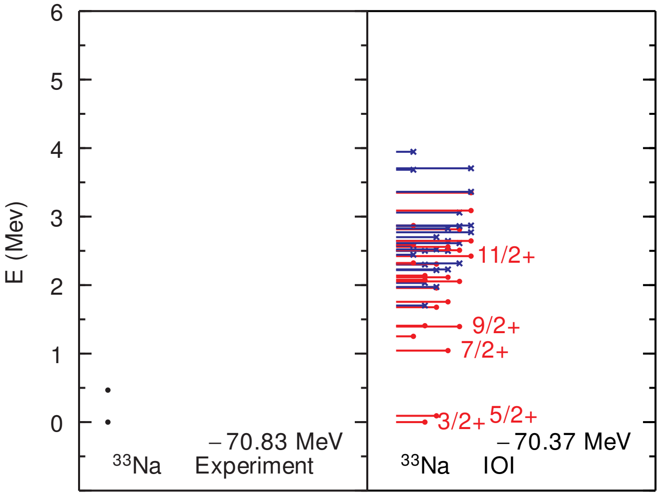

Figure 5.9: Comparison of experimental and theoretical level schemes for ^{33}Na up to 6 MeV. Experimental data from [87] is included in addition to the ENSDF database. Four states of each J^{π} are included in the figure. See the caption to Fig. 2.1 for further explanation.

The theoretical binding energies are in good agreement with experiment, including the rms deviation. The experimental level density for ^{31}Mg in Fig. 5.8 is higher than predicted at low energy, and the ground state spin is not reproduced in the calculation with the IOI interaction. This $1/2^+$ ground state has three *sd* neutron holes [80], and therefore two neutrons occupy the *pf* shell. The theoretical wavefunction, which is calculated in the harmonic oscillator basis in the CI calculation, reproduces this two-particle three-hole ($2p3h$) behavior for the $1/2^+$ state from a $2\hbar\omega$ excitation as discussed in Section 2.8. The absolute energy of the $1/2^+$ state is underbound by 360 keV, which is within the rms deviation of the fit. However, coupled with the overbinding of the $7/2^-$ $1p2h$ state and a high density of states at low energy, the $1/2^+$ state occurs theoretically as the third excited state instead of the ground state. Even though the ground state resides in the island of inversion in both cases, the $3/2^+$ state is a $1h$ state and occurs at an experimental (theoretical) excitation energy of 51 (106) keV. The boundaries of the island of inversion region, as determined in Section 5.1.3, must be treated with caution due to the coexistence of standard and inverted configurations below the rms deviation of 370 keV.

Doornenbal et al. [87] have identified the ground state and first excited state in the island of inversion nucleus ^{33}Na, and argue from systematics in the sodium isotopic chain that the states should have $3/2^+$ and $5/2^+$ in some order. They also argue that the second excited state should be above 700 keV in excitation energy. The predictions with the IOI interaction display this behavior, with the $3/2^+$ state as the ground state. Because the $5/2^+$ excited state at 92 keV has an excitation energy smaller than the rms deviation, a definitive statement about the spin of the ground state cannot be made.

One issue that arises in the comparison of level schemes in the island of inversion is the dearth of experimental data; the few excited states that have been measured rarely have assigned spin and parity. The five nuclei described in this section have excited states for comparison to calculations and are representative of the behavior

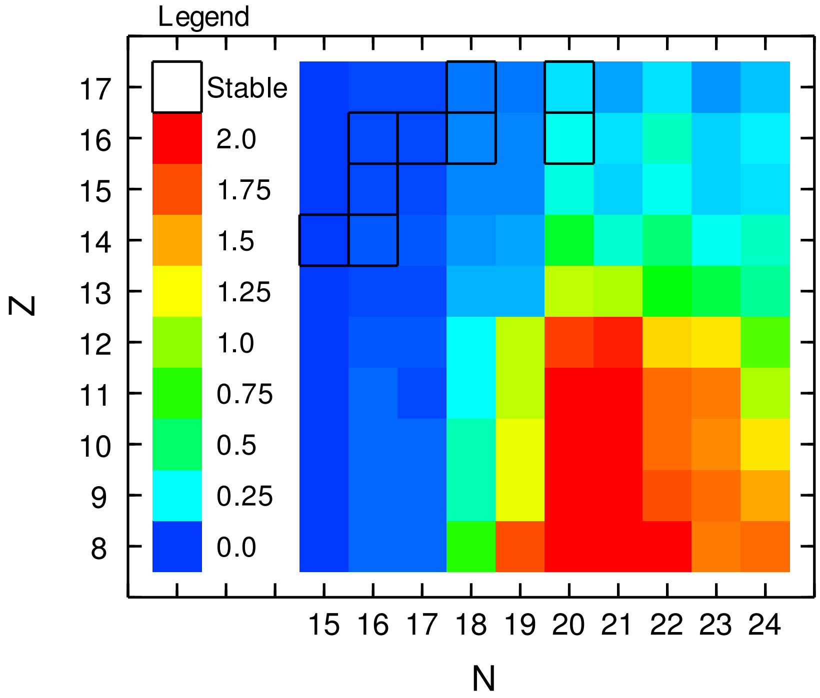

Figure 5.10: A plot of $\hbar\omega$ excitations for one hundred nuclei, as determined from the ground state wavefunctions calculated with the IOI interaction. The wavefunctions are composed of linear combinations of configurations, each with an integral number of excitations as defined in Section 2.8. The normalization condition $\langle\Psi \mid \Psi\rangle = 1$ leads to non-integral values for each nucleus. The island of inversion is composed of nuclei with more than 1.00 $\hbar\omega$ excitation. Stable isotopes are outlined in black.

of level schemes throughout the model space. The comparison between experimental data and calculations with the IOI interaction for all 100 nuclei can be accessed at [88].

5.1.3 Ground State Occupations

The island of inversion is composed of the nuclei near ^{31}Na where pf orbits are preferentially filled before the lower-energy sd shell is occupied completely. Because the physical states and calculations with a diagonalization of a model space interaction like the IOI interaction are composed of a linear combination of many configurations, the occupations of the neutron orbits are not integral. As a result, the boundaries of the island of inversion are dependent on a minimum value of excited neutrons. An excitation of $1\hbar\omega$ from the sd shell to the pf shell, as defined in Section 2.8, is necessary for a single configuration to be considered inverted. The cutoff on the average excitation in $\hbar\omega$ is selected as 1.00 to determine the boundaries of the island of inversion. For $N \leq 20$, the occupation of the pf orbitals is identical to the $\hbar\omega$ excitation for a ground state wavefunction. This does not provide a perfect description, as can be seen from the ground state of ^{33}Al. The primary component of the wavefunction corresponds to the standard filling of orbitals, resulting in a completely filled sd shell at $N = 20$. This component contributes 47% of the total probability density of the neutron occupation, but the other 53% is composed of hundreds of configurations, primarily with $2p2h$ excitations into the pf shell. The ground state of ^{33}Al has an average occupation of 1.10 pf neutrons, or an average excitation of 1.10 $\hbar\omega$. Since this value exceeds the minimum value of 1.00 $\hbar\omega$ excitation, ^{33}Al would be considered inside the island of inversion even though the primary component of the ground state has $0p0h$ structure. Experimental evidence has confirmed that the ^{33}Al ground state exhibits mixed $0p0h - 2p2h$ structure for the neutron configurations, such that Tripathi et al. consider ^{33}Al inside the island of inversion region [89]. As the presence of standard and inverted states within the rms deviation of the ground state demanded in Section 5.1.2, the minimum value of 1.00 $\hbar\omega$ excitation requires caution. Further investigation of the wavefunction for each individual isotope of interest is necessary if definitive statements about the boundary of the island of inversion are desired.

An approximate theoretical boundary is displayed graphically in Fig. 5.10, which plots the number of $\hbar\omega$ excitations as a function of proton and neutron number. While ^{34}Si is partially composed of configurations with $2\hbar\omega$, no isotopes with $Z \geq 14$ lie in the island of inversion region. The valley of stability, marked by the black boxes, has almost no contribution from configurations with an inversion in the occupation of neutron orbits. Similarly, all nuclei with $N \leq 18$ exhibit the standard occupation structure. While the $N = 24$ isotones ^{32}O and ^{33}F have nearly two holes in the sd neutron orbits, neither of these isotopes are bound, as seen in Figs. 5.3 and 5.4. In fact, no bound states in oxygen exhibit inversion. The results in Fig. 5.10 suggest that the island of inversion extends further than the $N = 22$ boundary that has been the limit of experimental investigation thus far, and that nearly all nuclei with $Z \leq 13$ and $N \geq 19$ exhibit inversion. An evaluation of the pf occupation in the fluorine isotopes with $N \geq 19$ and for magnesium, sodium, and neon isotopes with $N \geq 22$ would be interesting with rare isotope facilities.

5.1.4 β decay

The primary mode of decay for the calculated ground states occurs via β emission. The nuclei near the island of inversion approach the valley of stability through β^- decay, where a neutron is converted into a proton, an electron, and an antineutrino. The Q-value of the decay is determined by the difference in binding energy between the daughter and parent nuclei, in addition to 782 keV for the difference in mass between the neutron and the hydrogen atom. Because the reaction depends on the Q-value to the fifth power, experimental binding energies will be employed instead of the values determined with the IOI interaction. The partial half-life for the decay to a particular state in the daughter is given by

$$ft_{1/2} = \frac{C}{B(F) + (g_A/g_V)^2 B(GT)}, \tag{5.1}$$

where f is a phase-space factor that can be calculated, C is a constant that has been determined experimentally as $C = 6177$, and $B(F)$ and $B(GT)$ are Fermi and Gamow-Teller transitions, respectively. A complete description of β decay is contained in [12]. At the quark level, $g_A = -g_V$, but the value is generally modified for nuclear structure calculations to reproduce the decay of the neutron. From Wilkinson, $\mid g_A/g_V \mid = 1.261(8)$ [90].

The decays of exotic nuclei around $N = 20$ are at the limits of experimental investigation with rare isotope beams. In order to optimize the comparison between theoretical and experimental results, the decay of a more stable nucleus around $N =$

20 with known transition strengths must be calculated. As ^{35}P fulfills the requirements and has been previously studied with *sd* shell interactions [91], it will provide a test case of the IOI interaction.

Experimentally, the transition to the ground state of ^{35}P cannot be measured, but only inferred. An upper limit of 9% on the branching ratio to the ground state is included in the ENSDF database [53]. The branching ratios of the two measured transitions, to the $1/2^+$ state at 1.57 MeV and to the $3/2^+$ state at 2.94 MeV, are 99.5% and 0.5%, respectively [53]. The calculation with the standard USDB interaction for the β^- decay of the $1/2^+$ ground state of ^{35}P occurs to the lowest three states in ^{35}S. The $1/2^+$ state in ^{35}S at 1.68 MeV is the primary state populated, with a branching ratio of 90.7%. The $3/2^+$ ground state of ^{35}S has a branching ratio of 7.8%, and the remaining strength populates the $3/2^+$ excited state at 2.80 MeV. The standard interaction produces results that are in reasonable agreement with the experimental transitions, especially with the unknown ground-state to ground-state transition. The half-life of ^{35}P, as calculated with USDB, is 62.9 s, in comparison to the experimental value of 47.3(7) s. As the results in Section 2.2 have shown, the Hybrid Renormalization Procedure produces interactions which are comparable to the best Hamiltonians derived empirically. Although the model spaces are different for the IOI and USDB interactions, calculations with the two interactions might be naively expected to produce similar results.

The calculations with the IOI interaction populate only the lowest two states, with branching ratios of 18.9% and 81.1% to the $3/2^+$ ground state and $1/2^+$ excited state at 1.46 MeV in ^{35}S. The higher branching ratio to the ground state is important for the evaluation of the half-life of ^{35}P, resulting in a much shorter half-life of 18.3s, compared to the USDB and experimental results.

The empirical *sd* shell interactions require a quenching factor to reproduce experiment, implemented through a reduction of 30% of the ratio of the axial-vector to vector coupling constants g_A/g_V. In other words, β decays in the *sd* shell require approximately the quark value of g_A/g_V. This reduction, which is necessary to approximately reproduce β decays throughout the *sd* shell with the USDB interaction, was included for the calculations with both the USDB and IOI interactions above to incorporate effects of higher-order nucleon configuration mixing and from the presence of the delta isobar in the nuclear wavefunctions [92]. However, the 30% reduction of g_A/g_V with the IOI interaction results in too short of a lifetime. To approximately reproduce the experimental lifetime, the necessary reduction factor must be larger, with additional quenching due to the exclusion of the $0d_{5/2}$ from the model space. Transition strength at higher energies in ^{35}S, to isobaric analogue states of ^{35}P, are missing without the entire *sd* neutron shell. The reduction factor is phenomenologically determined for the IOI interaction by approximately reproducing the half-life of ^{35}P. With a reduction factor of 55%, the calculated half-life is 45.9 s, in reasonable agreement with the experimental value of 47.3(7) s. This reduction factor is necessary for all calculations with the IOI interaction and will be applied to the β^- decay of ^{33}Mg.

The decay of ^{33}Mg was studied by Tripathi et al. [89] and is of particular interest because of conflicting experimental evidence regarding the parity of the ground state. From the β decay, the ground state has been identified as $3/2^+$. A measurement of ^{33}Mg combining laser spectroscopy with nuclear magnetic resonance techniques unambiguously identified the ground state spin as $J = 3/2$, while assigning a negative parity from a measurement of the magnetic dipole moment [93]. Theoretically, the level scheme of ^{33}Mg, and particularly the β decay transitions and magnetic moments of the $3/2^+$ and $3/2^-$ states, can be compared to the experimental data to provide insight into the inconsistent assignment of the ground state parity.

The level schemes for ^{33}Mg and the daughter of its β^- decay, ^{33}Al, are included in Figs. 5.11 and 5.12, respectively. The spins and parities of the known levels are mostly unassigned, including the ground state of ^{33}Mg since the values from available experimental data are inconsistent. In the calculation, the ground state is $3/2^-$, but

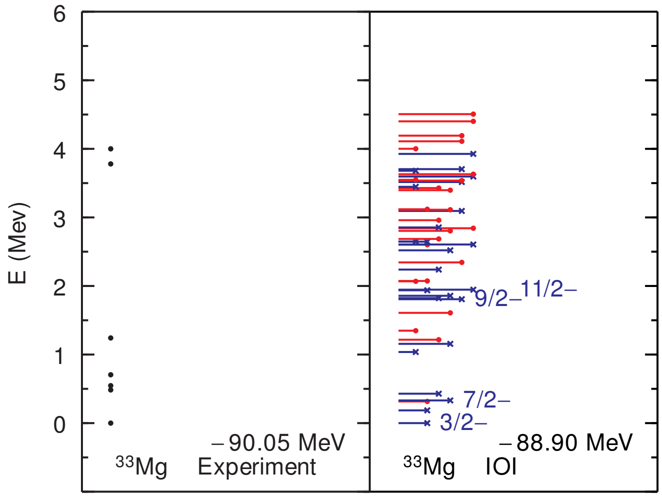

Figure 5.11: Comparison of experimental and theoretical level schemes for ^{33}Mg up to 6 MeV. Four states of each J^π are included in the figure. See the caption to Fig. 2.1 for further explanation.

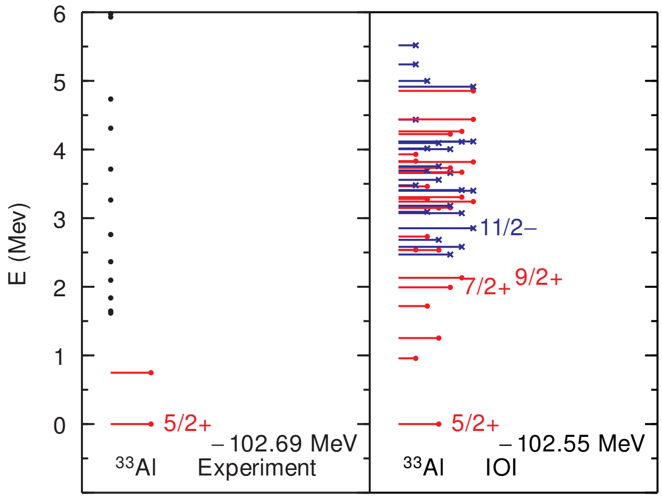

Figure 5.12: Comparison of experimental and theoretical level schemes for ^{33}Al up to 6 MeV. Experimental data from [89] is included in addition to the ENSDF database. Four states of each J^π are included in the figure. See the caption to Fig. 2.1 for further explanation.

four states occur within the rms deviation of the fit. As a result, it is necessary to consider the lowest four states in the calculation. The $7/2^-$ state at 330 keV is ruled out by the identification of $J = 3/2$ in [93], but the remaining three states can all reasonably be expected to match the experimental ground state. To distinguish between the theoretical $3/2^-$ ground state, the excited $3/2^-$ state at 186 keV, and the $3/2^+$ state at 316 keV, the β^- decay and magnetic moment of each state have been calculated with the IOI interaction. It is unusual for two states with the same J^π to occur at such low energy, especially with similar wavefunctions as in this case. The main component of each wavefunction ($\approx 45\%$) is $3p3h$ in nature, with two neutron holes in the $0d_{3/2}$ orbit, a pair of $0f_{7/2}$ neutrons and an unpaired neutron in the $1p_{3/2}$ orbit to produce $J^\pi = 3/2^-$.

Tripathi et al. measure the β^- decay of ^{33}Mg from γ transitions in the ^{33}Al daughter [89]. As a result, the Gamow-Teller strength above the neutron separation energy at 5.54(11) MeV was not measured. The branch to the ground state is also not measured directly, as it does not γ decay, but was inferred from the remaining strength after accounting for neutron emission. The half-life of ^{33}Mg was determined from a fit to the decay curve, with $t_{1/2} = 89(1)$ ms [89]. With the IOI interaction, the β decay of the three lowest states in ^{33}Mg and the γ decay scheme of ^{33}Al were calculated with NUSHELLX to compare to the experimental results. Since the ground state of ^{33}Mg has $J = 3/2$, the β decay can only occur to states in ^{33}Al with $J = 1/2, 3/2, 5/2$.

As can be seen in Fig. 5.12, the negative parity states begin at 2.68 MeV in ^{33}Al. Conservation of parity in the Gamow-Teller decay is a theoretical constraint, such that both $3/2^-$ states in ^{33}Mg decay only to negative parity states in ^{33}Al. The majority of the strength populates states above five MeV for both $3/2^-$ states. A significant neutron emission probability P_n is calculated, with $P_n = 25.8\%$ and $P_n = 49.6\%$ for the ground state and excited $3/2^-$ state respectively, in comparison to the experimental value of $P_n = 14(2)\%$ [89]. Furthermore, the respective β decay half-lives are 444 ms and 580 ms, in comparison to 89(1) ms. The $3/2^+$ state at 316

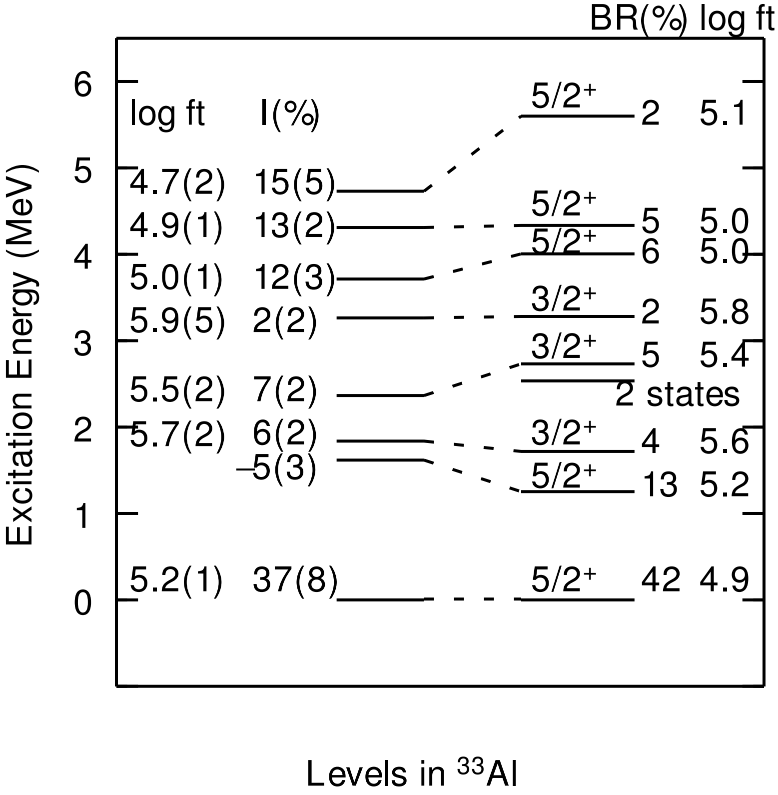

Figure 5.13: Comparison of experimental and theoretical level schemes for ^{33}Al as determined from the β^- decay of the lowest $3/2^+$ state in ^{33}Mg. The experimental levels and properties are taken from Fig. 3 of [89]. All theoretical states below the neutron separation energy with a beta decay branching ratio of at least 2% are plotted. The "2 states" at 2.54 MeV are: (i) a $5/2^+$ state with a branching ratio of 3% and a log ft value of 5.5, and (ii) a $1/2^+$ state with a branching ratio of 4% and a log ft value of 5.5.

keV has a half-life of 49 ms, with $P_n = 7.4\%$ and a branching ratio of 42.5% to the ground state, in comparison to the inferred branch of 37(8)% experimentally. The reduction in the neutron emission probability compared to experiment is due to the missing strength at higher energies from the exclusion of the $d_{5/2}$ neutron orbit.

Figure 5.13 compares the decay schemes of the $3/2^+$ state in ^{33}Mg for experiment and theory by analyzing the states in ^{33}Al. Although it is not shown graphically, the gamma decay observed in the ^{33}Al states has been compared to the theoretical E2 and M1 transitions to aid in the comparison of levels. For instance, there are three states in the theoretical decay that could match the 2.37 MeV experimental state. Neither of the two states at 2.54 MeV decays to the ground state, while the only measured decay from the experimental state populates the ground state. The theoretical $3/2^+$ state at 2.73 MeV has a 93% branch to the ground state in the gamma decay, and the remaining 7% decays to a 0.96 MeV state that is not populated by β decay, but could correspond to the 0.76 MeV state in the ENSDF database. Besides the two states at 2.54 MeV, the remaining states can be matched to the data. The experimental state at 1.62 MeV has a negative intensity because it is populated through gamma decay of the higher states. Theoretically, this state is assigned to the $5/2^+$ state at 1.26 MeV, even though it has a relatively large branching ratio, because of its population in the de-excitation of the higher-energy states. The highest three theoretical states in Fig. 5.13 have smaller branching ratios than expected from the intensity of measured γ transitions. In particular, the theoretical transition to the state at 5.60 MeV is much reduced, while the log ft value and theoretical energy are 2σ higher than experiment. The theoretical energy places the state right at the neutron decay threshold. The state is nevertheless matched to the experimental state at 4.73 MeV because two of the three γ transitions are reproduced, and because there are no other viable theoretical states. Again, the exclusion of the $d_{5/2}$ neutron orbit could contribute to the disagreement. The reproduction of the experimental data provides convincing evidence that the experiment by Tripathi et al. measured the decay of the $3/2^+$ state in ^{33}Mg. They assigned the ground state parity as positive based on the experimental results, and suggested that the magnetic moment could be negative if the $3/2^+$ state had a predominant $4p3h$ configuration. However, the theoretical wavefunction of the $3/2^+$ state is mainly $2p1h$ in nature.

The nuclear magnetic moment was measured as $\mu = -0.7456(5)\mu_N$, which led to an assigned ground state spin of $3/2^-$ [93]. For the $3/2^+$ state, which matches the β^- decay, the magnetic moment has the opposite parity with $\mu = 0.882\mu_N$. The $3/2^-$ states have the correct parity, with $\mu = -1.236\mu_N$ and $\mu = -0.815\mu_N$ for the ground state and excited state at 186 keV, respectively. The predominant configuration for both $3/2^-$ states has two neutron holes in the *sd* shell. The magnetic moment is in much better agreement with the excited $3/2^-$ state. The electric quadrupole moment has not been measured experimentally, but could be used to further differentiate between the states. The quadrupole moments for the three states are 3.96 (-3.48,13.69) e^2 fm^2 for the ground state ($3/2^-$ excited state, $3/2^+$ state). The comparatively large value of the $3/2^+$ state and the opposite sign of the $3/2^-$ states should aid in the identification of the ground state spin through a measurement of the ground state quadrupole moment. Based on the current status of experimental data, an isomer may be present with a lifetime similar to that of the ground state, which could have led to the inconsistent determination of the ground state parity.

The gamma decay from the $3/2^+$ to $3/2^-$ state, or vice versa, is strongly dependent on the energy difference between the states. Since all three states are within the rms deviation, no conclusions can be drawn regarding the gamma decay half-life. In the event that the energy difference is small, on the order of one keV, the beta decay half-life could be even shorter than the gamma decay. An upper limit of the half-life is therefore given by the beta decay half-lives for the three states, about half a second for each $3/2^-$ state and 49 ms for the $3/2^+$ state. The beta decay scheme and magnetic moment measurement have identified the ground state as $3/2^+$ and $3/2^-$, respectively, but either experiment could have measured the properties of an isomer. The theoretical calculation with the IOI interaction produces a $3/2^-$ ground state, but also excited $3/2^+$ and $3/2^-$ states within the rms deviation. The beta decay scheme of the $3/2^+$ state agrees well with the experimental decay, while the magnetic moment of the excited $3/2^-$ is in reasonable agreement with the experimental value. An experiment that can resolve the isomer from the ground state, even though the half-lives may be on the same order of magnitude, would be required to assign the ground state spin in ^{33}Mg.

Table 5.2: Comparison between experimental [86] and theoretical spectroscopic factors for states in ^{27}Ne.

J^{π}	$E_{Exp.}$	E_{IOI}	$C^2S_{Exp.}$	C^2S_{IOI}
$3/2^+$	0.000	0.000	0.42(22)	0.58
$3/2^-$	0.765	0.960	0.64(33)	0.63
$1/2^+$	0.885	0.318	0.17(14)	0.41
$7/2^-$	1.714	1.670	0.35(10)	0.46

5.1.5 ^{26}Ne(d,p)^{27}Ne

Although β^- decay is the primary mode of decay for ground states, other types of reactions are also of interest in the island of inversion region. Spectroscopic factors from transfer reactions, as defined in Section 4.1, are of particular interest as a probe of the evolution of shell structure, evaluated by the strength of single particle states. The level scheme of ^{27}Ne has already been shown in Fig. 5.7, including states obtained from the ^{26}Ne(d,p)^{27}Ne reaction [86]. The spectroscopic factors can be calculated directly with the IOI interaction through an overlap of the wavefunctions. Table 5.2 displays the experimental and theoretical results for excitation energies and spectroscopic factors of states in ^{27}Ne populated by the transfer reaction.

From the table, it can be seen that only the $1/2^+$ state is inconsistent in the comparison, once the rms deviation of 370 keV and the experimental uncertainty in the spectroscopic factors are taken into account. Short-range correlations are reduced for exotic nuclei, such that the global reduction factor between theory and experiment for spectroscopic factors [67] is not as pronounced for ^{27}Ne [94]. The other states rival the modified empirical interaction WBP-M, tuned by Brown et al. [86] specifically for ^{27}Ne. As seen in [86], the original WBP Hamiltonian derived by Warburton and Brown [95] does not reproduce the low-energy negative parity states, suggesting that the gap between the *sd* and *pf* neutron orbits is too large. With a more microscopic approach utilizing the Hybrid Renormalization Procedure, the shell structure evolves away from stability without fine-tuning. Even though the results are not consistent with experiment, the $1/2^+$ state is within a deviation of 2σ for both the energy and the spectroscopic factor. The overall agreement between experiment and calculations with the IOI interaction is satisfactory and is representative of the accuracy of structure information determined by reactions with exotic nuclei. To evaluate the description of reaction mechanisms, a more complicated reaction with recent experimental data is necessary.

5.1.6 ^{30}Mg(t,p)^{32}Mg

The coexistence of *sd* and *pf* neutron configurations in nuclei in the island of inversion region provides information regarding the stability of the $N = 20$ closure. The reaction code FRESCO [96] has been utilized to calculate the cross sections of the two-neutron transfer reaction ^{30}Mg(t,p)^{32}Mg and to evaluate the behavior of the $N = 20$ shell closure for the magnesium isotopes.

Figure 5.14 displays schematically the occupation of neutron orbits for the two-neutron transfer reaction, with the negligible contribution of the $1p_{1/2}$ orbit not included. The 0^+ ground state of ^{30}Mg, which lies outside the island of inversion as seen in Fig. 5.10, can be represented as two neutron holes in the $0d_{3/2}$ and $1s_{1/2}$ orbits. The two-nucleon transfer to 0^+ states in ^{32}Mg, assuming a direct transfer, requires two neutrons coupled to zero total angular momentum. In scenario A, *sd* orbits are populated in the transfer and the *sd* shell is filled. In scenario B, *pf* orbits are populated, which results in a $2p2h$ configuration in ^{32}Mg. As seen in Fig. 5.10, inverted configurations are necessary to describe the 0^+ ground state of ^{32}Mg, such that both scenarios must be included to properly describe the two-nucleon transfer reaction.

Global optical potentials from Perey and Perey [97] are used to describe the projectile-target and ejectile-remnant systems, as well as the core-core (^{30}Mg+p) interaction. Two-body coefficients of fractional parentage are determined from an overlap of the ^{30}Mg and ^{32}Mg wavefunctions with NUSHELLX [9]. The transfer mechanism is assumed to consist of one step, i.e. a simultaneous transfer of a di-neutron.

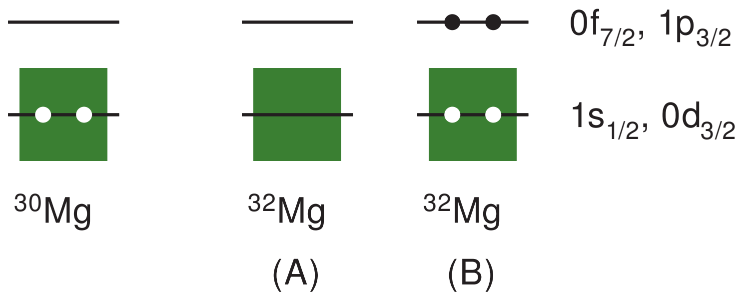

Figure 5.14: A schematic representation of the two-neutron transfer in the ^{30}Mg(t,p)^{32}Mg reaction. The ground state configuration of ^{30}Mg consists of two holes in the *sd* shell, with the small contribution of $2p4h$ configurations neglected. Two scenarios are possible for the transfer of a di-neutron: *sd* orbits are populated and the nominal $N = 20$ shell closure is filled (A), or *pf* orbits are populated, resulting in a $2p2h$ configuration for ^{32}Mg (B).

Sequential transfers of a single neutron should be suppressed due to the large negative Q-value of the ^{30}Mg(t,d)^{31}Mg reaction. The reaction calculations depend strongly on the Q-value; since the experimental binding energies are not reproduced by the IOI interaction within the rms deviation for all the states of interest, the input to FRESCO will include experimental energies.

In the simplest calculation, the USDB interaction operating in the *sd* model space can be used to calculate two-nucleon transfers from ^{30}Mg to ^{32}Mg. In this case, scenario A of Fig. 5.14 is the only possible reaction mechanism. The ground state of ^{32}Mg in the *sd* model space is missing correlations from the *pf* shell as described in Section 1.7 and displayed in Fig. 1.7. The 0_2^+ state occurs above nine MeV in excitation energy, since the protons are deeply bound for neutron-rich nuclei and neutron excitations are not possible. The reaction cross section for the ground state to ground state transition is 1.70 mb, in comparison to the experimental value of 10.5(7) mb [98]. The exclusion of *pf* orbits prevents an adequate description of the reaction process.

With the IOI interaction, which allows both scenarios of Fig. 5.14, the ground state to ground state transition has a reaction cross section of 9.69 mb, in good agreement with the experimental value. The average occupation of the pf orbits in the ground state is 1.79, with the primary configuration ($\approx 50\%$ of the total) composed of two neutron holes in the $0d_{3/2}$ orbit and two particles in the $0f_{7/2}$ orbit. The standard filling of neutron orbits, given by scenario A, represents only 16% of the ground state wavefunction. The same configuration, however, is the primary configuration in the 0_2^+ wavefunction, representing 64% of the wavefunction. The excitation energy of the 0_2^+ state is 2.19 MeV with the IOI interaction, while a recent experiment by Wimmer et al. [98] has identified the 0^+ excited state in ^{32}Mg at 1.06 MeV. With the experimental excitation energy, the reaction cross section is 0.21 mb. With the theoretical excitation energy, however, the reaction cross section is 1.32 mb. Since the shape coexisting 0_2^+ state at 1.06 MeV predominantly has a configuration with a fully-occupied sd shell, a comparable cross section to the USDB case might naively be expected. This result is obtained only with the theoretical excitation energy.

The mixing with the $2p2h$ configurations in the 0_2^+ state are important in the determination of the cross section. The inclusion of pf orbits can result in constructive or destructive interference in the calculation of the cross section. With the coefficients of fractional parentage from the IOI interaction, the sd and pf coefficients are in phase and cause destructive interference. A calculation with the same magnitude of the coefficients, but with the opposite phase for the sd coefficients, results in a 0.48 mb cross section with the experimental excitation energy. This value is still an order magnitude smaller than the experimental cross section of 6.5(5) mb [98], and smaller than the result with the USDB ground state, but emphasizes that all orbits contributing to the low-energy behavior of the nucleus must be included in the model space.

Wimmer et al. calculate a theoretical cross section for the excited state based on the ground state wavefunction of the USD interaction in the sd model space. The result is a factor of two smaller than measured [98], while a similar result here with the USDB interaction is a factor of 3.8 smaller than measured. The difference in effective interaction between USDB and USD affects the cross section on the 2% level. The optical potentials, coupling scheme, and other parameters of the reaction calculation significantly affect the results. Global optical potentials and a simplistic description of the two-nucleon transfer were approximations which could be improved upon in future work and are likely the cause for the deviation between these results and those from Wimmer et al. From the results obtained in this work, the reaction cross section to the ground state is in good agreement with experiment but the cross section to the excited 0^+ state is significantly reduced relative to experiment. The reaction calculation and the amount of mixing depend on the energy difference between the $0\hbar\omega$ and $2\hbar\omega$ configurations for ^{32}Mg. Since the excitation energy of the *sd*-like 0_2^+ state is over one MeV higher than experiment, the amount of mixing is likely reduced relative to the physical state. The similar experimental reaction cross sections to the ground state and excited 0^+ state, 10.5(7) and 6.5(5) mb respectively, suggest that the necessary mixing between $0\hbar\omega$ and $2\hbar\omega$ configurations is greater than calculated with the IOI interaction.

5.2 ^{42}Si

Another nucleus of interest for the Hybrid Renormalization Procedure is ^{42}Si, due to the evolution of the $N = 28$ shell closure away from stability. Bastin et al. [99] measured the 2^+ energy of ^{42}Si at 770(19) keV, indicating the disappearance of the shell closure as displayed in Fig. 1.9. Because ^{42}Si is outside of standard model spaces and has only recently been reproduced with the empirical SDPF-U interaction [48] discussed in Chapter 3, the HRP provides a more microscopic description which can be compared directly to experimental data. Again, the *sd* proton orbits are active, and the *sd* and *pf* neutron orbits could be of interest. As discussed in the beginning of Section 5.1, the matrix diagonalization restricts the number of neutron orbits. Two separate valence spaces will be employed, using the model space from the previous

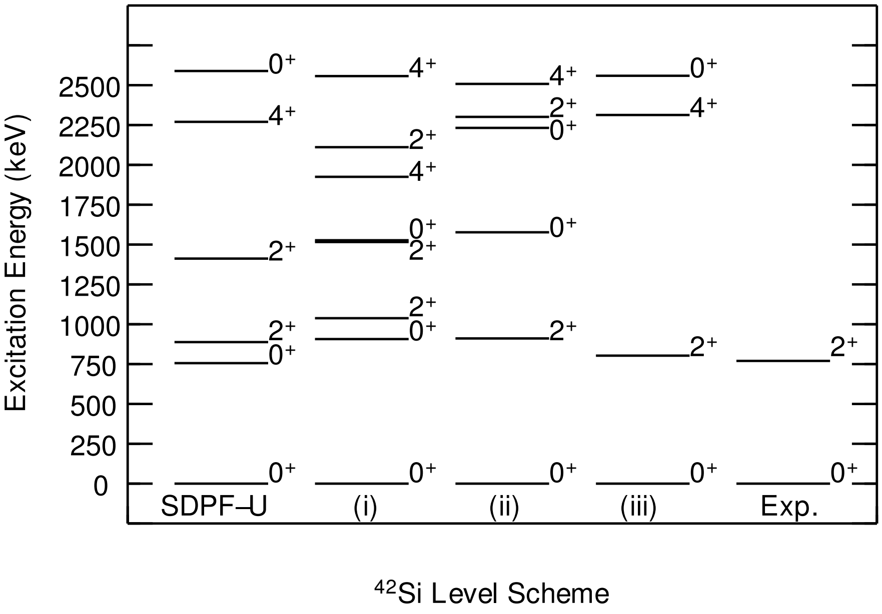

Figure 5.15: A comparison of level schemes for ^{42}Si from experiment, from the empirical SDPF-U interaction for $Z \leq 14$, and with three interactions derived from the HRP: the IOI interaction (i), the IOI interaction with SPE modified by Eq. 5.2 (ii), and an interaction in the *sdpf* model space with ^{42}Si as the target (iii).

section and the *sdpf* model space of Chapter 3.

In the model space from Section 5.1, the IOI interaction can be applied directly to ^{42}Si, composed of eight neutrons on top of the ^{34}Si target. The monopole terms account for evolution to heavier and more unstable isotopes, but reduce the predictive power outside of the experimental data included in the fit. Figure 5.2 showed the inaccuracy of Skyrme SPE in this model space for ^{34}Si and emphasized the necessity of parameterizing the SPE. If the Skxtb interaction reproduces the evolution of SPE from ^{34}Si to ^{42}Si, the appropriate SPE for the ^{42}Si calculation are modified from the Skyrme SPE by

$$\epsilon_{mod}^{42Si} = \epsilon_{Skxtb}^{42Si} + \epsilon_{fit}^{34Si} - \epsilon_{Skxtb}^{34Si}. \tag{5.2}$$

Two calculations will be performed in this model space: one with the IOI interaction, and another where the SPE of the IOI interaction have been modified by Eq. 5.2.

In the *sdpf* model space, the closed-subshell ^{42}Si nucleus is the target and the HRP is applied to determine two-body matrix elements and Skyrme single particle energies. With the limited data around ^{42}Si, SPE cannot be determined from experimental levels that approximate single particle states or by a fit to data; Skyrme uncorrelated SPE are utilized as discussed in Section 4.4.

The level schemes for ^{42}Si are shown in Fig. 5.15 for the different methods. In addition to the three HRP calculations, level schemes for experiment [99] and an empirical *sdpf* interaction [48] are provided for comparison. Thus far, the experimental studies have only detected the ground state and the first excited 2^+ state. Theoretically, the first excited 0^+ varies by 1.8 MeV. With the interaction from the application of the HRP in the *sdpf* model space (iii), the 0_2^+ state is higher in energy than the 4_1^+ state. On the other hand, the 0_2^+ state is the first excited state with both the empirical SDPF-U interaction and the IOI interaction from Section 5.1. The energy of the 0_2^+ state in ^{42}Si can provide information regarding the mixing between shape coexisting states and the stability of the $N = 28$ shell closure, following the discussion in Section 5.1.6.

The IOI interaction (i) produces a high level density relative to the other theoretical approaches, including an interaction with the same TBME but modified SPE (ii). Accounting for the evolution of Skyrme single particle energies from ^{34}Si to ^{42}Si also results in a lower 2^+ energy, in better agreement with experiment. For the microscopic interaction in the *sdpf* model space (iii), a low density of states is observed. While excitations of the *sd* orbits cannot occur, such that the level density is expected to be lower than in (i) and (ii), the active orbits are identical to the SDPF-U calculation. The microscopic approach does not reproduce the low-lying 0_2^+ state of the empirical interaction. More experimental data is needed for definitive conclusions on the importance of excitations of the *sd* neutrons and on the possibility of improving single particle energies for exotic isotopes by modifying Skyrme SPE with Eq. 5.2. The identification of the 4_1^+ and 0_2^+ states, which will occur with rare isotope facilities, can provide valuable insight for the application of the HRP far from stability.

Chapter 6

Outlook and Conclusions

The Hybrid Renormalization Procedure has been applied to regions of recent experimental interest. The agreement with available experimental data suggests the viability of the method, such that it can be extended to other regions of the nuclear chart. However, the deviation from experiment indicates that there are still improvements necessary. As discussed in Chapter 4, one improvement relates to the inconsistency and inaccuracy of Skyrme single particle energies. Microscopic energy density functionals, which are in the early stages of development, should focus on accurately accounting for the single particle properties of nuclei. The need for SPE parameters, as implemented in Section 5.1, could be eliminated with better functionals. Progress on any research method utilized by the HRP, i.e. renormalization group methods, many-body perturbative techniques, Configuration Interaction theory, and Energy Density Functional methods, will reduce the uncertainties in derived effective interactions and produce more reliable results.

Advancements in nuclear structure research external to this work can be continually implemented to enhance the HRP. Concurrently, the HRP can be improved by accounting for the effect of many-body forces. As discussed in Section 2.2, the HRP attempts to approximately include three-body effects in two ways: through the Skyrme interaction and through the introduction of monopole parameters as in Section 5.1. The effective two-body component of the three-body force is not included accurately in either case, but could be implemented in the HRP directly through a modification of the two-body matrix elements. The importance of this effective two-body component can be estimated from Fig. 2.3 since the USDB interaction implicitly includes the contribution from three-body forces while the HRP-SD interaction does not. Therefore, a treatment of three-body forces at the effective two-body level could significantly improve the effective interaction.

6.1 Three-body Forces

Truncating at three-body forces, the Hamiltonian was represented diagrammatically in Fig. 1.3. Single particle energies derived from EDF methods, for instance the one-nucleon separation energies calculated in Skyrme Hartree-Fock theory, include contributions from all terms within the dashed black box. Two-body matrix elements in the Hybrid Renormalization Procedure currently include only the explicit two-body component as derived from a microscopic nucleon-nucleon interaction. However, the effective two-body component of the three-body diagram, as determined from Skyrme Hartree-Fock theory [13], can be added through the monopole terms of the effective interaction given by

$$\bar{V}_{ab} = \frac{\sum_J (2J+1)\langle ab \mid V \mid ab\rangle_{JT}}{\sum_J (2J+1)}. \tag{6.1}$$

The monopole terms of the effective interaction, as derived from a microscopic nucleon-nucleon interaction with the HRP, are denoted $\bar{V}_{ab}^{NN}$. To account for the three-body forces at the effective two-body level, the monopole can instead be taken from calculations with EDF methods for two particles coupled to the target nucleus. For a target nuclues T, the monopole is

$$\bar{V}_{ab}^{EDF} = E(T+a+b) - E(T) - \epsilon_a - \epsilon_b, \tag{6.2}$$

where ϵ_i are one-nucleon addition energies of particle orbits outside the core, obtained with the equal filling approximation in an SR-EDF calculation as discussed in Section 4.4, and $E(T{+}a{+}b)$ is the energy of the configuration for a closed-shell target plus two nucleons constrained to be in orbitals a and b in a single reference EDF calculation restricted to spherical symmetry. The difference between $\bar{V}_{ab}^{EDF}$ and $\bar{V}_{ab}^{NN}$ represents the effective two-body component of the three-body force. All valence TBME can be modified by

$$\langle ab \mid V \mid ab\rangle_{JT}^{eff} = \langle ab \mid V \mid ab\rangle_{JT}^{HRP} - \bar{V}_{ab}^{NN} + \bar{V}_{ab}^{EDF} \tag{6.3}$$

to include the three-body force via the monopole two-body interaction.

Brown et al. [13] have applied this procedure to a ^{208}Pb target to produce level schemes in good agreement with experiment. An important effect of the procedure, shown in Fig. 7 of [13], is the reproduction of experimental binding energies as many particles are added. In order for a direct comparison between single-reference calculations with CI and EDF methods, the single particle energies in the effective interaction must be taken from the one-nucleon separation energies as determined by the energy density functional that is used to calculate $\bar{V}_{ab}^{EDF}$, rather than from experimental states or from a fit to data. The difference between the two calculations with a single Slater determinant can then be represented as the monopole of the explicit three-body term in Fig. 1.3, with matrix elements on the order of 1-2 keV [13]. The diagonalization of the full model space Hamiltonian results in correlations due to configuration mixing, which increases the binding energy for nuclei away from the closed shell.

The inclusion of three-body forces through a monopole two-body interaction has been shown to have a 5.3 MeV effect for ten protons outside of ^{208}Pb [13]. In Section 5.1, the monopole parameters contributed 11.1 MeV for ^{34}Si, which is composed of twelve nucleons outside the core. For a three-body interaction with identical strength in both regions, a contribution of 9.7 MeV is expected for ^{34}Si due to the additional permutations allowed for twelve particles. The monopole parameters provide approximately the expected strength due to three-body forces, but are not understood on a fundamental level. The parameters could be eliminated with an appropriate treatment of the effective two-body component of the three-body force, through an implementation of Eq. 6.3 in the Hybrid Renormalization Procedure. The application to the island of inversion region could be revisited, or calculations in other regions of interest could be performed.

6.2 Other Regions of Interest

Ab initio approaches are applicable for $A < 16$ and provide a nearly exact solution starting from microscopic potentials. Standard Configuration Interaction methods treat ^{16}O as a vacuum and produce results throughout the *sd* shell. For instance, the USDB interaction can be used throughout the *sd* shell with an rms deviation around 130 keV. As seen in Section 2.2, the Hybrid Renormalization Procedure can be applied to nuclei in the *sd* shell to provide results in reasonable agreement with experiment. However, due to the lack of three body forces, the results will not surpass those of empirical interactions like USDB. The form of the HRP-SD and USDB interactions is identical, as they both consist of single particle energies and two-body matrix elements in the model space. The USDB interaction supplies the best fit two-body Hamiltonian, thereby incorporating effects from many-body forces and orbits outside of the model space. A microscopic treatment of the many-body problem, as presented with the HRP, cannot improve upon the description of nuclei with the USDB interaction in the *sd* model space, but can provide insight into the contributions of three-body forces, for example.

The lightest nuclei that are particularly of interest for the HRP, since they cannot be calculated easily with other methods, lie on the neutron-rich side of the chart of nuclides. For instance, as mentioned in Chapter 3, the neutron-rich carbon isotopes require a reduction of 25% in the neutron-neutron interaction relative to the more stable oxygen isotopes. As in Chapter 3, the HRP might identify a microscopic origin of this reduction due to loosely bound valence orbits with long tails in their realistic radial wavefunctions.

By mass, the next neutron-rich isotopes outside of standard model spaces occur around $N = 20$. The HRP was applied in Chapter 5 to explain the island of inversion region, but the produced interaction was applied to one hundred nuclei, including the light neutron-rich isotopes around $N = 20$. In Section 5.2, the behavior of the $N = 28$ subshell was also probed through an investigation of ^{42}Si. Future applications of the HRP are to other "islands of shell-breaking" where, like the island of inversion, higher-energy orbits are filled preferentially to the standard ordering of orbits from Fig. 1.2. The next region of the chart of nuclides with similar behavior to the island of inversion occurs near the neutron-rich nickel isotopes. A fully occupied pf shell for ^{68}Ni results in magicity which is broken for ^{66}Fe when two protons are removed. Positive parity orbits, namely the $g_{9/2}$ neutron orbit, are occupied in the ground state at $N = 40$. This region could be studied with the HRP, treating ^{68}Ni as the target in the same manner that ^{34}Si was the target for the island of inversion region: as an exotic nucleus with good closed-subshell properties outside of the island of shell-breaking. The computing power required for the ^{68}Ni region is significantly larger than the island of inversion region, but calculations are tractable with modern parallelized resources.

Proton-rich nuclei outside of standard model spaces are another possibility for an application of the HRP. Unfortunately, less experimental data is known on this side of stability, but nuclei that occupy sd neutron orbits and pf proton orbits could be compared to their mirror nuclei in the $sdpf$ model space defined in Section 1.7. In this case, ^{34}Ca would be the target and results could be compared to the known isotopes from $Z = 20$ to $Z = 24$ with $N \leq 19$.

Finally, a study of heavy nuclei near the doubly magic ^{100}Sn, ^{132}Sn, and ^{208}Pb cores would provide a more microscopic prediction of collectivity in the tin and lead isotopic chains, of recent experimental [100] and theoretical [101] interest. The onset and reduction in collectivity as a function of neutron number offers insight into the shell structure and the strength of pairing matrix elements. A realistic calculation like the HRP that accounts for these effects directly would better explain the experimental results, especially with the inclusion of three-body effects from Section 6.1.

6.3 Single Particle Energies

As discussed in Section 4.4, the uncorrelated SPE of Skyrme interactions have been implemented in the Hybrid Renormalization Procedure to produce the SPE component of effective interactions. However, the one-nucleon separation energies of Skyrme interactions, which require the solution of Skyrme Hartree-Fock equations for three different nuclei, provide better indications of experimental behavior and should have been implemented in effective interactions derived from the HRP. The calculations in Chapter 3 and Sections 2.2 and 5.2 should be examined with the single particle energies of the effective interactions derived from the one-nucleon separation energies of the Skxtb interaction. Unless the uncertainty due to the equal filling approximation is quantified and is small relative to the global uncertainty of separation energies with the Skyrme interaction, a Skyrme Hartree-Fock solution for odd nuclei which breaks time-reversal symmetry is necessary. With either uncorrelated SPE or one-nucleon separation energies from EDF methods, the dependence of results on the parameterization of the Skyrme interaction should also be examined; in particular, the role of the tensor force, determined by a comparison of Skx and Skxtb for instance, should be understood from stability to exotic nuclei.

The centroid energy as defined in Eq. 4.3 is a simplification of the centroid energy described by Baranger [65], since the off-diagonal centroid matrix elements are neglected. The effective single particle energies obtained from a diagonalization of the centroid matrix can be compared to the results presented in Chapters 4 and 5 to evaluate the dependence on the simplified treatment of the centroid energy. A systematic study of ESPE and one-nucleon separation energies with various nuclear structure techniques would provide guidance regarding the uncertainties in single particle energies and the derivation of energy density functionals.

In a large model space, the SPE of the effective interaction should be determined from the ESPE of the target nucleus. For nuclei within the model space that are many particle or hole excitations from the target, the ESPE can be significantly different than the SPE of the effective interaction. In other words, the single particle structure can evolve as a function of proton or neutron number. In Section 5.2, the evolution of uncorrelated Skyrme SPE from ^{34}Si to ^{42}Si was assumed to reproduce the necessary change in the experimental ESPE from ^{34}Si to ^{42}Si, resulting in a modified interaction denoted (ii) in Fig. 5.15. The resultant calculations for ^{42}Si are affected greatly by the evolution of SPE, as seen in the comparison of (i) and (ii) in Fig. 5.15. The lack of experimental data and the lack of further applications of SPE modified by Eq. 5.2 prevent a definitive conclusion regarding the best way to calculate nuclei far from the target nucleus in a large model space.

6.4 Conclusion

The extension of experimental capabilities to more exotic nuclei with new or planned rare isotope facilities has emphasized the necessity of reliable theoretical calculations for nuclei outside of standard model spaces. Hybrid methods, which combine properties of the Configuration Interaction method and Energy Density Functional methods, can incorporate the generality of EDF methods with the accuracy of the CI method.

A hybrid method has been developed to convert a microscopic nucleon-nucleon potential into a low-momentum interaction via renormalization group methods, namely the v_{lowk} procedure. Many-body perturbative techniques can then renormalize the low-momentum interaction into a reduced model space using Rayleigh-Schrödinger perturbation theory. An effective interaction, composed of single particle energies obtained from Skyrme Hartree-Fock theory and two-body matrix elements from the renormalization procedure, can be implemented into full-scale Configuration Interaction calculations to determine theoretical properties of interest. A proof of principle was confirmed for this Hybrid Renormalization Procedure in a standard model space; the HRP results in the *sd* shell with ^{16}O as the target nucleus agree with the empirical USDB Hamiltonian to the expected accuracy, accounting for the restriction to a microscopic two-body force.

One ingredient of the HRP is the basis, with three choices studied: the harmonic oscillator basis, standard for many applications in nuclear physics; a realistic basis derived from Energy Density Functional methods; and a mixed basis, using harmonic oscillator radial wavefunctions and Energy Density Functional single particle energies. Due to recent experimental and theoretical interest in the *sdpf* shell and the neutron-rich silicon isotopes, six interactions were derived in the *sdpf* shell using all combinations of the three bases and two target nuclei, the doubly magic ^{40}Ca nucleus and the exotic ^{34}Si nucleus. In the harmonic oscillator and mixed bases, the interaction is nearly identical regardless of the choice of target. However, the ^{34}Si target reduces the strength of the interaction in the realistic basis as a result of the extended wavefunctions for loosely bound model space orbits. Calculations for neutron-rich silicon isotopes display the importance of the accurate determination of effective interactions away from stability. Accounting for the evolution of shell structure through a realistic basis is essential for an accurate description of exotic nuclei, but three-body forces must also be included for accuracy at the level of 100 keV.

Single particle energies are an important component of the Hybrid Renormalization Procedure, but are not determined accurately in Skyrme Hartree-Fock theory, particularly for light nuclei. Centroid energies from Eq. 4.3, whether determined from experiment or theory, are desired for the target nucleus since they better represent the single particle properties of interest throughout a given model space. As centroid energies cannot be easily obtained, the SPE in the effective interaction can be parameterized to improve upon the Skyrme Hartree-Fock description.

The Hybrid Renormalization Procedure was performed to generate an effective interaction for calculations in the island of inversion region. With twelve parameters to improve upon the Skyrme Hartree-Fock treatment of single particle energies and three-body forces, and an overall normalization of the two-body matrix elements, the level schemes of one hundred nuclei were calculated. Binding energies and low-energy states are in good agreement with available data when the 370 keV rms deviation of the interaction is taken into consideration. The boundaries of the island of inversion are determined theoretically through the evaluation of the ground state wavefunctions, and suggest that the island of inversion is larger than observed thus far, extending to both more neutron-rich nuclei and nuclei with fewer protons. Beta decay transitions from ^{35}Si and ^{33}Mg, and one- and two-neutron transfer on ^{26}Ne and ^{30}Mg, respectively, have also been studied and compared to recent experimental data. The level schemes of ^{42}Si with different applications of the HRP have been compared to experiment and to the result with an empirical interaction. The measurement of the 0_2^+ and 4_1^+ energies, which vary significantly in the theoretical approaches, will enable the evaluation of different techniques to calculate exotic isotopes via the HRP.

The Hybrid Renormalization Procedure can be improved by implementing three-body forces at the effective two-body level. Other aspects of the Hybrid Renormalization Procedure, particularly the single particle energies derived from Energy Density Functional methods but also renormalization group methods and many-body perturbative techniques, are of interest for future study. Progress in these areas can be implemented directly into the Hybrid Renormalization Procedure along with three-body forces to provide better convergence properties and effective interactions.

The extensive results obtained in the island of inversion region pertain to one application of the Hybrid Renormalization Procedure. Theoretical predictions for other nuclei outside of standard model spaces can be produced in future applications.

Appendix

Appendix A

Abbreviations and Definitions of Selected Terms

α - representation of the quantum numbers of a single orbit

A - mass number

Argonne v_{18} - a microscopic NN potential composed of eighteen local operators

BE - binding energy of a system

BR - branching ratio

C_{ij} - coefficients for the two-body monopole parameters in the IOI interaction

C_3 - coefficient for the three-body monopole parameter in the IOI interaction

C^2S - spectroscopic factor, where C is the isospin Clebsch-Gordan coefficient and S is defined in Eq. 4.1

CI - Configuration Interaction; CI theory is an approximate method to calculate the Schrödinger Equation 1.1 that operates in a reduced model space

CIB - charge-independence breaking; denotes a strong force where the average of the proton-proton and neutron-neutron interactions is not identical to the proton-neutron interaction

CSB - charge-symmetry-breaking; denotes a strong force where the proton-proton interaction is not identical to the neutron-neutron interaction

D - dimension of the model space

DFT - Density Functional Theory; DFT attempts to write the energy of a nucleus as a functional of the local density of the system, and to solve for the energy of a system through the minimization of that functional

E - energy of a system

EDF - Energy Density Functional; the energy written as a functional of the density of a system. EDF methods are similar to DFT, except that the Hohenberg-Kohn theorems are not satisfied by the nuclear functionals which break symmetries present in the nuclear system

ENSDF - Evaluated Nuclear Structure Data File, an online database containing nuclear properties such as excitation energies and log ft values

ESPE - effective single particle energy or centroid, as defined by Eq. 4.3 and denoted by ϵ

Exp. - experiment

ft - a phase space factor f multiplied by the half-life t for nuclear β decays; often given as log ft, where the logarithm has base 10.

g_A, g_V - coupling constants for the axial-vector, vector component of the weak interaction

G-matrix - an RG method that solves or approximates Eq. 1.19

H - Hamiltonian

H_0 - the mean field component of the nuclear Hamiltonian

H_1 - the remainder of the nuclear Hamiltonian, which can be treated as a perturbation from H_0

HO - harmonic oscillator

HRP - Hybrid Renormalization Procedure; defined in Chapter 2

HRP-SD - an interaction in the *sd* model space calculated for a ^{16}O target in the standard implementation of the HRP

HRP-3rd - identical to HRP-SD, except that diagrams are calculated to third order in Rayleigh-Schrödinger perturbation theory

IOI - an effective interaction derived from the HRP to calculate nuclei in and near the island of inversion region; see Section 5.1 for details

$\hbar\omega$ - energy scale in nuclear physics based on the solution of a harmonic oscillator mean field, where empirically $\hbar\omega = (45A^{-1/3} - 25A^{-2/3})$ MeV; an $\hbar\omega$ excitation refers to an increase in the main quantum number N by one

j - total angular momentum of a single particle

J - total angular momentum of a system

J^{π} - total angular momentum and parity of a system

k - representation of the quantum numbers of a many-body system

Λ - the cutoff in momentum space for the v_{lowk} renormalization procedure

ℓ - orbital angular momentum

m_j - projection of j along the z-axis

MIX - a basis which is composed of HO radial wavefunctions and SHF single particle energies

MSk7 - parameterization of the Skyrme interaction without a tensor force

n - radial quantum number

npnh - number of particle and hole excitations from a reference state, typically a Slater determinant with the natural ordering of orbits

N - can refer either to neutron number or main quantum number for a harmonic oscillator potential, where $N = 2n + \ell$; the disctinction should be clear from the usage in the text

NN - nucleon-nucleon; microscopic NN interactions or potentials describe the interaction between two free nucleons (proton or neutron) and are fit to scattering data

NNN - nucleon-nucleon-nucleon; microscopic NNN interactions or potentials describe the interaction between three free nucleons and are dependent on the choice of NN interaction

N2LO,N3LO - next-to-next-to-leading order, next-to-next-to-next-to-leading order;

the order of perturbation theory in χEFT; the N3LO interaction is a chiral microscopic NN potential at the N3LO level fit to elastic scattering data

ρ - the local density of a system

p - model space composed of all $N = 1$ single particle orbits $(0p_{3/2}, 0p_{1/2})$

pf - model space composed of all $N = 3$ single particle orbits $(0f_{7/2}, 0f_{5/2}, 1p_{3/2}, 1p_{1/2})$

P, Q - projection operators into (P) and out of (Q) the model space

Q-value - mass or binding energy differences between the reactants and products of a reaction

$\hat{Q}(\omega)$ or Q-box - the sum of all irreducible and valence-linked diagrams with at least one H_1 vertex; see [11] for a complete description

QCD - quantum chromodynamics

RG - Renormalization Group; RG methods are used to convert a microscopic NN potential with a hard core into a softer potential where the high- and low-momentum modes are decoupled

σ - standard deviation

s - model space composed of all $N = 0$ single particle orbits $(0s_{1/2})$

sd - model space composed of all $N = 2$ single particle orbits $(0d_{5/2}, 0d_{3/2}, 1s_{1/2})$

$sdpf$ - the model space composed of the sd proton orbits and pf neutron orbits

S_n - one-neutron separation energy

S_{2n} - two-neutron separation energy

SDPF-NR,SDPF-U - empirical interactions in the $sdpf$ model space

SHF - Skyrme Hartree-Fock

Skx, Skxtb - parameterizations of the Skyrme interaction without, with a tensor force

Sly4 - parameterization of the Skyrme interaction with a tensor force

SPE - single particle energy

SR-EDF - Single Reference EDF; EDF methods where a single Slater determinant is used as an auxiliary wavefunction for the minimization of the energy density functional

T - in general, T refers to the isospin of a system; in Section 1.4, it refers to the scattering matrix while in Section 6.1 it refers to a target nucleus

TBME - two-body matrix elements

μ - the nuclear magnetic moment, often reported in terms of the nuclear magneton μ_N

UNEDF - Universal Nuclear Energy Density Functional; a collaboration funded by the U.S. Department of Energy to determin a microscopic EDF for nuclear physics

USD,USDA,USDB - empirical two-body interactions in the *sd* model space

v_{lowk} - an RG method that approximates Eq. 1.20

ω - when separate from $\hbar$, the starting energy of a two-body diagram in Rayleigh-Schrödinger perturbation theo

WBP,WBP-M - empirical interactions in a model space composed of all orbits through the main quantum number $N = 3$

χEFT - chiral effective field theory

Z - proton number

Bibliography

BIBLIOGRAPHY

[1] P. Ring and P. Schuck, *The Nuclear Many-Body Problem.* Springer-Verlag Berlin Heidelberg, 1980.

[2] E. Caurier et al., Rev. Mod. Phys. 77, 427 (2005).

[3] J. Suhonen, *From Nucleons to Nucleus.* Springer-Verlag Berlin Heidelberg, 2007.

[4] V. Zelevinsky, *Quantum Physics.* Wiley, 2011.

[5] J. Blomqvist and A. Molinari, Nucl. Phys. A **106**, 545 (1968).

[6] B. A. Brown, A. Etchegoyen, W. D. M. Rae, N. S. Godwin, W. A. Richter, C. H. Zimmerman, W. E. Ormand and J. S. Winfield, MSU-NSCL Report No. 524, 1985.

[7] E. Caurier and F. Nowacki, Acta Phys. Pol. B **30**, 705 (1999).

[8] NuShell, W.D.M. Rae, http://knollhouse.org/default.aspx

[9] NuShellX@MSU, B.A. Brown and W.D.M. Rae, http://www.nscl.msu.edu/~brown/resources/resources.html

[10] K.A. Brueckner, Phys. Rev. **96**, 508 (1954).

[11] M. Hjorth-Jensen, T.T.S. Kuo, and E. Osnes, Phys. Rept. **261**, 125 (1995).

[12] B.A. Brown, Lecture Notes in Nuclear Structure Physics, unpublished.

[13] B.A. Brown, A. Signoracci, and M. Hjorth-Jensen, Phys. Lett. B **695**, 507 (2011).

[14] S.C. Pieper, V.R. Pandharipande, R.B. Wiringa, and J. Carlson, Phys. Rev. C **64**, 014001 (2001).

[15] B.A. Brown and W.A. Richter, Phys. Rev. C **74**, 034315 (2006).

[16] S. Cohen and D. Kurath, Nucl. Phys. **73**, 1 (1965).

[17] M. Honma, T. Otsuka, B.A. Brown, and T. Mizusaki, Phys. Rev. C **65**, 061301(R) (2002).

[18] P. Quentin and H. Flocard, Ann. Rev. Nucl. Part. Sci. **28**, 523 (1978).

[19] W. Kohn and L.J. Sham, Phys. Rev. **140**, A1133 (1965).

[20] W. Koch and M.C. Holthausen, *A Chemist's Guide to Density Functional Theory.* Wiley, 2000.

[21] B. Gebremariam, T. Duguet, and S.K. Bogner, Phys. Rev. C **82**, 014305 (2010).

[22] B.G. Carlsson, J. Dobaczewski, and M. Kortelainen, Phys. Rev. C **78**, 044326 (2008).

[23] M. Kortelainen et al., Phys. Rev. C **82**, 024313 (2010).

[24] Universal Nuclear Energy Density Functional (UNEDF) SciDAC Collaboration, http://www.unedf.org

[25] J. Decharge and D. Gogny, Phys. Rev. C **21**, 1568 (1980).

[26] T.H.R. Skyrme, Nucl. Phys. **9**, 615 (1959).

[27] D. Vautherin and D.M. Brink, Phys. Rev. C **5**, 626 (1972).

[28] M. Stoitsov et al., Phys. Rev. C **82**, 054307 (2010).

[29] B.A. Brown, Phys. Rev. C **58**, 220 (1998).

[30] B.A. Brown et al., Phys. Rev. C **74**, 061303(R) (2006).

[31] S.K. Bogner, R.J. Furnstahl, and A. Schwenk, Prog. Part. Nucl. Phys. **65**, 94 (2010).

[32] D.R. Entem and R. Machleidt, Phys. Rev. C **68**, 041001(R) (2003).

[33] R.B. Wiringa, V.G.J. Stoks, and R. Schiavilla, Phys. Rev. C **51**, 38 (1995).

[34] K. Tsukiyama, S.K. Bogner, and A. Schwenk, arXiv:1006.3639

[35] D.J. Gross and F. Wilczek, Phys. Rev. D **8**, 3633 (1973).

[36] K.A. Brueckner, Phys. Rev. **97**, 1353 (1955).

[37] S.K. Bogner, T.T.S. Kuo, and S. Schwenk, Phys. Rept. **386**, 1 (2003).

[38] J. Paldus, *Diagrammatic Methods for Many-Electron Systems.* In: Lecture Notes, University of Nijmegen Press, Njimegen (1991).

[39] S. Goriely, N. Chamel, and J.M. Pearson, Phys. Rev. Lett. **102**, 152503 (2009).

[40] E. Bender, K.W. Schmid, and A. Faessler, Nucl. Phys. A **596**, 1 (1996).

[41] R. Rodriguez-Guzman, Y. Alhassid, and G.F. Bertsch, Phys. Rev. C **77**, 064308 (2008).

[42] C. Thibault et al., Phys. Rev. C **12**, 644 (1975).

[43] T. Otsuka et al., Phys. Rev. Lett. **87**, 082502 (2001).

[44] S.M. Lenzi, F. Nowacki, A. Poves, and K. Sieja, Phys. Rev. C **82**, 054301 (2010).

[45] D.M. Manley et al., Phys. Rev. C **41**, 448 (1990).

[46] J. Retamosa, E. Caurier, F. Nowacki, and A. Poves, Phys. Rev. C **55**, 1266 (1996).

[47] S. Nummela et al., Phys. Rev. C **63**, 044316 (2001).

[48] F. Nowacki and A. Poves, Phys. Rev. C **79**, 014310 (2009).

[49] Home Page of Morten Hjorth-Jensen, http://folk.uio.no/mhjensen/cp/mhj.html

[50] A. Signoracci, B.A. Brown, and M. Hjorth-Jensen, Phys. Rev. C **83**, 024315 (2011).

[51] A. Signoracci and B.A. Brown, Phys. Rev. C **75**, 024303 (2007).

[52] A. Signoracci and B.A. Brown, Phys. Rev. Lett. **99**, 099201 (2007).

[53] Evaluated Nuclear Structure Data File (ENSDF) database, http://www.nndc.bnl.gov/ensdf/index.jsp

[54] G. Hagen et al., Phys. Rev. C **76**, 034302 (2007).

[55] T. Otsuka et al., Phys. Rev. Lett. **95**, 232502 (2005).

[56] E. Chabanat et al., Phys. Scr. **1995**, 231 (1995).

[57] M. Hjorth-Jensen, E. Osnes, H. Müther, and K.W. Schmid, Phys. Lett. B **248**, 243 (1990).

[58] J. Shurpin, H. Müther, T.T.S. Kuo, and A. Faessler, Nucl. Phys. A **293**, 61 (1977).

[59] H.M. Sommermann et al., Phys. Rev. C **23**, 1765 (1980).

[60] M. Stanoiu et al., Phys. Rev. C **78**, 034315 (2008).

[61] T.T.S. Kuo, F. Krmpotic, and Y. Tzeng, Phys. Rev. Lett. **78**, 2708 (1997).

[62] K. Ogawa et al., Phys. Lett. B **464**, 157 (1999).

[63] L. Gaudefroy, W. Mittig, et al., private communication.

[64] J. Lee, M.B. Tsang, and W.G. Lynch, Phys. Rev. C **75**, 064320 (2007).

[65] M. Baranger, Nucl. Phys. A **149**, 225 (1970).

[66] S. Michimasa et al., Phys. Lett. B **638**, 146 (2006).

[67] J. Lee et al., Phys. Rev. C **73**, 044608 (2006).

[68] W. H. Dickhoff and C. Barbieri, Prog. Part. Nucl. Phys. **52**, 377 (2004).

[69] A. Terakawa et al., Phys. Rev. C **66**, 064313 (2002).

[70] L. Gaudefroy et al., Phys. Rev. Lett. **97**, 092501 (2006).

[71] S. Goriely, F. Tondeur, and J.M. Pearson, At. Data and Nucl. Data Tabl. **77**, 311 (2001).

[72] M. Beiner, H. Flocard, N. Van Giai, and P. Quentin, Nucl. Phys. A **238**, 29 (1975).

[73] F. Ajzenberg-Selove, Nucl. Phys. A **281**, 1 (1977).

[74] T. Duguet et al., *Effective single-particle energies in correlated many-nucleon systems.*

[75] T. Otsuka et al., Phys. Rev. Lett. **105**, 032501 (2010).

[76] J.K. Tuli, "Evaluated Nuclear Structure Data File," Brookhaven National Laboratory report number 60875 (1995), http://www.osti.gov/bridge/servlets/purl/61189-DEdkFc/webviewable/61189.pdf

[77] M. Gélin, Doctorat de l'université de Caen GANIL T 07 02, page 100; O. Sorlin, private communication.

[78] P. Fallon et al., Phys. Rev. C **81**, 041302(R) (2010).

[79] A.N. Deacon et al., Phys. Rev. C **82**, 034305 (2010).

[80] D. Miller et al., Phys. Rev. C **79**, 054306 (2009).

[81] Georges Audi and Wang Meng, private communication, April 2011.

[82] G. Audi, A. H. Wapstra and C. Thibault, Nucl. Phys. A **729**, 337 (2003).

[83] M. Fauerbach et al., Phys. Rev. C **53**, 647 (1996).

[84] A. Schiller et al., Phys. Rev. C **72**, 037601 (2005).

[85] H. Sakurai et al., Phys. Lett. B **448**, 180 (1999).

[86] S.M. Brown et al., *Neutron shell breaking in the neutron-rich ^{27}Ne nucleus.*

[87] P. Doornenbal et al., Phys. Rev. C **81**, 041305(R) (2010).

[88] http://www.nscl.msu.edu/~brown/resources/island/jpg/island.htm

[89] V. Tripathi et al., Phys. Rev. Lett. **101**, 142504 (2008).

[90] D.H. Wilkinson, Nucl. Phys. A **377**, 474 (1982).

[91] E.K. Warburton et al., Phys. Rev. C **34**, 1031 (1986).

[92] B.A. Brown and B.H. Wildenthal, At. Data and Nucl. Data Tabl. **33**, 347 (1985).

[93] D.T. Yordanov et al., Phys. Rev. Lett. **99**, 212501 (2007).

[94] Ø. Jensen et al., arXiv:1104.1552

[95] E.K. Warburton and B.A. Brown, Phys. Rev. C **46**, 923 (1992).

[96] I.J. Thompson, Comput. Phys. Rep. **7**, 167 (1998); http://www.fresco.org.uk

[97] C.M. Perey and F.G. Perey, At. Data and Nucl. Data Tabl. **17**, 1 (1976).

[98] K. Wimmer et al., Phys. Rev. Lett. **105**, 252501 (2010).

[99] B. Bastin et al., Phys. Rev. Lett. **99**, 022503 (2007).

[100] A. Jungclaus et al., Phys. Lett. B **695**, 110 (2011).

[101] A. Ansari, Phys. Lett. B **623**, 37 (2005).